

HIGH RESOLUTION AUGER SPECTROSCOPY IN ENERGETIC ION ATOM COLLISIONS

N. STOLTERFOHT

*Hahn-Meitner-Institut für Kernforschung Berlin GmbH, Bereich Kern- und Strahlenphysik,
D-1000 Berlin 39, Fed. Rep. of Germany*



NORTH-HOLLAND – AMSTERDAM

HIGH RESOLUTION AUGER SPECTROSCOPY IN ENERGETIC ION ATOM COLLISIONS

N. STOLTERFOHT

Hahn-Meiner-Institut für Kernforschung Berlin GmbH, Bereich Kern- und Strahlenphysik, D-1000 Berlin 39, Fed. Rep. of Germany

Received June 1986

Contents:

1. Introduction	317	4.3. L- and M-Auger transitions	366
1.1. Historical background	318	4.4. Statistical analysis of the Auger spectra	370
1.2. Notations and definitions	319	4.5. Analysis of individual lines	375
2. Theory of nonradiative transitions	324	5. Projectile Auger spectroscopy	384
2.1. Basic formalism	324	5.1. General considerations	384
2.2. Transition energies	335	5.2. Kinematic effects	386
2.3. Transition rates	341	5.3. K-Auger transitions	389
3. Collision kinematics	347	5.4. L-Auger transitions	405
3.1. Kinematics of projectile and target atom	347	5.5. Transitions involving Rydberg electrons	412
3.2. Kinematic effects on the ejected electrons	350	Appendix A1. Summary of atomic units	417
4. Target Auger spectroscopy	356	Appendix A2. Expansion coefficients	418
4.1. General considerations	356	References	418
4.2. K-Auger transitions	358		

Single orders for this issue

PHYSICS REPORTS (Review Section of Physics Letters) 146, No. 6 (1987) 315-424.

Copies of this issue may be obtained at the price given below. All orders should be sent directly to the Publisher. Orders must be accompanied by check.

Single issue price Dfl. 78.00, postage included.

1. Introduction

In 1925 Pierre Auger [1, 2] observed remarkable tracks in cloud chamber graphs and attributed them to monoenergetic electrons spontaneously emitted from atomic species. This observation was the discovery of an important decay mode of highly excited atoms competing with the well-known decay mode of photon emission. The picture of Auger was theoretically confirmed by Wentzel [3] who formulated the process of spontaneous electron emission in 1927. In the following decades the Auger effect received increasing attention in many fields of physics including atomic, nuclear, solid state, and surface physics.

The transition resulting in Auger electron emission is caused by the electron–electron interaction. Generally, the Auger process involves two active electrons interacting with each other in the field of the atomic nucleus screened by the other (passive) electrons. The initial state is discrete and its energy lies above the first ionization threshold. The final state implies the ejected electron and the residual ion. When the Auger transition takes place in the isolated atom, it is only dependent on atomic properties. Therefore, the study of the Auger effect yields direct information about the structure and the dynamics of the atom.

It should be realized that the Auger process is relatively slow in comparison with time units characteristic for the atom. For instance, the Auger process takes place during several hundreds of revolutions of orbiting outer-shell electrons. Thus, it follows from the uncertainty principle that the natural spread of the Auger electron energy is small in comparison with characteristic atomic energies. On the other hand, in comparison with radiative transitions in outer shells, the Auger process is very fast and, hence, the corresponding width of the Auger lines is comparably large.

Comprehensive articles have appeared reviewing previous work about the Auger effect. The theory of autoionization and the Auger effect has been discussed in detail by Burke [4], Burhop and Asaad [5], Chattarji [6], McGuire [7], and Åberg and Howat [8]. Surveys about experimental studies of ion-induced Auger electrons have been given by Ogurtsov [9], Niehaus [10], Rudd and Maceck [11], Sevier [12], Mehlhorn [13, 14] and Matthews [15]. Specific experimental studies of electron spectra have been discussed by Stolterfoht [16–18], Berényi [19] and Mann et al. [20]. Instrumental details are described in refs. [11–15, 18]. Related work concerning excitation mechanisms in ion–atom collisions have been reviewed, e.g. by Garcia et al. [21], Kessel and Fastrup [22], and Meyerhof and Taubjerg [23].

In the present article, high-resolution Auger spectroscopy is reviewed for energetic ion–atom collisions. Emphasis is given on the atom-structure aspect of multiply ionized atoms excited in the collision. The discussion is focussed on high-resolution spectra where individual lines are separated, in general. Studies at particle accelerators in the energy range of a few tenths of keV to a few hundreds of MeV are discussed.

The work in the field is rather extensive so that no attempt is made to give a complete summary here. Measurements below a few tenths of keV are not treated to maintain the emphasis on fast collisions. Also, limited information is presented about the production mechanisms of the autoionizing states. For instance, studies concerning the excitation of magnetic substates, i.e. angular distributions of the ejected electrons are not considered. Moreover, instrumental details are not discussed. For more information about the excitation mechanisms and the apparatus, the reader is referred to previous reviews.

Most previous reviews about the Auger effect have been devoted either to theoretical or experimental work. In the experimental reviews, the Auger electron work is often discussed among other aspects

of the more general method of electron spectroscopy. The present article summarizes both theoretical and experimental work. The theoretical part is primarily devoted to atomic structure theory. The discussion is kept on an introductory level appropriate for readers not familiar with the Auger effect. Furthermore, the formalism to calculate kinematic effects is presented. In the experimental part, the studies of Auger electrons for the target and projectile are treated in detail. It is felt that, since the field has rapidly expanded the target spectroscopy and projectile spectroscopy have developed separately. In this article, the attempt is made to treat both types of spectroscopies under the common aspects of their potentials and merits.

Atomic units summarized in appendix A1 are used throughout this article if not otherwise stated.

1.1. Historical background

The Auger effect was first investigated in conjunction with nuclear decay mechanisms producing inner-shell vacancies such as K-capture processes. Details about this early work may be obtained from Robinson and Cassie [24], Groyles et al. [25], and Nall et al. [26], for example. In the experiments radioactive sources were used in solid samples. To escape from the solid without much energy loss, the Auger electron must have a relatively high velocity. Thus, deeply lying inner shells of heavy elements were studied in this case.

Autoionization was first observed by Beutler [27] for gas targets using the method of photoionization. More recently, with the use of synchrotron radiation, the method of photoabsorption developed into an important tool to determine energies of autoionization states with high accuracy [28, 29]. A method similar to photoabsorption is the analysis of the energy loss of electrons scattered in forward direction [30]. Both types of experiments have extensively been used to investigate interferences between autoionization states and continuum states creating asymmetric autoionization line profiles [31]. This phenomenon which appears to be typical for autoionization was treated theoretically by Fano [32], and Fano and Cooper [33]. Fano profiles in the spectra of autoionization electrons have first been observed by Mehlhorn [34].

In the early 1960's the studies of the Auger effect and autoionization merged together in measurements of the ejected electrons from isolated atoms in gaseous or vapour targets, e.g. see refs. [35–38]. Excitation of the atoms were achieved by impact of photons, electrons, or ions. In the experiments, electrostatic spectrometers were generally used allowing the detection of electrons from a few eV to several keV. The high resolution abilities of the spectrometers made possible a detailed analysis of spectral structures.

When the collision time to excite the atom is small in comparison with the life time of the Auger or autoionization state, the decay process may be considered as being independent from the excitation process. This is generally true for incident photons or electrons. Therefore, these particles are well suited for studies of the decay mechanism in an isolated atom. Indeed, most experimental information about Auger states originate from measurements using photon and electron impact as described in reviews by Siegbahn et al. [39], Krause [40], and Carlson [41]. More recently, post-collision phenomena were studied in detail by means of photon and electron impact [42].

In addition to these particles, ions have been used to obtain spectroscopic information about Auger and autoionization states. Rudd [37] measured the first high resolution spectra of He autoionization electrons produced by H^+ and H_2^+ impact. The use of incident ions has advantages, since they may excite states which are not accessible by photon and electron impact. However, the use of ions has also disadvantages. Ion impact produces line broadening which may inhibit high-resolution studies. The

decaying target atom may be influenced by the slowly emerging charged projectile producing post-collision effect. They have first been observed by Barker and Berry [43] in early experiments of ion-induced autoionization electrons. Moreover, line broadenings are produced by kinematic effects [44]. In particular, heavy ions transfer large recoil momenta so that the emitter is moving in different directions during the decay [45]. For example, Ne K Auger spectra cannot be resolved when they are produced in Ne + Ne collisions at energies of a few hundred keV [46].

For the target atom, the broadening effects can substantially be reduced when the impact energy is increased. In 1973 Ne-Auger spectra were measured with high resolution by Matthews et al. [47] using oxygen projectiles of about 30 MeV. The spectra confirmed previous observations in the field of X-ray spectroscopy which have indicated considerable outer-shell ionization in addition to the inner-shell vacancy production [48]. In fact, with very heavy projectiles, the target atom can be stripped to a few electron system as shown by Stolterfoht et al. [49] for 200-MeV Xe³¹⁺ projectiles.

The possibility to remove several electrons in a single collision and to reduce the kinematic broadening effects opened the field of high-resolution Auger spectroscopy of few electron systems. Several groups performed studies of target Auger electron produced by energetic heavy-ion impact. Works from the different groups have been reported by Matthews et al. [47], Schneider et al. [50], Mann and Folkmann [51], Woods et al. [52], Kádár et al. [53], and Matsuo et al. [54].

The Auger electrons ejected from the projectile are influenced by an additional broadening effect. This effect originating from the finite acceptance angle of the spectrometer cannot be avoided by increasing the projectile velocity. Rather it gains importance when the incident velocity is increased. Hence, for projectile Auger electrons, serious problems arise with broadening effects, when incident particles are used at energies within the MeV range.

In the early 1970's, electrons from fast projectiles have been measured in a series of experiments performed by Sellin, Pegg and collaborators [55,56]. Care was taken to reduce the kinematic broadening effects so that the resolution was sufficient to resolve individual Auger lines. In particular, life times of metastable states were studied using beam foil techniques. Similar measurements have been made by Rødbro et al. [57] and Schneider et al. [58] using also gas targets. More recently, Newcomb et al. [59] studied projectile Auger electron ejection following charge transfer in gas targets.

Rødbro et al. [57] achieved rather high resolution by observing the electrons at forward angles of a few degrees. The broadening effect due to the finite analyzer acceptance angle decreases with decreasing observation angle and it vanishes in first order at zero degree. Hence, the broadening effect for the projectile may essentially be reduced when the electrons are observed at zero degree. First observations of autoionization electrons at zero degree have been made by Lucas and Harrison [60]. Recently, Itoh et al. [61] exploited the method of zero-degree Auger spectroscopy showing that Auger electrons from Ne and Ar projectiles may be measured with rather high resolution at energies as large as 100 MeV.

1.2. Notations and definitions

In a simple picture, the Auger effect may be regarded as electron transitions between atomic orbitals shown in fig. 1. The example refers to a vacancy in the shell X being filled by an electron from the shell Y. The excess energy is given to an electron in the shell Z so that it is transferred to a continuum state of well-defined energies.

The spontaneous transition causing the emission of an electron is also called *autoionization*. In principle, there is no difference between the Auger effect and autoionization. However, for historical

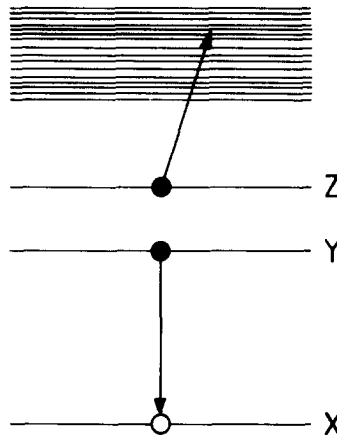


Fig. 1. Schematic diagram illustrating the Auger effect.

reasons it is common use to distinguish between different categories of initial states. The Auger effect refers to atoms ionized in an inner shell whereas autoionization is attributed to atoms doubly excited in the valence shell. However, it should be emphasized that this distinction loses significance, when inner and outer shells are simultaneously excited or ionized. Therefore, in this work no clear distinction is made between Auger effect and autoionization. When specific emphasis shall be given on inner or outer shell processes, the notations Auger process and autoionization will be retained. However, often the notation *Auger effect* is used to cover both effects. Also, the expression *nonradiative transition* is used in this case.

An individual Auger transition is defined by specifying fully the initial and final states involved. In multi-electron systems it is convenient to consider vacancies rather than electrons [62]. For example, an individual Auger transition is denoted by $K-L_1L_{23}(^1P)$, where the LS -coupling scheme is applied to fully specify the final state. Also, the transition $K-L_1LL_{23}(^3P)$ may be considered. Each transition gives rise to a line in the corresponding Auger spectrum as shown in fig. 2. The example refers to the K-Auger spectrum of Ne excited by 4.2-MeV H^+ impact [63].

All individual Auger transitions possible for given (sub)shells are summarized to (*sub*)groups using the notation $(K-L_1L_{23}) K-LL$ for example. Similarly, groups are summarized to *series* where only the shell of the initial state is specified, e.g. K-series or L-series. The present notation may also be applied to multi-vacancy states often created by heavy particle impact. Suppose that n L-vacancies are initially produced in addition to the K-vacancy, one may write KL^n-L^{n+2} . Of course, also subshells as well as terms may be specified.

An Auger line which refers to the transition from a single vacancy state to double vacancy states, is denoted as *normal line* or *diagram line*. Other lines are called *satellites*. For instance, the lines attributed to initial multi-vacancy states are satellites. Furthermore, lines due to double vacancies initially in the inner shell are called *hypersatellites*. The distinction between normal lines and satellite lines is very useful for incident electrons, photons and light ions, which produce primarily initial single vacancy states. However, for heavy ions which produce primarily multi-vacancy states, this distinction loses significance. Very often, heavy ions produce Auger spectra which consist exclusively of satellite lines.

Also, for multi-vacancy states, the convention to specify vacancies loses practicability. In particular for few-electron systems, it is preferable to specify electrons rather than vacancies. The same is true for

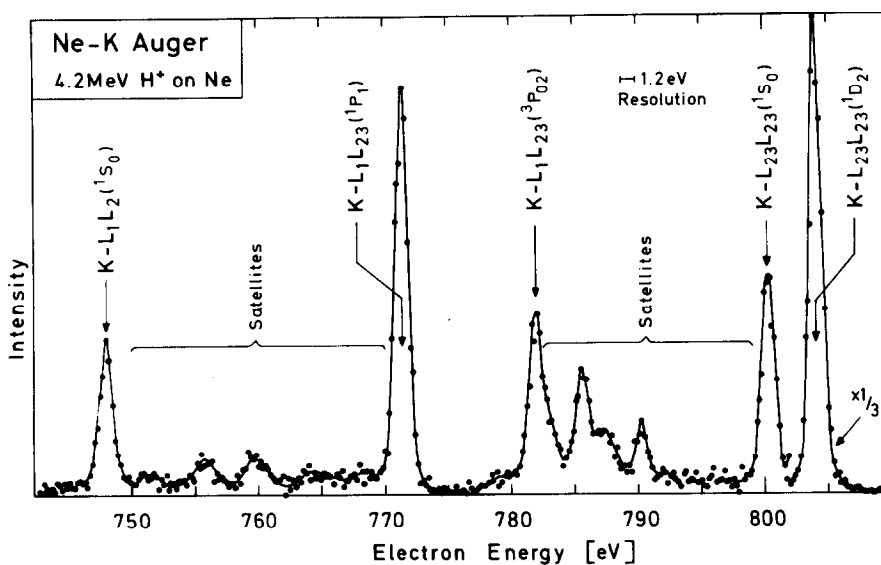


Fig. 2. Neon-K Auger spectrum produced by 4.2-MeV H^+ impact. From ref. [63].

autoionization involving outer-shell electrons. For example, an Auger transition in a 3-electron system is denoted by $1s^2-1s2p^2\ ^1D$ where again the LS -coupling scheme is applied. (Note that the order of specifying the initial and final state is reversed.) It should be pointed out that in the field of Auger spectroscopy in ion-atom collisions no preference is given to a specific notation scheme. Both schemes described above will be used further in this article.

The final state considered here refers to an atomic subsystem which has one electron less in comparison with the initial system. Thus, it is referred to as *final ionic state*. However, we may also consider the *final state* of the total system including the ejected electron. In this case, the notation $1s^2\epsilon d-1s2p^2\ ^2D$ is used for example. The existence of two different types of final states requires particular attention when properties of Auger transitions are specified. For instance, the selection rules for Auger transitions generally given in literature refer to the final state of the total system.

Further notations are commonly used to classify the Auger effect. A transition is called *Coster-Kronig* (CK) transition [64] when the initial vacancy and *one* final vacancy occupy subshells within one shell. A typical example for a CK transition is $L_1-L_{23}M$. If the initial vacancy and *both* final vacancies are produced in the same principal shell, the transition is called *Super-Coster-Kronig* (SCK) transition. The SCK transition is possible only for a limited number of atoms in the intermediate Z range. It is obvious that the energy of CK or SCK electrons is relatively small. However, the transition probabilities are rather large, i.e. up to a factor 10 larger than those of the competing Auger transitions.

In addition to the Auger effect described by Wentzel's Ansatz where two electrons are involved, *higher-order* Auger processes are possible where *three* or more electrons are affected. For example, Carlson and Krause [38, 65] observed the emission of two (continuous) electrons as a result of filling one K vacancy in Ne. This process has been denoted as *double Auger effect* [38]. Similarly, one electron may be excited simultaneously with the ejection of a (discrete) electron, when the inner-shell vacancy is filled. Processes of this type have been summarized by Krause et al. [66]. Furthermore, a double vacancy in an inner shell may be filled by a simultaneous transition of two electrons and the excess

energy is carried away by one electron to the continuum. This process had first been suggested by Ogurtsov [10] and subsequently observed by Afrosimov et al. [67].

The Auger process is characterized by the *transition energy* which is defined as the difference between the energies of the initial state and the final ionic state. The transition energy is equal to the energy of the ejected electron. Furthermore, the Auger process is characterized by the *transition rate* P_{if} which is equal to the number of Auger transitions per unit time. The transition rate corresponds by way of the uncertainty principle, to the *partial Auger width* Γ_{if}^a which has the dimension of an energy. Actually, the quantities P_{if} and Γ_{if}^a are equal in magnitude within the framework of atomic units used here (appendix A1). It should be pointed out that the transition rate as well as the transition energy are defined for isolated atoms and, hence, they are typical atomic structure quantities.

The concept of widths is very useful in the field of Auger and X-ray spectroscopy. If there are several Auger decay channels for a given initial state, the corresponding partial Auger widths add to the *Auger width*

$$\Gamma_i^a = \sum_f \Gamma_{if}^a \quad (1.2.1)$$

of the initial state. Analogously, the *Coster-Kronig width* Γ_i^c and the radiative width Γ_i^x are obtained. These widths contribute to the *total width*

$$\Gamma_i = \Gamma_i^a + \Gamma_i^c + \Gamma_i^x \quad (1.2.2)$$

of the initial state. Then, it follows for the *natural line width*

$$\Gamma(i, f) = \Gamma_i + \Gamma_f \quad (1.2.3)$$

of an Auger line, where Γ_f is the total width of the final states which may further decay. The difference between the partial width Γ_{if}^a and the natural line width $\Gamma(i, f)$ should be noted. The partial width Γ_{if}^a is uniquely specified by the initial and the final state, whereas $\Gamma(i, f)$ depends on transitions other than from i to f and/or on radiative transitions.

The branching ratio into a specific Auger channel is the *partial Auger yield*

$$a_{if} = \Gamma_{if}^a / \Gamma_i \quad (1.2.4)$$

The decay in all Auger channels defines the *Auger yield*

$$a_i = \Gamma_i^a / \Gamma_i \quad (1.2.5)$$

Similarly, the *Coster-Kronig yield* f_i and the *fluorescence yield* ω_i are obtained. From eq. (1.2.2) it is seen that

$$a_i + f_i + \omega_i = 1.$$

It should be emphasized that a_i , f_i and ω_i are defined for individual states. For instance, the Auger yield for a given (open) shell is usually a mean value:

$$\bar{a}_I = \sum_i Q_i a_i \tag{1.2.5a}$$

where Q_i is the excitation probability for state i , with $\sum_i Q_i = 1$. The label i runs over all states associated with a vacancy in the shell labeled I. Analogous definitions yield the mean Coster-Kronig yield \bar{f}_I and the mean fluorescence yield $\bar{\omega}_I$.

Information about the widths and yields are obtained from the related line spectra. A transition from an initial state to a final state gives rise to a specific line whose intensity I_{if} is a measure for the corresponding excitation probability and branching ratio. For instance, the Auger line intensity is obtained by

$$I_{if}^a = A Q_i a_{if} \tag{1.2.6}$$

where A is a proportionality constant characteristic for the instrument used to record the Auger spectrum. (The constant A may also depend on the electron observation angle.)

It is important to realize that the Auger line intensity is not proportional to the transition rate P_{if} , but it is proportional to the Auger yield a_{if} . Often, a_{if} is close to one, i.e. when the decay to *one* final state f dominates. In this case, the intensity I_{if} probes primarily the excitation probability Q_i . Information about the transition rate P_{if} may then be obtained from the analysis of the natural width of the Auger line.

Auger widths and radiative widths are given for the K-shell in fig. 3 taken from the compilation by

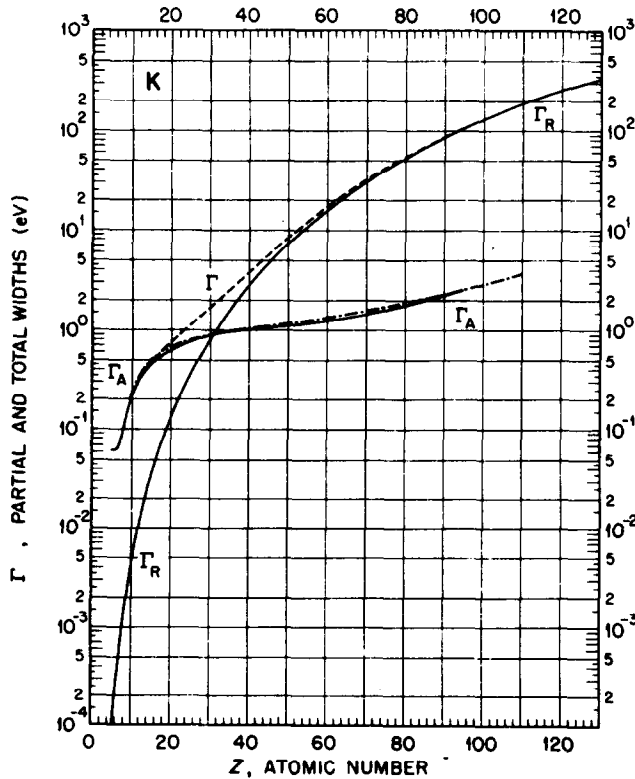


Fig. 3. Auger width Γ_A , radiative width Γ_R , and total width Γ for the K-shell. From the compilation by Krause [68].

Krause [68]. It is seen that the radiative width varies by more than six orders of magnitude within the Z range of the periodic table. In this range the Auger width varies only slightly. The near constancy of the Auger width is the outstanding feature of the electron–electron interaction causing the nonradiative transitions.

2. Theory of nonradiative transitions

2.1. Basic formalism

The following section is concerned with the principles of atomic structure calculations relevant for nonradiative transitions. Here, only a brief overview can be given. For more details the reader is referred to the fundamental textbooks by Condon and Shortley [69], Slater [70] and Hartree [71]. The present formalism is primarily based on nonrelativistic quantum mechanics. Relativistic theories are discussed in the reviews by Burhop and Asaad [5], Chatterji [6], Åberg and Howat [8], and Grant [72].

2.1.1. Hamiltonian and wave functions

Starting point for the theoretical treatment of atomic multi-electron system is the partition of the total Hamiltonian into terms consisting of one- and two-electron operators. Using essentially the notation by Condon and Shortley [69] one may set

$$H = F + Q \quad (2.1.1)$$

where

$$F = \sum_i f(i) \quad \text{and} \quad Q = \sum_{i>j} q(i, j).$$

The term $f(i)$ denotes a one-electron operator affecting the i th electron and $q(i, j)$ denotes a two-electron operator affecting the i th and j th electron.

The partition of the total Hamiltonian is generally performed within the framework of the independent particle model (IPM). Within this model an electron is considered to move independently from the others in the average potential produced by the nucleus and the other electrons. Let w_i be the electronic part of the average potential relevant for the i th electron. Thus, the IPM postulates the one-electron Hamiltonian

$$h(i) = \frac{1}{2} p_i^2 - Z/r_i + w_i \quad (2.1.2)$$

where Z is the nuclear charge, $p_i = -\nabla_i$ is the momentum operator of the i th electron and r_i is its radial coordinate. In general, the model Hamiltonian $h(i)$ is identified with the operator $f(i)$ where also spin–orbit interaction $\xi(r_i) (l_i s_i)$ may be included. When the effect of the potential w_i is small, $f(i)$ may be set equal to the ‘hydrogenic’ Hamiltonian $p_i^2/2 - Z/r_i$. Then, the operator $q(i, j)$ is identified primarily with the electron–electron interaction r_{ij}^{-1} where r_{ij} denotes the distance between the i th and j th electron. However, $q(i, j)$ may include also contributions from the Breit operator discussed further below.

Hence, the total Hamiltonian may be partitioned according to

$$H = H^0 + V^{\text{so}} + V^{\text{c}} \quad (2.1.3)$$

where

$$H^0 = \sum_i h(i), \quad V^{\text{so}} = \sum_i \xi(r_i) (l_i s_i)$$

and

$$V^{\text{c}} = V^{\text{e}} - W^{\text{e}}.$$

The operator V^{c} denotes the electronic 'rest' interaction obtained from the full electron–electron interaction $V^{\text{e}} = \sum_{i < j} r_{ij}^{-1}$ and the sum of the average potentials $W^{\text{e}} = \sum_i w_i$ postulated within the IPM.

When the model Hamiltonian H^0 is determined, care is to be taken to minimize the total energy of the system. In this sense, the best H^0 is obtained from the Hartree–Fock method [73, 74]. When H^0 is derived by the Hartree–Fock method, transitions initiated by the operator V^{c} are referred to as electron–correlation effects. It should be emphasized that Auger transitions and autoionization are prominent examples for electron–correlation effects.

The eigenfunctions of the Hamiltonian H^0 may be regarded as the zero-order approximations of the corresponding quantities for the total Hamiltonian H . For closed shells, the zero-order solutions are obtained by solving the one-electron Schrödinger equation

$$hu_i = \varepsilon_i u_i \quad (2.1.4)$$

where u_i is a spin orbital and ε_i is the corresponding orbital energy. The solution of eq. (2.1.4) is achieved by iterations, as the Hamiltonian h depends itself on the spin orbitals u_i . The iterative procedure is denoted as *self-consistent field* (SCF) method.

When w_i in eq. (2.1.2) is a central field potential, the spin orbital is specified by the well-known set of quantum numbers $\{nlm_l m_s\}$ and it factorizes according to

$$u_{nlm_l m_s} = R_{nl} Y_{lm_l} \chi_{m_s} \quad (2.1.4a)$$

where R_{nl} , Y_{lm_l} and χ_{m_s} denote the radial wave function, the spherical harmonics, and the spin wave function, respectively.

Then, the zero-order solutions of the multi-electron Schrödinger equation for the N -electron atom

$$H^0 \Psi_{\kappa\mu} = E_{\kappa}^0 \Psi_{\kappa\mu} \quad (2.1.5)$$

are obtained as

$$E_{\kappa}^0 = \sum_{i=1}^N \varepsilon_i \quad (2.1.5a)$$

and

$$\Psi_{\kappa\mu}(1, 2, \dots, N) = \det\{u_1(1) u_2(2) \cdots u_N(N)\}. \quad (2.1.5b)$$

This expression represents an antisymmetrized product of spin orbitals forming a Slater determinant [70] which implies the normalization factor $(N!)^{1/2}$. The label κ stands for the set of ‘radial’ quantum numbers and μ stands for the set of magnetic quantum numbers, i.e.

$$\kappa = \{n_1 l_1 \dots n_N l_N\} \quad (2.1.5c)$$

$$\mu = \{m_{l_1} m_{s_1} \dots m_{l_N} m_{s_N}\}. \quad (2.1.5d)$$

The energy E_κ^0 is degenerate with respect to the set of magnetic quantum numbers μ . Hence, it is dependent solely on the set of quantum numbers κ which stands for the *electronic configuration*. The association with the single electron configuration is the specific feature of the zero-order solutions from eq. (2.1.5).

For the treatment of relativistic effects, a few modifications of the formulas must be introduced. In eq. (2.1.2) the operator $p_i^2/2$ is replaced by the relativistic kinetic energy operator

$$c\alpha_i p_i + c^2 \beta_i \quad (2.1.6)$$

where α_i and β_i refer to 4×4 matrices defined within the framework of the Dirac theory [75]. Moreover, the electron–electron interaction r_{ij}^{-1} is replaced by the Møller operator

$$(1 - \alpha_i \alpha_j) \exp(iqr_{ij})/r_{ij}. \quad (2.1.7)$$

This interaction may be regarded as being produced by the retarded exchange of photons. The quantity q refers to the modulus of the photon propagation vector. For small q , the Møller operator is replaced by

$$1/r_{ij} + B_{ij} \quad (2.1.8)$$

with the *Breit* operator

$$B_{ij} = -\frac{\alpha_i \alpha_j}{r_{ij}} - \frac{(\alpha_i \nabla_i)(\alpha_j \nabla_j) r_{ij}}{2}. \quad (2.1.8a)$$

The first and second operator are denoted as *magnetic* term and *retardation* term, respectively.

The solution of the Dirac equation for a central potential yields relativistic (one-electron) orbitals of the form

$$u_{nkm} = \frac{1}{r} \begin{Bmatrix} P_{nk} \Omega_{km} \\ iQ_{nk} \Omega_{-km} \end{Bmatrix}. \quad (2.1.9)$$

The radial functions P_{nk} and Q_{nk} are the large and small component of the orbital, respectively. Moreover, eq. (2.1.9) implies spin–orbit functions

$$\Omega_{km} = \sum_{m_s} \langle l m_l m_s | j m \rangle Y_{l m_l} \chi_{m_s} \quad (2.1.9a)$$

where Clebsch–Gordon coefficients are used in the notation by Messiah [75]. In the relativistic treatment, the quantum number $k = (l - j)(2j + 1)$ replaces one-electron angular momenta j and l . In the following discussion, most conclusions remain valid, when relativistic effects are incorporated into the present formalism. In particular, the self-consistent field (SCF) methods may be used in conjunction with the Dirac equation yielding the Dirac–Fock (DF) method.

2.1.2. Angular momentum coupling

To improve the zero-order solutions one proceeds in two steps. First, the one-electron angular momenta are coupled to new angular momenta which are approximate constants of motion under the influence of the perturbation V^{so} and V^c . In practice, linear combinations of the zero-order solutions $\Psi_{\kappa\mu}$ are formed summing over the set μ of magnetic quantum numbers for a fixed configuration κ . The linear combinations are still solutions of eq. (2.1.5), since the energy E_{κ}^0 is degenerate with respect to the magnetic quantum numbers. The modified zero-order solutions are required as a basis when higher-order corrections are evaluated in the second step. Then, linear combinations are formed summing also over the set of quantum numbers κ . Thus, one allows for *configuration interaction* which is the characteristic effect of the perturbation V^c .

In table 1 different coupling schemes are compared. Each coupling procedure yields a new set of angular momentum quantum numbers, which refer to constants of motion or approximate constants of motion. For instance, the total angular momentum J and its component M are always good quantum numbers, since the corresponding operators commute with H . Further commuting angular momenta are obtained within each coupling scheme depending on the symmetry of the interaction involved.

Russel–Saunders or *LS*-coupling is suitable for low Z elements for which $V^c \gg V^{so}$. In this case, both $SLM_S M_L$ and $SLJM$ are sets of good quantum numbers. The set $SLJM$ is to be chosen when the spin–orbit interaction becomes noticeable. For $V^c \approx V^{so}$ it is required to use the intermediate coupling scheme considered further below. For high Z elements, V^{so} increases strongly so that $V^{so} \gg V^c$. Then, *jj*-coupling becomes suitable where the total angular momenta j_1, j_2, \dots of the single electrons are appropriate quantum numbers in addition to m_{j_1}, m_{j_2}, \dots or J and M . The components m_{j_1}, m_{j_2}, \dots cease to be good quantum numbers, when V^c becomes significant.

Hence, the procedure of angular momentum coupling yields expressions of the form [76]

$$\Psi_{\kappa\lambda}(1, 2, \dots N) = \sum_{\mu} U_{\mu}^{\lambda} \Psi_{\kappa\mu}(1, 2, \dots N) \tag{2.1.10}$$

where the expansion coefficients U_{μ}^{λ} constitute a unitary transformation which depends on the coupling schemes applied. The label λ stands for the new set of angular momenta which are constants of motion

Table 1
Comparison of different coupling schemes for angular momenta. Here, V^{so} and V^c refer to typical expectation values of spin–orbit interaction and electron correlation interactions, respectively. Z denotes the atomic numbers and IC stands for intermediate coupling

Coupling scheme	Z value range	Interactions	Quantum numbers
<i>LS</i>	low	$V^c \gg V^{so}$	$n_1 l_1, n_2 l_2, \dots LS \begin{cases} M_L M_S \\ JM \end{cases}$
IC	medium	$V^c \approx V^{so}$	$n_1 l_1, n_2 l_2, \dots \begin{cases} JM \\ m_{j_1}, m_{j_2}, \dots \end{cases}$
<i>jj</i>	high	$V^c \ll V^{so}$	$n_1 l_1 j_1, n_2 l_2 j_2, \dots \begin{cases} JM \\ m_{j_1}, m_{j_2}, \dots \end{cases}$

or approximate constants of motion, i.e.

$$\lambda = \{L_1 L_2 \dots M_1 M_2 \dots\}. \quad (2.1.10a)$$

The transformation (2.1.10) has the purpose to diagonalize the Hamiltonian interactions within the subspace spanned by the functions $\Psi_{\kappa\mu}$ when the magnetic quantum numbers are varied for a given configuration. In particular, *LS*-coupling and *jj*-coupling have essentially the effect to diagonalize the matrices formed by the elements $\langle \Psi_{\kappa\mu} | V^c | \Psi_{\kappa\mu'} \rangle$ and $\langle \Psi_{\kappa\mu} | V^{so} | \Psi_{\kappa\mu'} \rangle$, respectively. In the intermediate coupling procedure, *both* interaction matrices are diagonalized. This indicates that the different coupling schemes should not be regarded as being equivalent. In fact, *LS*- and *jj*-coupling emerge as special cases from the more general method of intermediate coupling.

The procedures involved in the *LS*- and *jj*-coupling schemes are unique only for two electrons (or vacancies). When more than two electrons (vacancies) are involved, additional effort is required to find a suitable coupling scheme. Particular care is needed when electrons (vacancies) occur in different open shells. Then, the set ω of additional quantum numbers (e.g. seniority [69]) has to be introduced to specify fully the states. In general, one may write for the *LS*-coupled states

$$\Psi_{\kappa\omega SLJM} = \sum_{\mu} U_{\mu}^{\omega SLJM} \Psi_{\kappa\mu}. \quad (2.1.11)$$

This equation is based on the *SLJM* scheme which differs from the *LSJM* scheme by a phase factor [69]. A similar relation may be set up for *jj*-coupling.

As an example for the Russel–Saunders scheme, two electrons or vacancies are coupled:

$$\Psi_{n_1 l_1 n_2 l_2 SLJM} = \sum_{m_1 m_2 m_{s_1} m_{s_2}} U_{m_1 m_2 m_{s_1} m_{s_2}}^{SLJM} \det\{u_1 u_2\} \quad (2.1.12)$$

where

$$U_{m_1 m_2 m_{s_1} m_{s_2}}^{SLJM} = \langle l_1 l_2 m_1 m_2 | LM \rangle \langle s_1 s_2 m_{s_1} m_{s_2} | SM_S \rangle \langle SLM_S M_L | JM \rangle.$$

The orbitals u_1 and u_2 are specified by $\{n_1 l_1 m_1 m_{s_1}\}$ and $\{n_2 l_2 m_2 m_{s_2}\}$, respectively. Similarly, *jj*-coupling yields

$$\Psi_{n_1 l_1 j_1 n_2 l_2 j_2 JM} = \sum_{m_1 m_{s_1} m_2 m_{s_2}} U_{m_1 m_{s_1} m_2 m_{s_2}}^{j_1 j_2 JM} \det\{u_1 u_2\} \quad (2.1.13)$$

where

$$U_{m_1 m_{s_1} m_2 m_{s_2}}^{j_1 j_2 JM} = \langle l_1 s_1 m_1 m_{s_1} | j_1 m_{j_1} \rangle \langle l_2 s_2 m_2 m_{s_2} | j_2 m_{j_2} \rangle \langle j_1 j_2 m_{j_1} m_{j_2} | JM \rangle.$$

The formulas show that the expansion coefficients U_{μ}^{λ} from eq. (2.1.10) are products of Clebsch–Gordon coefficients.

The transformation from *LS*- to *jj*-coupling is obtained by means of 9j-symbols [75]

$$\Psi_{n_1 l_1 j_1 n_2 l_2 j_2 JM} = \sum_{LS} [S, L, j_1, j_2]^{1/2} \begin{Bmatrix} s_1 s_2 S \\ l_1 l_2 L \\ j_1 j_2 J \end{Bmatrix} \Psi_{n_1 l_1 n_2 l_2 SLJM} \quad (2.1.14)$$

where the short notation

$$[S, L, j_1, j_2] = (2S + 1)(2L + 1)(2j_1 + 1)(2j_2 + 1)$$

is used.

The labor involved in the intermediate coupling method is facilitated when *LS*- or *jj*-coupling is performed before the diagonalization procedure is carried out. When *LS*-coupling is performed first, the states in intermediate coupling may be expressed as

$$\Psi_{\kappa\nu JM} = \sum_{\omega LS} U_{\omega SL}^{\nu J} \Psi_{\kappa\omega SLJM} \quad (2.1.15)$$

where ν stands for additional labels needed to specify the intermediate coupling states. The coefficients $U_{\omega SL}^{\nu J}$ are determined by diagonalization of the matrix formed by the quantities

$$H_{ij} = \langle \Psi_{\kappa\omega_i S_i L_i JM} | H | \Psi_{\kappa\omega_j S_j L_j JM} \rangle .$$

It is noted for *LS*-coupling that $H_{ij} = V_{ij}^{so}$ ($i \neq j$) where V_{ij}^{so} is defined analogously to H_{ij} .

For two states, the diagonalization may be carried out analytically. In this case, the expansion coefficients for the intermediate coupling states $\Psi_{\kappa\nu_1 JM}$ and $\Psi_{\kappa\nu_2 JM}$ are obtained as

$$U_{\omega_1 S_1 L_1}^{\nu_1 J} = U_{\omega_2 S_2 L_2}^{\nu_2 J} = \cos(\phi/2) \quad (2.1.16a)$$

$$U_{\omega_2 S_2 L_2}^{\nu_1 J} = -U_{\omega_1 S_1 L_1}^{\nu_2 J} = \sin(\phi/2) \quad (2.1.16b)$$

with

$$\tan \phi = \frac{2H_{12}}{(H_{11} - H_{22})} . \quad (2.1.16c)$$

Moreover, the diagonalization yields the eigenenergies for the intermediate coupling:

$$E_{1,2} = \frac{H_{11} + H_{22}}{2} \pm \left[\left(\frac{H_{11} - H_{22}}{2} \right)^2 + H_{12}^2 \right]^{1/2} . \quad (2.1.17)$$

Methods to evaluate the matrix elements are discussed further below.

2.1.3. Matrix elements

Important quantities in the atomic structure calculations are the Hamiltonian matrix elements:

$$H_{\kappa\lambda, \kappa'\lambda'} = \langle \Psi_{\kappa\lambda} | H | \Psi_{\kappa'\lambda'} \rangle . \quad (2.1.18)$$

For the states $\Psi_{\kappa\lambda}$ it is assumed that appropriate angular momentum coupling is already incorporated. This has the consequence that the off-diagonal matrix elements $H_{\kappa\lambda,\kappa\lambda'}$ ($\lambda \neq \lambda'$) for a fixed configuration κ are small.

Using eq. (2.1.10) the quantities $H_{\kappa\lambda,\kappa\lambda'}$ may be expanded in terms of the matrix elements obtained from single determinant states:

$$H_{\kappa\mu,\kappa'\mu'} = \langle \Psi_{\kappa\mu} | H | \Psi_{\kappa'\mu'} \rangle. \quad (2.1.19)$$

From eq. (2.1.1) it follows that

$$H_{\kappa\mu,\kappa'\mu'} = F_{\kappa\mu,\kappa'\mu'} + Q_{\kappa\mu,\kappa'\mu'} \quad (2.1.19a)$$

where the latter matrix elements are defined analogously to $H_{\kappa\mu,\kappa'\mu'}$. To evaluate these matrices it is assumed that the wave functions $\Psi_{\kappa\mu}$ and $\Psi_{\kappa'\mu'}$ are constructed of spin orbitals which belong to the same basis set. This is synonymous with the assumption that the orbitals are frozen. In the calculations of the matrix elements the frozen orbital approach, which implies the orthonormality of the spin orbitals, plays an important role. Non-zero results for the matrix elements are obtained for three cases:

(i) The functions $\Psi_{\kappa\mu}$ and $\Psi_{\kappa'\mu'}$ are identical, i.e. the matrix elements are diagonal:

$$F_{\kappa\mu,\kappa\mu} = \sum_i \langle u_i | f | u_i \rangle \quad (2.1.20a)$$

$$Q_{\kappa\mu,\kappa\mu} = \sum_{i>j} \{ \langle u_i u_j | q | u_i u_j \rangle - \langle u_i u_j | q | u_j u_i \rangle \}. \quad (2.1.20b)$$

(ii) The functions $\Psi_{\kappa\mu}$ and $\Psi_{\kappa'\mu'}$ differ in one spin orbital, i.e. $u_a \neq u_c$:

$$F_{\kappa\mu,\kappa'\mu'} = \langle u_a | f | u_c \rangle \quad (2.1.21a)$$

$$Q_{\kappa\mu,\kappa'\mu'} = \sum_i \{ \langle u_a u_i | q | u_c u_i \rangle - \langle u_a u_i | q | u_i u_c \rangle \}. \quad (2.1.21b)$$

(iii) The functions $\Psi_{\kappa\mu}$ and $\Psi_{\kappa'\mu'}$ differ in two spin orbitals, i.e. $u_a \neq u_c$ and $u_b \neq u_d$:

$$F_{\kappa\mu,\kappa'\mu'} = 0 \quad (2.1.22a)$$

$$Q_{\kappa\mu,\kappa'\mu'} = \langle u_a u_b | q | u_c u_d \rangle - \langle u_a u_b | q | u_d u_c \rangle. \quad (2.1.22b)$$

When more than two pairs of unlike spin orbitals occur, $Q_{\kappa\mu,\kappa'\mu'}$ as well as $F_{\kappa\mu,\kappa'\mu'}$ vanish since the corresponding operators do not affect more than two electrons.

As an example for the one-body operator $f(i)$ the spin orbit interaction $\xi(r_i)l_i s_i$ is considered. When the electrons are described by central-field spin orbitals (2.1.4a), the matrix elements split into a radial part and an angular part:

$$\langle u_a | \xi(r) l s | u_b \rangle = \delta_{l_a l_b} \xi_{n_a l_a n_b l_b} C_{l_a m_a m_s_a l_b m_b m_s_b} \quad (2.1.23)$$

with $l = l_a = l_b$. The angular coefficient

$$C_{lm_l m_s l m_l m_s} = \langle Y_{lm_l} \chi_{m_s} | \mathbf{ls} | Y_{lm_l} \chi_{m_s} \rangle \quad (2.1.23a)$$

may be evaluated using the spin-orbit function Ω_{km} from eq. (2.1.9a) in conjunction with the relation

$$\langle \Omega_{km} | \mathbf{ls} | \Omega_{km} \rangle = \frac{1}{2} \{ j(j+1) - l(l+1) - s(s+1) \}.$$

Furthermore, the radial coefficients are obtained as

$$\xi_{n_a l n_b l} = \langle R_{n_a l} | \xi(r) | R_{n_b l} \rangle. \quad (2.1.23b)$$

A particular notation is used for the diagonal term ($n = n_a = n_b$):

$$\zeta_{nl} = \langle R_{nl} | \xi(r) | R_{nl} \rangle \quad (2.1.23c)$$

known also as *spin-orbit parameter*.

As an example for the two-body operator $q(i, j)$ the electron-electron interaction r_{ij}^{-1} is inspected. This interaction may be evaluated using the expansion [69]

$$r_{ij}^{-1} = \sum_{km_k} \frac{4\pi}{2k+1} \frac{r_{<}^k}{r_{>}^{k+1}} Y_{km_k}(i) Y_{km_k}(j) \quad (2.1.24)$$

where $r_{<} = \min(r_i, r_j)$ and $r_{>} = \max(r_i, r_j)$. Then, it follows that

$$\begin{aligned} \langle u_a u_b | r_{ij}^{-1} | u_c u_d \rangle &= \delta(m_{s_a}, m_{s_c}) \delta(m_{s_b}, m_{s_d}) \delta(m_{l_a} + m_{l_b}, m_{l_c} + m_{l_d}) \\ &\quad \times \sum_{k=k_0}^{k_m} c^k(l_a m_{l_a}, l_c m_{l_c}) c^k(l_b m_{l_b}, l_d m_{l_d}) R^k(ab, cd) \end{aligned}$$

where $k_0 = \max(|l_a - l_c|, |l_b - l_d|)$ and $k_m = \min(l_a + l_c, l_b + l_d)$. Furthermore,

$$c^k(l_a m_{l_a}, l_c m_{l_c}) = \langle Y_{l_a m_{l_a}} | Y_{km_k} | Y_{l_c m_{l_c}} \rangle \quad (2.1.25a)$$

with $m_k = m_{l_a} + m_{l_b}$ and $k + l_a + l_c = \text{even}$. It follows from the Wigner-Eckert theorem [75] that

$$c^k(l_a m_{l_a}, l_b m_{l_b}) = \frac{\langle l_b k m_{l_b} m_k | l_a m_{l_a} \rangle}{\sqrt{2l_a + 1}} \langle l_a || C^k || l_b \rangle \quad (2.1.25b)$$

with the reduced matrix element of the spherical harmonics:

$$\langle l_a || C^k || l_b \rangle = (-1)^{l_a} [(2l_a + 1)(2l_b + 1)]^{1/2} \begin{pmatrix} l_a & k & l_b \\ 0 & 0 & 0 \end{pmatrix} \quad (2.1.25c)$$

where 3j-symbols are used. Techniques to evaluate the angular coefficients c^k and numerical results are given in various textbooks [69, 70]. It is noted that the coefficients c^k are independent of the atomic system under consideration. Specific properties of the atom enter only into the radial coefficient

$$R^k(ab, cd) = \left\langle R_{n_a l_a} R_{n_b l_b} \left| \frac{r_{<}^k}{r_{>}^{k+1}} \right| R_{n_c l_c} R_{n_d l_d} \right\rangle \quad (2.1.26)$$

which is known as *general Slater integral* [70].

In atomic structure calculations particular attention is paid to the ‘diagonal’ matrix elements of r_{ij}^{-1} for which a specific notation has been introduced [69]

$$J_{ab} = \langle u_a u_b | r_{ij}^{-1} | u_a u_b \rangle \quad (2.1.27a)$$

$$K_{ab} = \langle u_a u_b | r_{ij}^{-1} | u_b u_a \rangle. \quad (2.1.27b)$$

Furthermore, the ‘diagonal’ matrix elements

$$F^k(ab) = R^k(ab, ab) \quad (2.1.28a)$$

$$G^k(ab) = R^k(ab, ba) \quad (2.1.28b)$$

have been introduced as F and G integrals [69]. From eq. (2.1.25) it is seen that J_{ab} and K_{ab} may be expressed in terms of the F and G integrals, respectively.

2.1.4. Total energy and configuration interaction

In the following, specific applications are considered where the Hamiltonian matrix elements $H_{\kappa\lambda, \kappa'\lambda'}$ enter into the analysis. The diagonal elements of the Hamiltonian matrix may be used to obtain the first-order approximation $E_{\kappa\lambda}^1 = H_{\kappa\lambda, \kappa\lambda}$ of the total energy. From eq. (2.1.3) it follows that

$$E_{\kappa\lambda}^1 = E_{\kappa}^0 + E_{\kappa\lambda}^c + E_{\kappa\lambda}^{\text{so}} \quad (2.1.29)$$

where the corrections $E_{\kappa\lambda}^c$ and $E_{\kappa\lambda}^{\text{so}}$ refer to the interactions V^c and V^{so} , respectively. The first-order corrections remove most degeneracies involved in the zero-order solutions. For instance, $E_{\kappa\lambda}^c$ produces the term splitting and $E_{\kappa\lambda}^{\text{so}}$ produces the multiplet splitting characteristic for LS -coupling.

To calculate $E_{\kappa\lambda}^c$ in eq. (2.1.29), the average value of the electron–electron interaction V^c is considered first:

$$E_{\kappa, \text{av}}^c = N_{\kappa}^{-1} \sum_{\lambda} E_{\kappa\lambda}^c \quad (2.1.30)$$

where $E_{\kappa\lambda}^c = \langle \Psi_{\kappa\lambda} | V^c | \Psi_{\kappa\lambda} \rangle$ and N_{κ} is the number of terms in the sum of eq. (2.1.30). When $\Psi_{\kappa\lambda}$ are based on Hartree–Fock orbitals, it may be shown that $\langle \Psi_{\kappa\lambda} | W^e | \Psi_{\kappa\lambda} \rangle = 2E_{\kappa, \text{av}}^c$. This indicates that the sum W^e of (average) HF-potentials contains the electron–electron interaction twice [75]. The matrix element of W^e is independent of λ , since it is spherically symmetric. With eq. (2.1.3) it follows that

$$E_{\kappa\lambda}^c = E_{\kappa\lambda}^e - 2E_{\kappa, \text{av}}^c. \quad (2.1.31)$$

Expressions to deduce $E_{\kappa, \text{av}}^c$ are given in Slater’s textbook [70].

Equation (2.1.31) indicates that the mean energy $E_{\kappa, \text{av}}^c$ (defined as in eq. (2.1.30)) and $E_{\kappa, \text{av}}^e$ are

equal apart from a sign. Hence, it follows for the mean value of the total energy that

$$E_{\kappa,av}^1 = E_{\kappa}^o - E_{\kappa,av}^e + E_{\kappa,av}^{so} \quad (2.1.32)$$

This shows that $E_{\kappa,av}^1$ and E_{κ}^o differ significantly. Also, E_{κ}^o contains the electron–electron interaction twice. Hence, in atomic structure calculations, $E_{\kappa,av}^1$ instead of E_{κ}^o is often regarded as the zero-order approach to the total energy.

It is noted that the trace of a matrix is invariant with respect to a unitary transformation such as that given by eq. (2.1.10). Hence, the average value of the diagonal matrix elements is independent of the coupling scheme applied. For instance, in *LS*-coupling $E_{\kappa,av}$ is identified with the term averaged energy [70].

The nondiagonal matrix elements $H_{\kappa\lambda,\kappa'\lambda'}$ ($\kappa \neq \kappa'$) govern the coupling between configurations. To treat configuration interaction (CI) it is useful to consider the spectrum of eigenvalues resulting from eqs. (2.1.5) and (2.1.29). In fig. 4 the possible CI's are indicated schematically and in fig. 5 the

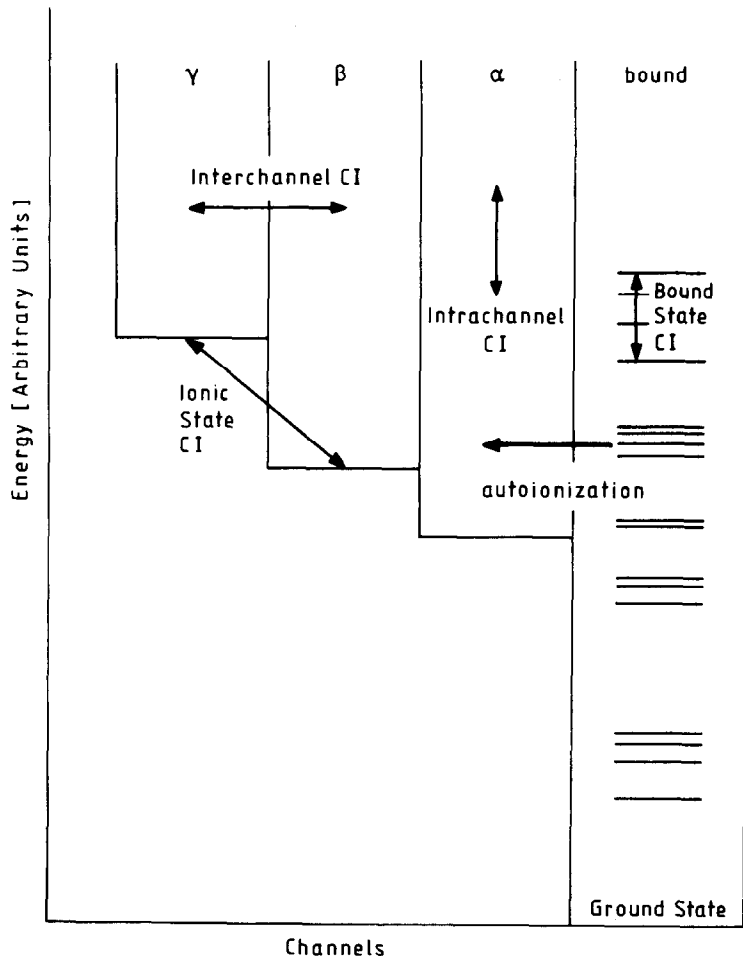


Fig. 4. Schematic Auger transition diagram illustrating different types of configuration interaction (CI). The columns labelled α , β and γ refer to different channels.

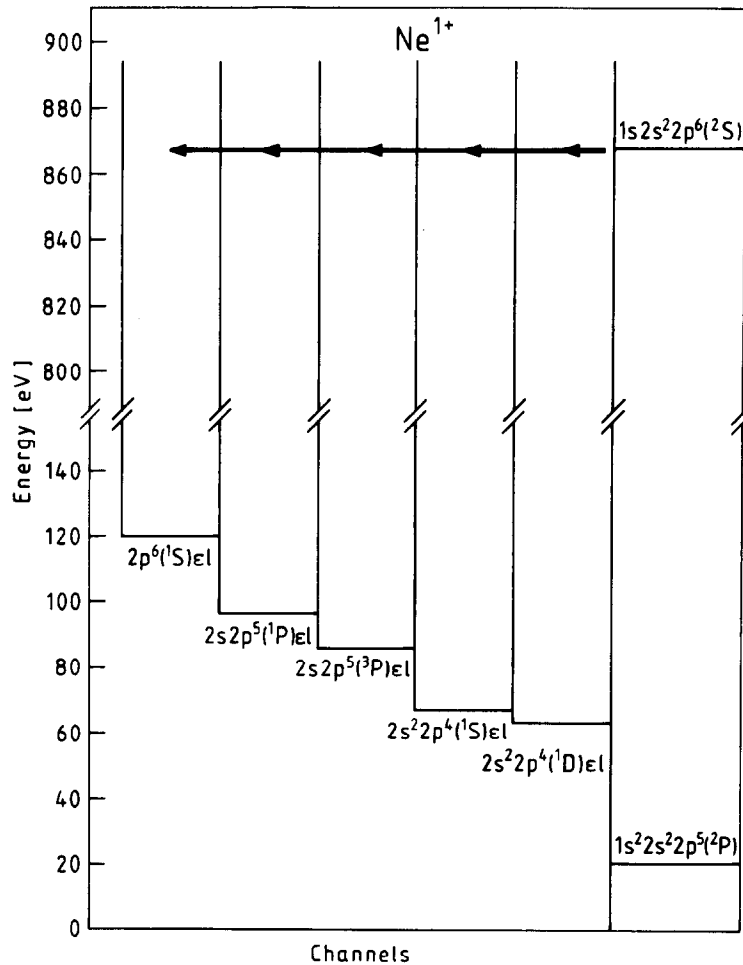


Fig. 5. Auger transition diagram for Ne^{1+} showing bound states and different series of continuum states. The columns denoted channels are specified by the states of the residual ion. The horizontal arrows represent Auger transitions.

configuration spectrum is shown for Ne as an example [13, 32]. In the right-hand column of fig. 4 the energies of the configurations are given where both electrons occupy bound states. The left-hand side shows columns which imply at least one electron in a continuum state. These columns are denoted as channels labeled α , β and γ etc. Each channel is specified by the bound state of the residual ion.

Configuration interaction occurs between bound states ordered vertically in the right-hand column, e.g. between $2s^2 {}^1S$ and $2p^2 {}^1S$ for He. Similarly, *intrachannel* CI occurs vertically between states $1s\epsilon l$ and $1s\epsilon' l$ in one column attributed to a channel. Furthermore, *interchannel* CI takes place between states of two different channels, e.g. $1s\epsilon l$ and $2s\epsilon' l$ having about the same energies. This interaction is represented by a (near) horizontal arrow connecting two channels. In atoms with more than two electrons, *ionic state* CI may occur between the bound states of the residual ion. This type of CI is represented by an arrow connecting the ionic states of two different channels.

Finally, CI may occur between a bound state and a continuum state located in a channel. This interaction constitutes the basis underlying the Auger transition or autoionization. It is represented by horizontal arrows in figs. 4 and 5. (Here, the spectroscopic convention is used to place the initial state

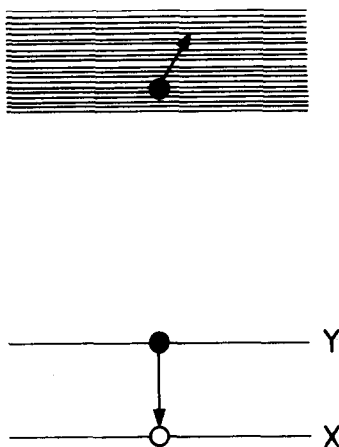


Fig. 6. Transition diagram illustrating the free-free Auger transition caused by interchannel configuration interaction.

on the right-hand side from the final state.) Thus, it is emphasized that the Auger effect or autoionization refer to a specific type of configuration interaction. In fact, Fano [32] showed by means of the technique by Rice [77] that a rigorous treatment of autoionization proceeds along the line of the usual method treating configuration interaction.

The process of configuration interaction involving a continuum electron may also be considered from another point of view. The mechanism underlying the interchannel CI is due to a transition between continuum states depicted in fig. 6. When the vacancy in X is filled, the excess energy is given to a continuum electron resulting in an increase of its kinetic energy. This process may be regarded as a free-free (Auger) transition. It is obtained by time reversing the well-known process of inelastic electron scattering.

Likewise the ordinary Auger process or autoionization can be viewed as elastic electron scattering involving a resonance. (When excitation and decay are independent processes the Auger process or autoionization may be considered as a half collision event.) Hence, radiationless transitions may be treated theoretically within the framework of scattering theory. Characteristic feature of the scattering approach is that interchannel CI may readily be incorporated in the analysis. In the past, multichannel scattering calculations have primarily been performed to treat autoionization discussed in detail by Burke [4]. Only recently, scattering approach to the Auger process has been worked out by Åberg [78] and Åberg and Howat [8].

2.2. Transition energies

The Auger transition energy may be evaluated from the energies of the related multi-electron states of the atom. Let $E_i^{(N)}$ and $E_f^{(N)}$ be such energies associated with the initial and final state of the atomic N -electron system, respectively. From the law of energy conservation it follows that $E_i^{(N)} = E_f^{(N)}$ which merely reflects the fact that the Auger transition takes place in a conservative system. The energy of the final system splits into the energy $E_f^{(N-1)}$ of the residual ion and the energy ϵ_a of the ejected electron. Then, it follows that

$$\epsilon_a = E_i^{(N)} - E_f^{(N-1)}. \tag{2.2.1}$$

Hence, the transition energy ϵ_a is determined by calculating separately the energy of the initial state and the energy of the final ionic state.

With regard to eq. (2.2.1) it is convenient to exhibit Auger transition with the framework of a level diagram [79] showing the energies for each charge state of the atom in a separate column [80]. An example [11] is given in fig. 7 for Ne which is the atom studied most extensively in the field of Auger spectroscopy. A specific Auger transition is associated with an arrow connecting states in adjacent columns. (Again, the spectroscopic convention is used that the initial state is placed on the right-hand side of the final state.) Each arrow may be associated with a line in the corresponding Auger spectrum.

To set up an Auger transition diagram, care has to be taken to relate the energy levels to a common zero of energy. Generally, in computations of total energies the zero of energy is attributed to the totally stripped nucleus. Thus, the total energies are negative as well as the orbital energies in accordance with eq. (2.1.5a). Alternatively, the zero of energy may be attributed to the ground state of the neutral atom. Then, the energies of the excited states are positive as in fig. 7.

There are different methods to determine transition energies for multi-electron systems. First semiempirical methods are used relating the relevant energies to experimental and theoretical values extracted from different sources such as tables of spectroscopic data. Second, the energies are evaluated explicitly by means of the atomic structure formalism outlined in the foregoing section. In particular,

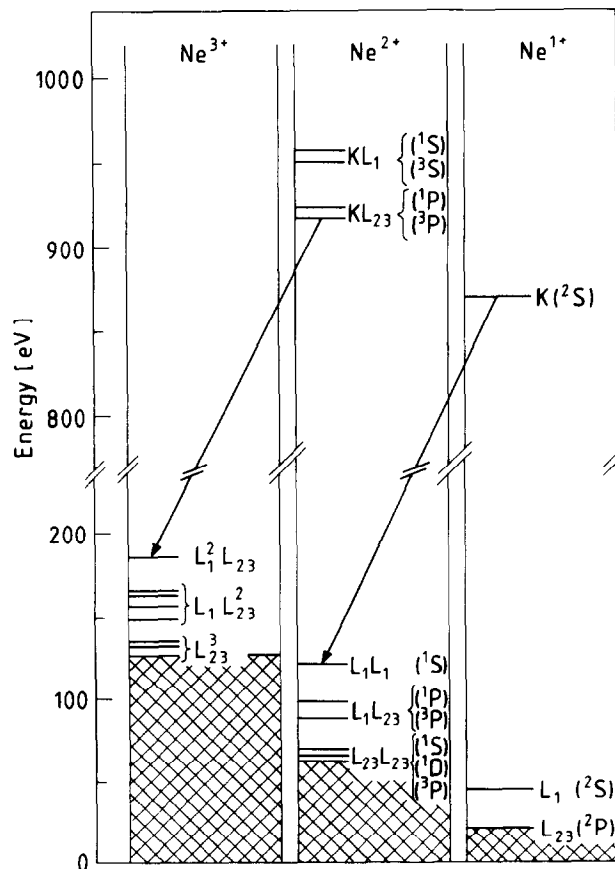


Fig. 7. Auger transition diagram showing bound states of Ne¹⁺, Ne²⁺ and Ne³⁺. The arrows represent specific Auger transitions.

ab-initio methods are applied using Hartree–Fock or Dirac–Fock codes. Some of these methods will be discussed in the following.

2.2.1. Semiempirical methods

When the zero energy is attributed to the ground state of the N -electron atom, the energy of the initial state is equal to the binding energy B_X of the electron to be removed from shell X. Likewise, the final state energy is equal to the sum of the binding energy B_Y of electron in shell Y and the binding energy $B_Z^{(Y)}$ of the electron to be removed from shell Z in an atom already ionized in shell Y. When the residual ion is excited, also the appropriate excitation energy is to be inserted into $B_Z^{(Y)}$. Hence, one obtains

$$\varepsilon_a = B_X - B_Y - B_Z^{(Y)}. \quad (2.2.2)$$

Also, B_Z may be used instead of $B_Z^{(Y)}$ when B_Y is replaced by $B_Y^{(Z)}$.

Experimental values for the binding energies B_X and B_Y may be obtained from tables given by Bearden and Burr [81] and Sevier [12]. Often, these data refer to atoms in the solid state, so that care should be taken when transition energies for isolated atoms are determined [82]. In cases where Koopmans' theorem [83] is valid, the binding energies may be replaced by the corresponding orbital energies [84].

Semiempirical methods to determine $B_Z^{(Y)}$ have been discussed by Bergström and Hill [85] and by Coghlan and Clausing [86]. The semiempirical methods have been proven to be quite successful for heavy atoms, but they fail usually for light atoms. In particular, problems arise with predictions concerning Coster–Kronig and Super-Coster–Kronig transitions [87].

When $B_Z^{(Y)}$ is not too different from B_Z , one may set approximately:

$$\varepsilon_a = B_X - B_Y - B_Z \quad (2.2.3)$$

as suggested also by fig. 1. Equation (2.2.3) has been given already by Auger [1].

The essential condition for the validity of eq. (2.2.3) is that the orbitals of the passive electron do not change (relax) during the Auger transition. The frozen orbital approach breaks down, when the Auger transition affects the screening of the nuclear charge resulting in an alteration of the electronic orbitals. Generally, the relaxation effects cause only small fractional changes in the orbital energies. However, to date the experimental techniques allow to determine the Auger electron energies with high accuracy so that the alterations of the orbital energies are noticeable.

2.2.2. Atomic structure calculations

Asaad and Burhop [88] and Asaad [89, 90] calculated explicitly transition energies for the K–LL group implying intermediate coupling and configuration interaction. The analysis may be considered as a classical example for the application of the atomic structure formalism (section 2.1). The procedure by Asaad and Burhop has been discussed in various reviews [5, 8, 13] so that only a brief description shall be given here.

For K–LL transitions the initial state is unique, whereas various possibilities exist for the final state. The LS -coupling scheme yields 6 states whose energies are obtained as follows:

$$(1) \quad 2s^{-2}(^1S^e): \quad 2B_{2s} + F^0(2s, 2s)$$

$$\begin{aligned}
(2) \quad 2s^{-1}2p^{-1}(^1P^o): & \quad B_{2s} + B_{2p} + F^0(2s2p) + \frac{1}{3}G^1(2s2p) \\
(3) \quad 2s^{-1}2p^{-1}(^3P^o): & \quad B_{2s} + B_{2p} + F^0(2s2p) - \frac{1}{3}G^1(2s2p) \\
(4) \quad 2p^{-2}(^1S^e): & \quad 2B_{2p} + F^0(2s2p) + \frac{2}{5}F^2(2p2p) \\
(5) \quad 2p^{-2}(^1D^e): & \quad 2B_{2p} + F^0(2p2p) + \frac{1}{25}F^2(2p2p) \\
(6) \quad 2p^{-2}(^3P^e): & \quad 2B_{2p} + F^0(2p2p) - \frac{1}{5}F^2(2p2p).
\end{aligned}$$

The transition energies are obtained by subtracting the above expressions from the binding energy B_{1s} of the 1s electron in the neutral atom. In (pure) LS -coupling, no transition is possible to the $^3P^e$ state because it does not conserve parity as shown in the next section.

Asaad and Burhop [88] noted that several pairs of states for equal configuration, J -value, and parity mix in the intermediate coupling scheme:

$$(^1P_1^o, ^3P_1^o), \quad (^1S_0^e, ^3P_0^e) \quad \text{and} \quad (^1D_2^e, ^3P_2^e). \quad (2.2.4)$$

The interaction of these states gives rise to two-by-two submatrices which may be diagonalized separately using the analytic solutions given in section 2.1. From eq. (2.1.17), closed form expressions for the Auger-transition energies are obtained for 10 states formed by intermediate coupling. (Due to the selection rules, transitions are possible to 9 states only.) As an example, the expressions for the pair $(^1S_0^e, ^3P_0^e)$ with $J=0$ and even parity are given [88]:

$$2p^{-2}(^1S_0^e): \quad 2B_{2p_{1/2}} + F^0(2p2p) + 0.1F^2(2p2p) - 1.5\zeta_{2p} + [(0.3F^2(2p2p) - 0.5\zeta_{2p})^2 + 2\zeta_{2p}^2]^{1/2} \quad (2.2.5a)$$

$$2p^{-2}(^3P_0^e): \quad 2B_{2p_{3/2}} + F^0(2p2p) + 0.1F^2(2p2p) + 1.5\zeta_{2p} - [(0.3F^2(2p2p) - 0.5\zeta_{2p})^2 + 2\zeta_{2p}^2]^{1/2}. \quad (2.2.5b)$$

The expressions for the other states are deduced in ref. [88]. The quantity $\zeta_{2p} = 2(B_{2p_{1/2}} - B_{2p_{3/2}})/3$ is the spin-orbit parameter. Of course, in intermediate coupling L and S cease to be good quantum numbers. In the expressions (2.2.5), the notations $^1S_0^e$ and $^3P_0^e$ are retained to indicate the states achieved asymptotically for $\zeta_{2p} \rightarrow 0$.

Asaad [90] proceeded a further step by including configuration interaction in the calculation of the K-LL transition energies. Inspecting the terms formed in LS -coupling it is seen that (1) and (4) are based on different configurations, but they are equal in the quantum numbers L , S , and parity. Hence, they mix under the influence of the electron-electron interaction. The interaction is governed by the off-diagonal matrix element [90]

$$\langle 2p^{-2}(^1S^e) | V^c | 2p^{-2}(^1S^e) \rangle = -\frac{1}{\sqrt{3}} G^1(2s2p)$$

which may again be accounted for by diagonalizing analytically the corresponding two-by-two matrix (eq. 2.1.17). However, the analytical treatment is not possible if electron-electron interaction as well as spin-orbit interaction are taken into account simultaneously. Then, the three states $2s^{-2}(^1S_0^e)$,

$2p^{-2}(^1S_0^e)$ and $2p^{-2}(^3P_0^e)$ have to be coupled. This coupling gives rise to a three-by-three matrix which is to be diagonalized using numerical methods [91].

In fig. 8 results from the Asaad-Burhop formalism are shown [41], see also in ref. [92]. In the analysis, experimental values were used for the binding energies and the spin-orbit interaction parameter. The F and G integrals were obtained from semiempirical expressions which were adjusted to fit various experimental data. It was found that the agreement between theory and experiment is quite satisfactory.

The importance of the analytic expressions given by Asaad and Burhop [88] is that they indicate the applicability of the different coupling schemes throughout the periodic table. For low Z , pure LS -coupling is valid giving rise to 5 K-LL Auger lines. In intermediate Z range, 9 Auger lines are produced which reduce to 6 lines in the high Z range where jj -coupling is applicable fairly well.

The major problem with the early calculations by Asaad and Burhop is that the relaxation of the passive electrons is partially ignored. Shirley [93] derived an additive relaxation term using the formalism by Hedin and Johansson [94] and he achieved an essential improvement in the agreement between experiment and the theoretical results. More recently, Larkins [95, 96] developed a rigorous

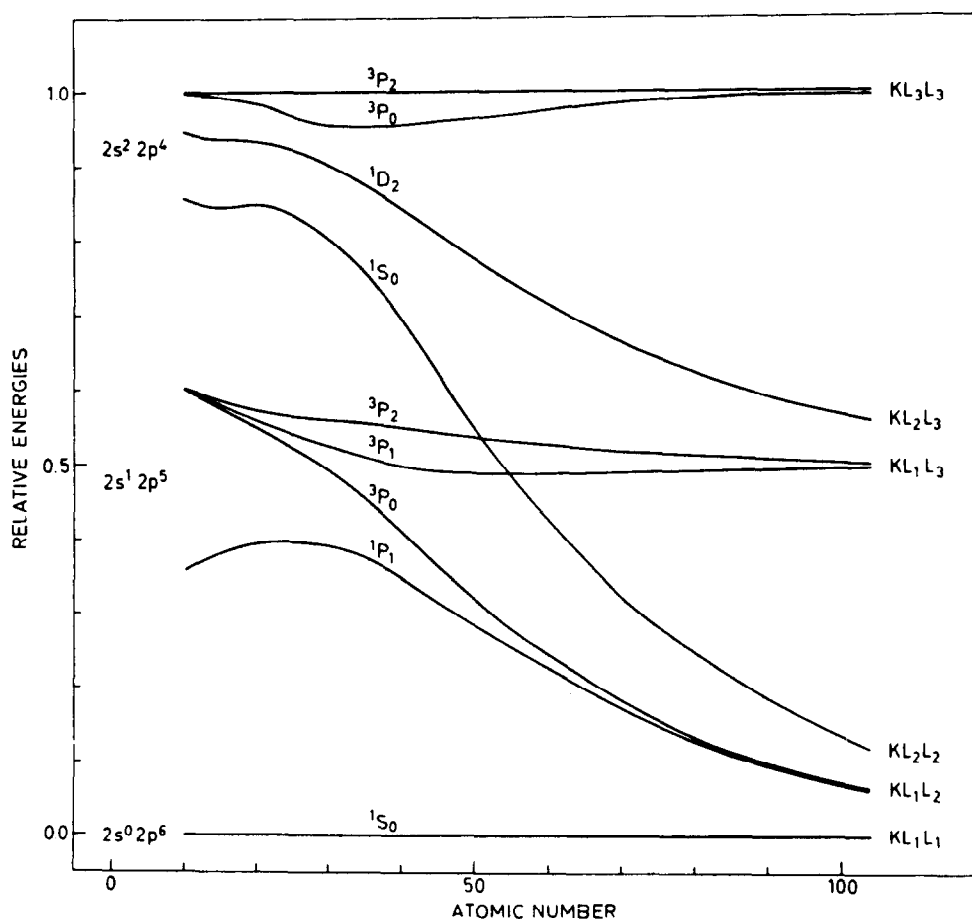


Fig. 8. K-LL transition energies relative to the lowest lying 1S_0 state. The data are obtained using the formalism by Asaad and Burhop [88]. From ref. [41].

method to determine the relaxation term including relativistic corrections. The need to modify the Asaad–Burhop procedure clearly shows that relaxation effects play an important role in the calculation of K–LL transition energies.

Accurate results for transition energies are obtained by means of ab-initio calculations using self-consistent field (SCF) methods. To date, extensive computer programs such as the nonrelativistic Hartree–Fock code by Froese-Fischer [97] and the relativistic Dirac–Fock code by Desclaux [98], Grant et al. [99] and Cowan [100], became available [101]. In the ab-initio methods, the relaxation effects are incorporated in a most natural way, when separate calculations are performed for the initial and final state, i.e. when the SCF orbitals are optimized specifically for the state under consideration. Note that the SCF method is based on a variational principle searching for the energy minimum of a given state whose choice implies a certain arbitrariness.

Thus, the results of the SCF procedure are not unique, when the initial and/or final state involve various closely-lying levels. In principle, the SCF procedure could be performed by each level separately consuming considerable computer time. However, generally in this case, a common set of orbitals is searched for by optimizing to the term averaged energy.

The SCF method may be extended to handle more than one configuration. In this case, states including configuration interaction are used within the SCF method to minimize the energy. The corresponding codes are denoted as multi-configuration Hartree–Fock (MCHF) or multi-configuration Dirac–Fock (MCDF). An alternative procedure to treat electron correlation effects has been established by Kelly [102] using many-body perturbation (MBPT) theory.

In table 2 theoretical results from the MCDF code by Briançon and Desclaux [103], from the MBPT approach by Kelly [102], and from the semiempirical method by Larkins [96] are compared with experimental results by Mehlhorn et al. [104]. The overall agreement between theoretical and experimental data lies typically within 1 eV. It is seen that the MBPT results are in outstanding agreement with the experiment. This indicates that when results are needed whose accuracy is better than 1 eV, considerable effort is required to take electron correlation effects properly into account.

The comparison of the data in table 2 shows that relativistic and nonrelativistic calculations yield practically the same results. Hence, relativistic effect does not play a significant role for Ne. However, relativistic effects gain importance for heavier atoms. The leading quantum electrodynamic (QED) correction is due to the Lamb shift including the electron self-energy [105] and the vacuum

Table 2
Comparison of theoretical (a–c) and experimental (d) K–LL transition energies in Ne. The data are given in units of eV

Transition	Semi-empirical ^{a)} (eV)	MCDF ^{b)} (eV)	MBPT ^{c)} (eV)	Expt. ^{d)} (eV)
K–L ₁ L ₁ (¹ S)	747.0	747.5	748.2	748.4
K–L ₁ L ₂₃ (¹ P)	770.9	771.7	771.7	771.8
(³ P)	781.8	783.7	782.4	782.4
K–L ₂₃ L ₂₃ (¹ S)	800.9	801.8	801.3	800.8
(¹ D)	803.4	806.9	804.5	804.5
(³ P)	806.1	810.3	–	–

a) Larkins [96].

b) Briançon and Desclaux [103].

c) Kelly [102]

d) Mehlhorn et al. [104].

polarization [106]. The Lamb shift is a single-electron property originating from the coupling of the electronic system to the photon continuum. In addition, for systems with more than one electron, level shifts are produced by the Breit interaction (2.1.8) including the magnetic and retardation contribution. For heavier atoms in the periodic table, the energy shifts may reach values of some hundred eV. In this case, a careful analysis of the relativistic effects is required for an accurate determination of the transition energy.

For completeness it is added that, analogous to the Lamb shift, autoionizing states exhibit a level shift due to the coupling to the electron continuum. This (nonrelativistic) correlation effect is treated within the framework of the configuration-interaction theory by Fano [32] and the scattering approach by Åberg [78]. The level shift of Auger states due to the coupling to the electron continuum is about of the same magnitude as the corresponding Auger width. Hence, it is of particular importance for *Coster–Kronig* transitions as has recently been shown by Chen et al. [107].

Unfortunately, the shift due to the coupling to the electron continuum has no convenient name as the Lamb shift has. With the improvement of the energy resolution in the field of Auger spectroscopy, it is expected that the shift due to the coupling to the electron continuum will receive increasing attention. Hence it appears useful to introduce a specific notation for the shift due to the coupling with the electron continuum. One may consider to apply the general term ‘resonance shift’ in the present case. However, to be more specific it is favorable to use the notation ‘Auger shift’ for the effect produced by the coupling of the electron continuum.

2.3. Transition rates

The dynamics of the Auger process are characterized by the transition rate specifying the decay of an atom from the initial state to the final state. On the basis of first-order perturbation theory, Wentzel [3] derived an expression for the transition rate which became a prominent example of Fermi’s Golden Rule:

$$P_{if} = 2\pi S |\langle \Psi_f | V^e | \Psi_i \rangle|^2 \rho(\varepsilon). \quad (2.3.1)$$

The symbol S shall indicate that the square of the matrix element is to be averaged over the initial states and summed over the final states. The averaging and summing refers to the quantities not observed in the experiments, e.g. the magnetic quantum numbers or the angular momentum of the ejected electron.

In eq. (2.3.1) the operator V^e is used instead of V^c whose replacement does not affect the transition rate in the frozen orbital approach. The difference between V^e and V^c vanishes in the matrix element, since W^e is composed of *one*-body operators (eq. (2.1.3)) whereas the initial and final states differ by *two* pairs of spin orbitals. The energy density $\rho(\varepsilon)$ of the ejected electron depends on the normalization of the radial continuum orbitals $R_{\varepsilon l}$. In the following the normalization

$$\int R_{\varepsilon l} R_{\varepsilon' l} r^2 dr = \delta(\varepsilon' - \varepsilon)$$

is adopted for which follows that $\rho(\varepsilon) = 1$.

Auger transitions imply definite selection rules. In general, the initial state and the final state are specified by the total angular momenta J_i and J_f and their magnetic quantum number M_i and M_f ,

Table 3
Selection rules for autoionization and Auger transitions [108]. Labels are used denoting orbital angular momentum (L), spin (S), total angular momentum (J), its z -component (M), and parity (Π)

Interaction	ΔL	ΔS	ΔJ	ΔM	$\Delta \Pi$
Coulomb	0	0	0	0	no
Spin-orbit					
(Spin-other orbit)	0, ± 1	0, ± 1	0	0	no
Spin-spin	0, $\pm 1, \pm 2$	0, $\pm 1, \pm 2$	0	0	no
Hyperfine	0, $\pm 1, \pm 2$	0, ± 1	0, ± 1	0, ± 1	no

respectively. Also, parities Π_i and Π_f are good quantum numbers. Parity is even or odd depending on whether the sum of the one-electron orbital angular momenta $\sum_i l_i$ is an even or odd number. With these specifications the selection rules may be written as follows:

$$J_i = J_f, \quad M_i = M_f, \quad \Pi_i = \Pi_f \quad (2.3.2)$$

which account for the fact that total angular momentum and parity are constants of motion in a conservative atomic system. The selection rules for Auger transitions [108] are summarized in table 3. It should be recalled that the final state includes the ejected electron.

In the following, more or less severe restrictions are adopted in the calculations of the transition rate. The initial and final states are assumed to be represented by single configuration functions such as those given in eq. (2.1.10). The frozen orbital approach is retained, i.e. all orbitals, in particular that of the continuum electron, are based on a common potential. Generally, this potential is obtained by performing the SCF procedure with respect to the initial hole state. Furthermore, atoms are considered having nearly closed shell configurations. In particular, the initial state refers to a closed-shell atom having a single vacancy in an inner shell. The final state is due to an atom with two outer-shell vacancies and one continuum electron. These initial and final states refer to the important case of inner-shell ionization of rare gas atoms. The restrictions considered here simplify essentially the analysis so that the related formulas may readily be given in closed form. For cases concerning open-shell configurations the formalism increases considerably in complexity [109]. Steps beyond the present restrictions will be discussed in the final part of this section.

2.3.1. LS - and jj -coupling

First, the transition rate is considered for small spin-orbit interaction for which LS -coupling is valid. In the $SLJM$ -scheme the initial and final states are specified as follows (for convenience the ket notation is used):

$$|i\rangle \equiv |n_0 l_0^{-1} S_i L_i J_i M_i\rangle \quad (2.3.3a)$$

$$|f\rangle \equiv |(n_1 l_1^{-1} n_2 l_2^{-1} S L) \varepsilon l S_f L_f J_f M_f\rangle. \quad (2.3.3b)$$

In the initial state the angular momenta $L_i = l_0$ and $S_i = \frac{1}{2}$ are determined by the initial hole state. In the final state the two holes are coupled to the angular momenta L and S which, in turn, are coupled with the continuum electron (denoted by εl) to the final angular momenta L_f and S_f . In LS -coupling

particular selection rules have to be taken into account (table 3):

$$L_i = L_f \quad \text{and} \quad S_i = S_f \quad (2.3.4)$$

in addition to the general selection rules given by eq. (2.3.2). In the $LSM_L M_S$ -coupling scheme also $M_{L_i} = M_{L_f}$ and $M_{S_i} = M_{S_f}$ holds. The parity selection rule requires that

$$l_0 + l + l_1 + l_2 = \text{even} . \quad (2.3.5)$$

Hence, in LS -coupling the transition rate is obtained as

$$P_{if}^{LS} = 2\pi \sum_l |\langle f|V^e|i \rangle|^2 \quad (2.3.6)$$

where the initial and final states are given in eq. (2.3.3). It is seen that only the sum over l remains from the requirement of averaging over initial states and summing over final states. This follows from the selection rules and the fact that the matrix element in eq. (2.3.6) is independent of J and M .

Explicit calculations show that the final continuum electron may be recoupled so that it is replaced by a corresponding hole particle in the initial state [109]:

$$P_{if}^{LS} = 2\pi \frac{(2S+1)(2L+1)}{2(2l_0+1)} \sum_l |\langle n_1 l_1^{-1} n_2 l_2^{-1} LSJM | r_{12}^{-1} | n_0 l_0^{-1} \epsilon l^{-1} LSJM \rangle|^2 \quad (2.3.7)$$

where the selection rules (2.3.2) and (2.3.4) are already incorporated. It is seen that the recoupling of the continuum electron simplifies the matrix elements. Also, proper statistical factors are derived as expected from averaging over initial states and summing over final states. The recoupling method is commonly used in transition rate calculations.

Equation (2.3.7) may further be evaluated [110, 111] applying eq. (2.1.25) in conjunction with eq. (2.1.12). It follows that

$$P_{if}^{LS} = 2\pi \frac{(2S+1)(2L+1)}{2\tau(2l_0+1)} \sum_l \left| \sum_k \{ D^k(l_0 l_1 l_2 L) + (-)^{L+S} E^k(l_0 l_1 l_2 L) \} \right|^2 \quad (2.3.8)$$

with

$$D^k(l_0 l_1 l_2 L) = \langle l_0 \| C^k \| l_1 \rangle \langle l \| C^k \| l_2 \rangle \begin{Bmatrix} l_0 & l & L \\ l_2 & l_1 & k \end{Bmatrix} R^k(l_0 l_1 l_2) \quad (2.3.8a)$$

where 6j-symbols [75] are used, and $\tau=2$ for equivalent electrons 1 and 2, otherwise $\tau=1$. The amplitude E^k is obtained as D^k by exchanging the labels l_1 and l_2 throughout expression (2.3.8a). It should be added that an expression similar to eq. (2.3.8) is obtained for jj -coupling [8,89].

It is seen that the calculations of the transition rate require the determination of the radial integrals and various angular coefficients. The latter quantities may be extracted from tables given in current textbooks [69, 70]. The labour in the transition rate calculations lies in the evaluation of the radial integrals R^k . In early calculations, screened hydrogenic wave functions have been applied, see, for instance, the work by Callan [112] and Crasemann and coworkers [113–115]. Rubenstein [116] was first

Table 4
Comparison of theoretical (a–d) and experimental (e) K–LL transition rates of Ne. The data are given in units of 10^{-4} a.u. The notation CI stands for configuration interaction

Transition	LS coupling (a)	Ionic state CI (b)	Interch. and initial state		Expt. (e)
			CI (c)	Interch. CI (d)	
K–L ₁ L ₁ (¹ S)	8.16	6.1	4.9	4.5	5.1
K–L ₁ L ₂₃ (¹ P)	20.29	18.6	13.7	15.0	14.5
(² P)	5.49	5.7	4.9	7.0	5.3
K–L ₂₃ L ₂₃ (¹ S)	4.28	6.0	7.7	8.3	8.0
(¹ D)	56.72	51.9	49.3	55.0	51.5
(³ P)	0	0.001	–	–	0.04

- a) McGuire et al. [119].
b) Asaad [90] and Mehlhorn [13].
c) Kelly [102].
d) Howat et al. [136].
e) Krause et al. [60] and Gelius [125].

to apply SCF-orbitals which became commonly used later. In the early 1970's various studies of transition rates for closed-shell atoms have been made by Walters and Bhalla [117, 118], McGuire [119–122], and Chen and Crasemann [123]. Relativistic calculations of the K–LL transition rates have been performed by Bhalla and Ramsdale [124]. The previous work is summarized in the review by Burhop and Asaad [5].

In table 4 calculations by McGuire [119] for Ne K–LL transition rates are compared with experimental results by Krause et al. [66] using the total Auger width (eq. (2.1.1)) from Gelius [125]. The overall agreement between theory and experiment is good except for the final states $2s^{-2}1S$ and $2p^{-2}1S$. In these cases configuration interaction is important, as discussed further below. It should be noted that in *LS*-coupling, the transition to the state $2p^{-2}3P$ is not allowed, since with $l = 1$ the parity selection rule (2.3.5) is violated. However, experimentally a non-zero transition rate is observed for the $2p^{-2}3P$ state. This is understood within the framework of intermediate coupling.

2.3.2. Mixed and intermediate coupling

Single vacancies in (closed) shells other than the K-shell exhibit fine structure splitting which can usually be resolved experimentally. Consequently, the initial vacancy should be specified by its j -value, so that the jj -coupling scheme is favourable. When the final state is still given in the *LSJM*-scheme, one obtains the transition rate in the mixed coupling scheme proposed by Asaad and Mehlhorn [126],

$$P_{if}^{\text{mix}} = 2\pi \frac{2J+1}{2j_0+1} \sum_j |\langle n_1 l_1 n_2 l_2 LSJM | r_{12}^{-1} | n_0 l_0 j_0^{-1} \epsilon l j^{-1} JM \rangle|^2 \quad (2.3.9)$$

which may be evaluated in terms of *LS*-transition rates by expanding the initial state in *LS*-coupling terms (eq. (2.1.14)):

$$P_{if}^{\text{mix}} = 2 \frac{2l_0+1}{2j_0+1} \sum_j [L, S, j_0, j]^{1/2} \begin{Bmatrix} s_0 & s & S \\ l_0 & l & L \\ j_0 & j & J \end{Bmatrix} P_{if}^{LS} \quad (2.3.9a)$$

Likewise, P_{if}^{mix} may be evaluated in terms of the transition rate in jj -coupling [127]. Important application for the mixed coupling scheme is the Ar-L shell studied in detail experimentally by Ridder et al. [128].

The LS -coupling of the final state loses significance with increasing atomic number Z . In this case, it is favourable to adopt the intermediate coupling scheme by using expression (2.1.15) for the final state [8, 88]:

$$P_{if}^{IC} = 2\pi \frac{2J+1}{2(2l_0+1)} \sum_l \left| \sum_{L'S'} U_{LS}^{l'l} \langle n_1 l_1^{-1} n_2 l_2^{-1} L' S' JM | r_{12}^{-1} | n_0 l_0^{-1} \epsilon l^{-1} LSJM \rangle \right|^2. \quad (2.3.10)$$

The selection rules for LS -coupling reduce the sum over L' and S' to one term. The intermediate coupling state may also be inserted for the final state of the mixed coupling formula (2.3.9). Then, two possibilities exist to evaluate the matrix element. The jj - to LS -coupling transformation (2.1.14) is applied to the initial state as in eq. (2.3.9a). Alternatively, the intermediate coupling state is expressed over jj -coupling terms by an expansion analogous to that given in eq. (2.1.15). As expected, the first method is to be favoured for low Z atoms.

Intermediate coupling plays an important role in cases where transitions are forbidden by specific selection rules for LS -coupling. This is the case for the final state $2p^{-2} 3P$ noted already above. Intermediate coupling mixes various pairs of states shown by the expression (2.2.4). Again, as an example the pair ($1S_0, 3P_0$) is considered in more detail. Intermediate coupling produces states labelled ν_1 and ν_2 for which eq. (2.3.10) yields the corresponding transition rates:

$$P_{\nu_1}^{IC}(1S) = |U_{1S}^{\nu_1}|^2 P_{1S}^{LS} \quad (2.3.11a)$$

$$P_{\nu_2}^{IC}(3P) = |U_{1S}^{\nu_2}|^2 P_{1S}^{LS}. \quad (2.3.11b)$$

The coefficients $U_{1S}^{\nu_1} = \cos(\phi/2)$ and $U_{1S}^{\nu_2} = \sin(\phi/2)$ are determined from $\tan \phi = 2H_{12}/(H_{11} - H_{22})$, see eq. (2.1.16). The values for H_{ij} may be obtained by comparing eq. (2.1.17) with eq. (2.2.5). The nondiagonal matrix element H_{12} , which governs the mixing of the states, is proportional to the spin-orbit parameter ζ_{2p} . From $\zeta_{2p} \rightarrow 0$ it follows that $\phi \rightarrow 0$. Hence, as expected $P_{\nu_1}^{IC}(1S) \rightarrow P_{1S}^{LS}$ and $P_{\nu_2}^{IC}(3P) \rightarrow 0$ for vanishing spin-orbit interaction.

There is no definite solution to the problem whether intermediate coupling is required for the final state. To date, experimental transition rates [68, 129] are determined with an accuracy of the order of $\pm 10\%$. Within these limits deviation from the LS -coupling scheme for K-LL group becomes noticeable for Z values larger than about 25 [89]. Hence, for neutral Ne the transition rates are practically not affected by inclusion of intermediate coupling. Alternatively, when the calculations of the K-LL transition rates are based on jj -coupling, deviations between theory and experiment become noticeable for Z values smaller than about 55. This has been shown by Asaad and Petrini [130] who incorporated intermediate coupling into the relativistic treatment by Bhalla and Ramsdale [123].

Recently, relativistic transition rates including intermediate coupling have been studied systematically within the whole periodic table by Chen, Crasemann and collaborators [131–134]. In the calculations, the Dirac-Slater (DS) method as well as the Dirac-Fock (DF) method [70] are used to evaluate the relativistic orbitals (2.1.9). The electron-electron interaction is represented by the Møller operator (2.1.7). A summarizing discussion of the relativistic effects is given by Chen and Crasemann [134]. It is found that for total Auger widths, the relativistic effects tend to average out. Pronounced effects are

seen only at the very end of the periodic table. However, the partial widths are strongly influenced by relativistic effects when Z exceeds about 40. In this case, no characteristic trend is observed. It appears that each case needs a specific calculation including the particular properties of the transition studied.

2.3.3. Relaxation and electron correlation

Next, steps shall be discussed leading beyond the independent-particle frozen-orbital model considered so far. Howat et al. [135, 136] studied in detail effects arising from relaxed orbitals. In the analysis, two different sets of orbitals are used optimized separably to the initial and final configuration. As a consequence, care has to be taken with the non-orthonormality of the orbitals from the different sets and of the corresponding initial and final multi-electron states. In particular, the difference between the two operators V^c and V^e does not necessarily vanish so that the proper interaction operator $V^c = H - H^0$ has to be inserted back into eq. (2.3.1).

The analysis by Howat et al. [136] yields a correction to the frozen-orbital approach involving several one- and two-electron interaction matrix elements, whose evaluation requires additional effort. For Ne, the correction reduces the partial transition rate to the final state $2s^{-2}1S$ by about 10% which, however, is not sufficient to account for the difference between theory and experiment in that case.

Further improvements of the transition rate calculation are achieved when configuration interaction is incorporated in the analysis. As pointed out in section 2.1 there are different types of configuration interaction relevant for the final state: Ionic state CI, intrachannel CI, and interchannel CI. When the final state is based in HF-orbitals intrachannel CI may be disregarded [136]. However, the other types of configuration interaction have a definite influence on the transition rate.

The method by Asaad [90] to treat ionic state CI is already outlined in section 2.2. Under the influence of the interaction V^e , the LS -coupling states $2s^{-2}1S_0^e(\equiv 1S')$ and $2p^{-2}1S_0^e(\equiv 1S)$ mix to form the CI states

$$\Psi_1(1S') = C_{1S}^1 \Psi_{1S'} + C_{1S}^1 \Psi_{1S}$$

$$\Psi_2(1S) = C_{1S}^2 \Psi_{1S'} + C_{1S}^2 \Psi_{1S} .$$

Again, the new states are specified to indicate the terms asymptotically achieved for vanishing interaction V^e . Inserting these states as final states in eq. (2.3.7), one obtains the CI-transition rates

$$P_1^{CI}(1S') = |C_{1S}^1 P_{1S'}^{LS} + C_{1S}^1 P_{1S}^{LS}|^2 \quad (2.3.12a)$$

$$P_2^{CI}(1S) = |C_{1S}^2 P_{1S'}^{LS} + C_{1S}^2 P_{1S}^{LS}|^2 . \quad (2.3.12b)$$

The expansion coefficients may be calculated by means of eq. (2.1.16). For Ne, one obtains [90, 91]

$$C_{1S}^1 = C_{1S}^2 = 0.98 \quad \text{and} \quad C_{1S}^1 = -C_{1S}^2 = -0.17 .$$

From the magnitude and sign of the coefficients follows a $\sim 15\%$ reduction of the $2s^{-2}1S$ transition rate and an enhancement by the same amount of the $2p^{-2}1S$ transition rate. From table 4 it is seen that these alterations remove partially the disagreement between theory and experiment. Similar improvements have been found for low Z atoms, in general [90].

The remaining discrepancies between theory and experiment are attributed to the influence of

interchannel CI. This type of CI is understood by inspecting the final state in its original form given by expressions (2.3.3). It shows that L and S (as well as J and M) of the final ionic state are actually not good quantum numbers. In fact, only the quantum numbers of the total system *including* the ejected electron are constants of motion. Hence, states which differ in configurations, angular momentum L , and spin S exhibit couplings governed by the matrix element

$$\langle (n_1 l_1^{-1} n_2 l_2^{-1} L S) \varepsilon l J_f M_f | r_{12}^{-1} | (n'_1 l'_1^{-1} n'_2 l'_2^{-1} L' S') \varepsilon' l' J_f M_f \rangle .$$

The matrix element corresponds to the free-free (Auger) transition mentioned in conjunction with fig. 6.

The rules for the selection of the ionic quantum numbers are not so restrictive, they have to fulfill the usual triangular conditions for angular momentum coupling [75]. Thus, interchannel CI allows the coupling of various configurations and angular momenta of the final ionic state.

Interchannel CI for K-LL transitions have first been investigated by Kelly [102] using many-body perturbation theory in second order. In that work, also initial state CI has been incorporated. Kelly found that the interchannel CI between the states $(2s^{-2} 1S) \varepsilon s^2 S$ and $(2s^{-1} 2p^{-1} 1,3P) \varepsilon' p^2 S$ is nearly as large as the ionic state CI treated previously [90]. Thus, for Ne the remaining discrepancies between theory and experiment are nearly removed, as shown in table 4. A similar good agreement has been obtained by Howat and collaborators [136, 137] using a scattering approach in the description of the Auger process. Recent studies of final state channel interaction have been performed by Karim and Crasemann [138]. Furthermore, interchannel interaction is included in the many-body perturbation approach by Nicolaides and Mercouris [139] using the method of complex eigenvalues.

It should be recalled that, strictly, the formulas given here apply for closed-shell atoms only. Nevertheless, to a good approximation the formulas retain validity for open-shell atoms, when the initial and final state vacancies occur in closed shells [131–134]. However, in cases where the initial or final vacancies are produced in open shells, the formalisms have to be extended with respect to a suitable angular momentum coupling scheme. McGuire [109] derived general expressions adequate to treat various open-shell configurations in LS -coupling. The expressions are lengthy so that they shall not be given here.

In the past decade, several studies have been performed by McGuire [138–142], Chen, Crasemann and collaborators [143–150], and Bhalla [151–153] concerning transition rates in open-shell systems. These studies are of particular importance for the present work, since the field of energetic ion-atom collisions deals primarily with multiply ionized atoms.

3. Collision kinematics

3.1. Kinematics of projectile and target atom

The particles involved in ion-atom collisions are influenced by kinematic effects, since momentum and energy are exchanged between the particles during the collision. The kinematic quantities relevant for collision particles are depicted in fig. 9. The projectile of energy T_0 and velocity \mathbf{v}_0 is incident on the target atom at rest. The projectile is scattered by the angle β_1 . After the collision, it has the energy T_1 and the velocity \mathbf{v}_1 . Analogous quantities β_2 , T_2 and \mathbf{v}_2 are defined for the recoiling target atom. In an inelastic collision, the internal energy Q is transferred to the particles.

The kinematic quantities are related through the laws of energy and momentum conservation

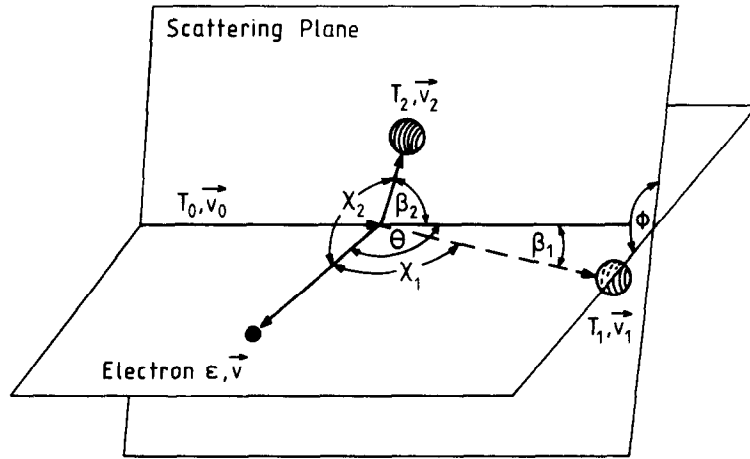


Fig. 9. Diagram used to define the kinematic parameter for the incident particle (label 0), the scattered particle (label 1), the recoil particle (label 2), and the ejected electron (no label).

$$T_0 = T_1 + T_2 + Q \quad (3.1.1a)$$

and

$$M_1 v_0 = M_1 v_1 + M_2 v_2 \quad (3.1.1b)$$

where M_1 and M_2 are the mass of the projectile and the target, respectively. It is noted that Q also includes the energy transferred to the electrons ejected during the collision. However, the momenta transferred to the ejected electrons are neglected in eq. (3.1.1b), since these momenta are generally small. In a high-precision analysis care should be taken with the electron momenta.

For a given incident energy T_0 and energy loss Q all kinematic quantities may be determined, if one of them is known, e.g. the scattering angle β_1 . Corresponding formulas are given in current textbooks [154]. Here, only a few expressions are extracted that are relevant for energetic collisions ($T_0 \gg T_2$ or Q).

The recoil angle β_2 is obtained by squaring both sides of eq. (3.1.1b) and replacing v_0^2 by $2T_0/M_1$ from eq. (3.1.1a). It follows that

$$\cos \beta = \frac{Q + (1 - \gamma)T_2}{2(\gamma T_1 T_2)^{1/2}} \quad (3.1.2)$$

where $\gamma = M_2/M_1$ and $\beta = \beta_1 + \beta_2$. For energetic collisions the right-hand side is much smaller than 1. Hence, the angle β is close to 90° . Since β_1 is generally small in high-energy collisions, the recoil angle β_2 is close to 90° , too.

The recoil energy T_2 may be obtained by taking into consideration that the (zero) momentum perpendicular to the incident beam direction is conserved in the collision, i.e.

$$M_1 v_1 \sin \beta_1 = M_2 v_2 \sin \beta_2. \quad (3.1.3)$$

With the conditions $v_1 \approx v_0 \cos \beta_1$ and $\beta_2 \approx 90^\circ - \beta_1$ valid for energetic collisions it follows for the recoil energy that

$$T_2 \approx (T_0/\gamma) \sin^2 \beta_1 . \quad (3.1.4)$$

It is seen that the recoil energy is strongly dependent on the scattering angle.

The foregoing analysis shows that, indeed, the kinematic quantities may be determined, if the scattering angle β_1 is known. However, information about β_1 is not readily accessible. To obtain such information, calculations are needed including knowledge about the excitation mechanism involved. Certain information about the scattering angle may be obtained from impact parameter studies where the internuclear motion is treated classically in an approximation.

For a given scattering potential it is possible to deduce the scattering angle as a function of the impact parameter. For instance, the pure Coulomb potential yields the relation

$$\tan (\beta_1^c/2) = Z_1 Z_2 / 2 T_0^c b \quad (3.1.5)$$

where Z_1 and Z_2 are the (screened) nuclear charges of the collision partners. The label c denotes quantities in the projectile-target center-of-mass reference system. Relations to convert quantities from the center-of-mass system to the laboratory system are given by

$$T_0^c = T_0 / (1 + \gamma) \quad (3.1.6a)$$

and

$$\tan \beta_1 = M_2 \sin \beta_1^c / (M_1 + M_2 \cos \beta_1^c) . \quad (3.1.6b)$$

It is noted that eq. (3.1.5) is valid for cases where electronic screening effects do not produce substantial deviations from the pure Coulomb potential. Otherwise a screened Coulomb potential is to be used and more elaborate numerical calculations are needed to determine the scattering angle.

In collisions, the scattering angle varies within a certain range. Usually, the cross section differential in β_1 exhibits a maximum at a characteristic value $\bar{\beta}_1$ which corresponds to the impact parameter \bar{b} . This quantity may be estimated by means of the Massey criterion

$$\bar{b} = v_0 / Q \quad (3.1.7)$$

where v_0 is the projectile velocity and Q is the excitation energy as above. It is not expected that the results from eq. (3.1.7) are highly accurate. However, since precise calculations are often tedious, eq. (3.1.7) may be considered as being a useful tool for obtaining rough estimates of the impact parameter.

Equations (3.1.5), (3.1.6) and (3.1.7) show that the product $T_0^{3/2} \sin \beta_1$ is approximately constant. However, in slow collisions implying potential energy curve crossings, the impact parameter does not vary significantly so that $T_0 \sin \beta_1$ is about constant [52]. Hence, it follows from eq. (3.1.4) that

$$T_2 = \text{const.} / T_0^\alpha \quad (3.1.8)$$

where the exponent α ranges from 1 to 2. Equation (3.1.8) shows that the recoil energy decreases as the

projectile energy increases. This *kinematic collision paradoxon* results from the fact that for a given impact parameter the recoil momentum depends essentially on the collision time. The latter quantity, however, decreases with increasing impact energy. Thus, the *kinematic collision paradoxon* may be understood.

3.2. Kinematic effects on the ejected electrons

Since the Auger electron originates from a moving emitter, it is influenced by kinematic effects first pointed out by Rudd et al. [44]. Hence, the corresponding Auger lines are modified in position, width and intensity. Kinematic effects on the Auger lines have been studied by Gordeev and Ogurtsov [45], Rudd and Macek [11], Risley et al. [155], Stolterfoht et al. [156], Gleizes et al. [157] and Dahl et al. [258]. To calculate these effects it is useful to introduce the reduced emitter energy $t_i = T_i/M_i = v_i^2/2$. Again, the labels $i = 1$ and 2 are used for the scattered projectile and the target atom, respectively. Note that the emitter mass M_i is given here in atomic units, i.e. of the electron mass.

The velocity \mathbf{v} of the Auger electron in the laboratory frame of reference is obtained from adding the emitter velocity \mathbf{v}_i to the velocity \mathbf{v}' of the electron in the emitter rest frame, as shown in fig. 10. Here, quantities in the emitter rest frame are denoted by primed symbols. It follows that for the projectile rest frame energy $\varepsilon' = v'^2/2$ of the electron

$$\varepsilon' = \varepsilon + t_i - 2(\varepsilon t_i)^{1/2} \cos \chi_i. \quad (3.2.1a)$$

The same equation but solved for the electron energy ε in the laboratory rest frame reads

$$\varepsilon = [t_i^{1/2} \cos \chi_i \pm (\varepsilon' - t_i \sin^2 \chi_i)^{1/2}]^2 \quad (3.2.1b)$$

with

$$\cos \chi_i = \cos \theta \cos \beta_i + \sin \theta \sin \beta_i \cos \phi$$

where χ_i denotes the angle between \mathbf{v} and \mathbf{v}_i (fig. 10). The angles θ and ϕ specify the direction of the electron with respect to the incident beam.

Equation (3.2.1b) may also be written as $v = u_i \pm u'$, where $u_i = v_i \cos \chi_i$ and $u' = v' \cos \psi_i$ are the

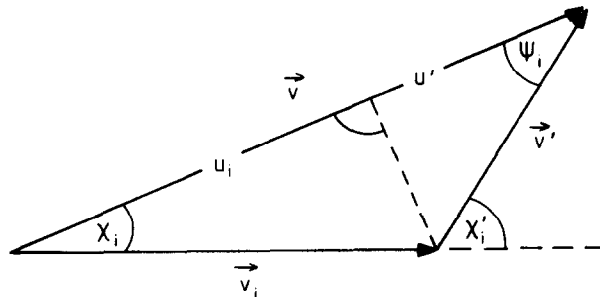


Fig. 10. Vector diagram formed by the emitter velocity \mathbf{v}_i and the velocities \mathbf{v} and \mathbf{v}' of the ejected electron in the laboratory and the emitter frame of reference, respectively.

projections of the velocities \mathbf{v}_i and \mathbf{v}' , respectively, along the direction of the velocity \mathbf{v} (fig. 10). Note that $\psi_i = \chi'_i - \chi_i$. Hence, the first and second term on the right-hand side of eq. (3.2.1b) may be regarded as contributions originating from the emitter and the electron, respectively. The fraction u'/v , a measure of the relative contribution from the electron, may be expressed as

$$\frac{u'}{v} = \left(\frac{\varepsilon'}{\varepsilon}\right)^{1/2} \cos \psi_i = \left(\frac{\varepsilon'}{\varepsilon}\right)^{1/2} \left[1 - \frac{t_i}{\varepsilon'} \sin^2 \chi_i\right]^{1/2} = 1 - \left(\frac{t_i}{\varepsilon}\right)^{1/2} \cos \chi_i \quad (3.2.2)$$

where eq. (3.2.1b) was used. This fraction is close to unity for slow emitters or for small angles χ_i . However, it may deviate from one for fast emitters ($t_i > \varepsilon'_0$). In this case, u'/v tends to zero when χ_i approximates the maximum angle χ_i^m defined by $\sin \chi_i^m = (\varepsilon'/t_i)^{1/2}$ for which \mathbf{v}' becomes perpendicular to \mathbf{v} ($\psi = 90^\circ$). It is shown below that the ratio v/u' governs the transformation of the Auger line width which plays an important role in the calculations of the kinematic effects.

In the following the kinematic effects changing the position, width and height of an Auger line, are referred to as *shifting*, *stretching* and *enhancing*, respectively. Also, the occurrence of two Auger lines in the spectrum is denoted as *doubling*. These effects originate from the transformations of the emitter frame of reference to the laboratory frame of reference. In addition, there are *broadening* effects on the Auger line which originate primarily from instrumental deficiencies.

Doubling: Slow emitters ($t_i < \varepsilon'$) yield one solution referring to the + sign in eq. (3.2.1b). Hence, one Auger line is produced in the laboratory rest frame referring to one Auger line in the emitter frame of reference. However, for fast emitters ($t_i > \varepsilon'$) two solutions exist referring to the + and - sign in eq. (3.2.1b). For example, at 0° two Auger lines are produced in the laboratory frame corresponding to the ejection of the electrons under 0° and 180° in the emitter frame of reference [60]. However, such solutions are possible only for angles smaller than the limiting angle χ_i^m . At angles larger than χ_i^m no solution exists. Hence, fast emitters eject Auger electrons only in a cone of forward angles. It is noted that in collision systems considered in this article, the designations 'fast' and 'slow' are generally applicable to the projectile and target, respectively.

Also, it is mentioned that the terms 'slow' and 'fast' used here correspond to those known from the discussion of the inner-shell excitation mechanisms. There, the projectile velocity is compared with the velocity of the bound inner-shell electron involved in the excitation. The velocities of the inner-shell electron and the Auger electron ejected by filling the corresponding inner-shell vacancy are roughly equal.

Stretching: The width $\Delta\varepsilon$ of the Auger line observed in the laboratory frame differs from the corresponding width $\Delta\varepsilon'$ observed in the emitter rest frame. From eq. (3.2.1a) it follows that $d\varepsilon'/d\varepsilon = 1 - (t_i/\varepsilon)^{1/2} \cos \chi_i$ which is seen to be equal to u'/v from eq. (3.2.2). For sufficiently small widths one may set $\Delta\varepsilon/\Delta\varepsilon' \approx d\varepsilon/d\varepsilon'$ and one obtains

$$\Delta\varepsilon = \left(\frac{\varepsilon}{\varepsilon'}\right)^{1/2} \left(1 - \frac{t_i}{\varepsilon'} \sin^2 \chi_i\right)^{-1/2} \Delta\varepsilon' \quad (3.2.3)$$

where eq. (3.2.2) was used. The effect of the width transformation results in a 'stretching' (or 'compressing') of the Auger spectrum as a whole [17, 155]. It is important to note that the stretching effect does not wash out intrinsic structures of the spectrum, i.e. it does not increase the overlap of closely lying lines. Such 'wash out', however, is produced by the broadening effects discussed further below.

Enhancing: The frame transformation enhances (or reduces) the height of an Auger line. This effect may be accounted for by relating the solid angle $\Delta\Omega'$ in the emitter rest frame to the solid angle $\Delta\Omega$ in the laboratory rest frame. From $\Delta\Omega/\Delta\Omega' = \sin \chi_i \Delta\chi_i/\sin \chi'_i \Delta\chi'_i$, $d\varepsilon'/d\chi_i = 2(t_i\varepsilon)^{1/2} \sin \chi_i$ and $d\varepsilon/d\chi' = 2(t_i\varepsilon')^{1/2} \sin \chi'_i$ it follows with eq. (2.3.2) that

$$\Delta\Omega = \frac{\varepsilon'}{\varepsilon} \left(1 - \frac{t_i}{\varepsilon'} \sin^2 \chi_i\right)^{1/2} \Delta\Omega'. \quad (3.2.4)$$

It is noted that the solid angle decreases as the energy increases by the frame transformation. The solid angle $\Delta\Omega$ acquires the same number of electrons in the laboratory frame as $\Delta\Omega'$ does in the emitter rest frame. For example, electrons from fast emitters are strongly forward directed so that there the solid angle is relatively small for the detection of a given number of electrons.

From eq. (3.2.4) the relation between the single differential cross section $d\sigma/d\Omega$ in the laboratory rest frame and the corresponding cross section $d\sigma'/d\Omega'$ is obtained as [158]

$$\frac{d\sigma}{d\Omega} = \frac{\varepsilon}{\varepsilon'} \left(1 - \frac{t_i}{\varepsilon'} \sin^2 \chi_i\right)^{-1/2} \frac{d\sigma'}{d\Omega'}. \quad (3.2.5)$$

Similarly, the double differential cross section $d^2\sigma/d\varepsilon d\Omega$ is transformed according to

$$\frac{d\sigma}{d\varepsilon d\Omega} = \left(\frac{\varepsilon}{\varepsilon'}\right)^{1/2} \frac{d\sigma'}{d\varepsilon' d\Omega'}. \quad (3.2.6)$$

where eq. (3.2.3) was implicated. Equation (3.2.6) shows that the height of an Auger line is increased as the Auger energy increases by the frame transformation. Of course, eq. (3.2.6) is not limited to Auger electrons production, but it applies for electron ejection, in general [160].

Broadenings: A broadening effect increases the width of an Auger line without increasing the separation between two neighbouring lines. Therefore, it increases the overlap of the two lines and, hence, it washes out intrinsic structures of the Auger spectra. The broadenings are due to the fact that some kinematic parameters vary within certain ranges [155, 156]:

- (i) the variation $\Delta\phi$ of the azimuthal angle between electron and emitter,
- (ii) the variation $\Delta\theta$ of the polar angle of the electron,
- (iii) the variation $\Delta\beta_i$ of the emitter scattering angle, and
- (iv) the variation Δt_i of the reduced emitter energy.

For convenience in our notation, the effects (i) and (ii) will be referred to as *azimuthal broadening* and *polar broadening*, respectively. It is noted that the effects (i) and (iv) are important for electrons from both target and projectile and that (ii) and (iii) primarily affect the projectile electrons. In first or higher order the broadening may be deduced from the corresponding term of a Taylor expansion. Furthermore, the broadening may be calculated in all orders as the difference $\Delta\varepsilon$ of the energies evaluated from eq. (3.2.1b) between the two limits within which the relevant parameter varies.

In noncoincidence experiments, where the scattering plane is not fixed, the azimuthal broadening effect is most significant, since ϕ may vary in the full angular range. The shape of the Auger line resulting from the variation of ϕ is given by the distribution function

$$f_\phi(\varepsilon) = \frac{d\sigma}{d\Omega'} \frac{d\phi}{d\varepsilon} \quad (3.2.7)$$

where $d\sigma/d\Omega'$ is the single differential cross section for Auger emission in the emitter rest frame. The derivative $d\phi/d\varepsilon$ may be evaluated (without approximation) by means of eq. (3.2.1b). One obtains

$$\frac{d\phi}{d\varepsilon} = \frac{(\varepsilon + \varepsilon' - t_i)/2\varepsilon}{[B^2 - (\varepsilon - \varepsilon' + t_i - A)^2]^{1/2}} \tag{3.2.8}$$

where

$$A = 2(\varepsilon t_i)^{1/2} \cos \beta_i \cos \theta$$

and

$$B = 2(\varepsilon t_i)^{1/2} \sin \beta_i \sin \theta$$

introduced by Gordeev and Ogurtsov [45]. For constant $d\sigma/d\Omega'$, the shape of the Auger line is solely given by eq. (3.2.8) which yields the characteristic Auger profile discussed in detail previously [11, 45, 157]. Figure 11 shows such profile schematically. Outstanding features of the profile are the singularities at energies ε_1 and ε_2 for which the dominator vanishes in eq. (3.2.8). In practice, these singularities are smeared out by additional broadening effects such as the variation Δt_2 of the recoil energy treated further below.

The electron intensity distribution is centered around the mean value $\bar{\varepsilon}$ obtained by solving the equation

$$\varepsilon' = \bar{\varepsilon} + t_i - 2(\bar{\varepsilon} t_i)^{1/2} \cos \beta_i \cos \theta .$$

Comparison with eq. (3.2.1a) shows that $\bar{\varepsilon}$ represents the shifted Auger energy averaged over ϕ . Often in the analysis of the Doppler shift, the mean energy $\bar{\varepsilon}$ is meant when the label ε is used.

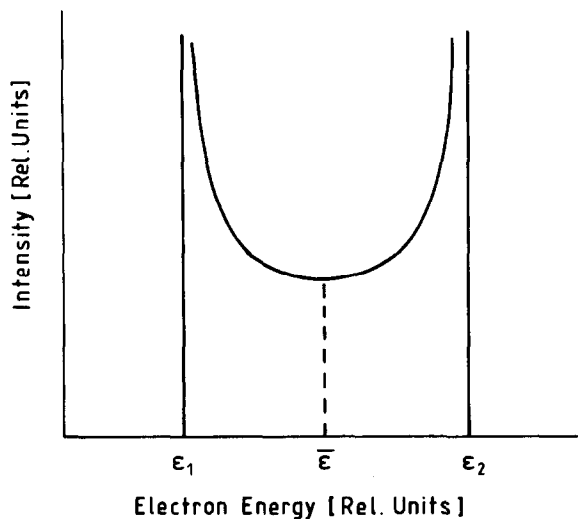


Fig. 11. Profile of an Auger line produced by the variation of the azimuthal angle ϕ . The data are evaluated by means of eq. (3.2.8).

The quantities A and B may be expressed by Taylor expansions in terms of the mean energy $\bar{\varepsilon}$:

$$A(\bar{\varepsilon} + \Delta\varepsilon) = \bar{A} + \Delta\varepsilon \bar{A}' \dots$$

$$B(\bar{\varepsilon} + \Delta\varepsilon) = \bar{B} + \Delta\varepsilon \bar{B}' \dots$$

where $\bar{A} = A(\bar{\varepsilon})$, $\bar{A}' = A'(\bar{\varepsilon})$, etc. When A and B are replaced by the zero order expression \bar{A} and \bar{B} , respectively, one obtains with $(\varepsilon + \varepsilon' - t_i)/2\varepsilon \approx 1$

$$d\phi/d\varepsilon = 1/[\bar{B}^2 - (\varepsilon - \bar{\varepsilon})^2]^{1/2}. \quad (3.2.8a)$$

Inspection of the denominator in eq. (3.1.7) shows that the Doppler profile has a (base) width of $2\bar{B}$ in accordance with the treatment by Rudd and Macek [11]. Thus, $2B$ may be considered as the zero-order approximation of the azimuthal broadening.

A more accurate expression for the (base) width of the Auger profile is obtained when the first-order terms are retained in the expansion of A and B . From the difference $\varepsilon_2 - \varepsilon_1$ of the two energies obtained by solving $\varepsilon = \varepsilon' - t_i - A(\varepsilon) \pm B(\varepsilon)$ for which the denominator vanishes in eq. (3.2.8), it follows that $\Delta B_\phi = 2\bar{B}/[1 - \bar{A}']$ for the azimuthal broadening. Hence, one obtains

$$\Delta B_\phi = \frac{4(\varepsilon t_i)^{1/2} \sin \beta_i \sin \theta}{1 - (t_i/\varepsilon)^{1/2} \cos \beta_i \cos \theta} \quad (3.2.9)$$

where $\bar{\varepsilon}$ is denoted by ε as usually done when no chance for confusion exists. The expression derived by Rudd and Macek [11] differs from that in eq. (3.2.9) by the denominator which is equal to the width transformation factor $d\varepsilon'/d\varepsilon$, see eqs. (3.2.2) and (3.2.3). Note that eq. (3.2.9) follows also from $\Delta B_\phi = \Delta B'_\phi d\varepsilon'/d\varepsilon'$ where the broadening $\Delta B'_\phi = \varepsilon'(\phi = 0^\circ) - \varepsilon'(\phi = 180^\circ)$ is equal to $2\bar{B}$, see eq. (3.2.1a). Hence, the broadening given by Rudd and Macek [11] is equal to B'_ϕ which refers to the emitter rest frame. For slow emitters the frame transformation may be disregarded, since $d\varepsilon'/d\varepsilon'$ is close to unity. However, for fast emitters the frame transformation becomes significant. Thus, eq. (3.2.9) may be considered as an extension to fast emitters for which the Doppler shift is important.

It is interesting to note that in near symmetric collisions the broadenings from eq. (3.2.9) are practically equal for the projectile and the target atom. This follows from the fact that ΔB_ϕ depends on the velocity component $t_i^{1/2}$ perpendicular to the incident beam, whose values are nearly equal for the projectile ($i = 1$) and the target atom ($i = 2$), see eq. (3.1.3).

The azimuthal broadening may significantly be reduced when the electrons are observed at 0° or 180° [161]. This possibility, however, has not as yet been exploited in the field of target Auger spectroscopy. To reduce the azimuthal broadening, other methods are frequently used.

For fast collisions relevant here, one may set $\beta_2 \approx 90^\circ$ and, thus $t_i^{1/2} \sin \beta_i \approx t_2^{1/2}$. Hence, approximately, the broadening ΔB_ϕ is proportional to the recoil velocity v_2 . According to the *kinematic collision paradoxon* expressed by eq. (3.1.8) the recoil velocity decreases with increasing projectile velocity. Thus, one obtains the important result that the broadening ΔB_ϕ decreases with increasing projectile velocity. Therefore, high resolution Auger studies are particularly attractive at high-energy accelerators [15, 16].

When the incident velocity increases, the projectile electrons are increasingly influenced by the polar broadening effect originating from the variation of the angle θ . This variation is usually due to the

nonzero width of the electron detector entrance slit. Using the full width $\Delta\theta$ for the spectrometer acceptance angle, it follows for the first-order term that $\Delta B_{\phi}^{(1)} = \Delta\theta d\varepsilon/d\theta$. The derivative $d\varepsilon/d\theta$ may be deduced from the relation

$$\frac{d\varepsilon}{d\theta} = \frac{d\varepsilon}{d\varepsilon'} \frac{d\varepsilon'}{d\theta} \quad (3.2.10)$$

where $d\varepsilon'/d\theta$ may be determined using eq. (3.2.1a). For small scattering angles one obtains

$$\Delta B_{\theta}^{(1)} = \Delta\theta \frac{d\varepsilon}{d\varepsilon'} 2(\varepsilon t_1)^{1/2} \cos \beta_1 \sin \theta \quad (3.2.11)$$

where $d\varepsilon/d\varepsilon' = v/u'$ from eqs. (3.2.2) and (3.2.3). For the derivation of eq. (3.2.11) it is assumed that $\beta_1 \ll \Delta\theta$ so that one may set $\sin \beta_1 \approx 0$. Deviations from this assumption will be considered further below.

The expression (3.2.11) has previously been given by Risley et al. [155]. The broadening formula given by Stolterfoht et al. [156] differs from that in eq. (3.2.11) by the factor $d\varepsilon/d\varepsilon'$ which provides the width transformation from the emitter to laboratory rest frame, see eq. (3.2.3). As mentioned above, the frame transformation may be disregarded for slow collisions [156].

It should be kept in mind that the application of eq. (3.2.11) is limited to projectile electrons. The formula shows that the broadening $\Delta B_{\theta}^{(1)}$ depends on the emitter velocity component parallel to the incident beam. This component is usually much larger for the projectile than that for the target atom. Thus it is understood that the broadening $\Delta B_{\theta}^{(1)}$ is significant primarily for the projectile. For the projectile it is clear that the broadening $\Delta B_{\theta}^{(1)}$ increases with increasing impact velocity. This is the major reason that high-resolution studies of projectile Auger electrons are difficult to perform at high-energy accelerators.

The polar broadening effect may essentially be reduced when the electrons are observed at zero degree [60]. There the first-order expression (3.2.11) cancels and the second-order term $\Delta B_{\theta}^{(2)} = 0.5 \Delta\theta^2 d\varepsilon^2/d\theta^2$ becomes important. Forming the two-fold θ derivative of ε from eq. (3.2.1b) yields for $\theta = 0$

$$\Delta B_{\theta}^{(2)} = \Delta\theta^2 \frac{t_1}{4} \left[\left(\frac{\varepsilon'}{t_1} \right)^{1/2} + \left(\frac{t_1}{\varepsilon'} \right)^{1/2} \pm 2 \right] \quad (3.2.12)$$

where the signs + and – correspond to the two solutions of eq. (3.2.1b). Again, it is assumed that β_1 is much smaller than $\Delta\theta$. Expression (3.2.12) has previously been given by Itoh et al. [61]. It is noted that Itoh et al. [61] used the half angle of the analyzer acceptance whereas, here, $\Delta\theta$ refers to the full width of the analyzer acceptance angle.

A rough estimate for $10^\circ \leq \theta \leq 170^\circ$ shows that $\Delta B_{\theta}^{(2)}/\Delta B_{\theta}^{(1)} \approx \Delta\theta$. With typical acceptance angles of 0.5° or 10^{-2} rad it is seen that $B_{\theta}^{(2)}$ is two orders of magnitude smaller than $B_{\theta}^{(1)}$. Hence, a significant reduction of the broadening effect is expected when the first-order term cancels. Indeed, experimental studies at electron observation angle of zero degree have shown that projectile Auger spectra may be recorded with relatively high resolution [61].

The broadening effect due to the variation $\Delta\beta_1$ of the projectile scattering angle is treated similarly as the polar broadening effect. In first order, one obtains $\Delta B_{\theta}^{(1)} = \Delta\beta_1 d\varepsilon/d\beta_1$. Again, the broadening effect is first analyzed in the emitter frame of ref. [146] and then transformed to the laboratory frame.

With a fixed azimuthal angle ($\phi = 0$) it follows from eqs. (3.2.1a) and (3.2.1b) that $d\varepsilon'/d\beta_1 = 2(\varepsilon t_1)^{1/2} \cos \bar{\beta}_1 \sin \theta$, where the mean scattering angle $\bar{\beta}_1$ is assumed to be small ($\sin \bar{\beta}_1 \approx 0$). Thus, it follows that

$$\Delta B_\beta^{(1)} = \Delta \beta_1 \frac{d\varepsilon}{d\varepsilon'} 2(\varepsilon t_1)^{1/2} \cos \bar{\beta}_1 \sin \theta. \quad (3.2.13)$$

It is seen that eq. (3.2.13) is identical to eq. (3.2.11) except that $\Delta\theta$ is replaced by $\Delta\beta_1$. Consequently, the broadenings ΔB_θ and ΔB_β may be treated together using the sum $\Delta\theta + \Delta\beta_1$ instead of $\Delta\theta$ in eq. (3.2.11). Similarly, the combined second-order effect may be evaluated by inserting the sum $\Delta\theta^2 + \Delta\beta_1^2$ for $\Delta\theta^2$ in eq. (3.2.12) where cross terms are disregarded in the Taylor expansion.

The broadening ΔB_i due to the variation Δt_i of the reduced energy of the emitter is obtained from $\Delta B_i^{(1)} = \Delta t_i d\varepsilon/dt_i$. As usual, $d\varepsilon'/dt_i$ is determined first and, then, a width transformation is performed. One obtains

$$\Delta B_i^{(1)} = \frac{\Delta t_i}{t_i} (\varepsilon' - \varepsilon) \frac{d\varepsilon}{d\varepsilon'}. \quad (3.2.14)$$

The broadening $\Delta B_i^{(1)}$ is relevant for projectile electrons as well as for target electrons. For projectile emitters the relative variation $\Delta t_1/t_1$ is usually small but the Doppler shift $\varepsilon' - \varepsilon$ may be significant. For target emitters the Doppler shift $\varepsilon' - \varepsilon$ is usually small but the relative variation $\Delta t_2/t_2$ is rather large, since t_2 is strongly affected by a small variation of the projectile scattering angle β_1 , see eq. (3.1.4). Hence, the variation $\Delta\beta_1$ produces broadening effects for the projectile electrons eq. (3.2.13) as well as for the target electrons via the variation of the recoil energy (eq. (3.2.14)).

4. Target Auger spectroscopy

4.1. General considerations

The important feature of target Auger spectroscopy is its potential to gain information about multiple ionization processes in a single collision [47]. In fact, the target atom may be stripped to a few-electron system, when sufficiently heavy projectiles are used [49]. Fast projectiles transfer only little energy to the target atom so that the kinematic effects on the ejected Auger electrons are limited. Hence, target Auger spectroscopy provides detailed information about the production and decay of states in highly ionized systems.

The few-electron recoil ions may be used to study secondary collisions with neutral target atoms [51]. Information about this type of collision is of fundamental importance in many adjacent fields such as astrophysics, plasma physics, and fusion research. The knowledge of such collisions is limited, since slow and highly ionized atomic species are difficult to achieve under laboratory conditions. Therefore, the investigation of secondary collisions involving slow recoil ions are of considerable interest. The related studies of Auger electrons are referred to as *recoil Auger spectroscopy*.

Target Auger spectroscopy is strongly affected by problems arising from the large number of inner-shell vacancy states randomly created in heavy ion-atom collisions. Usually, the target Auger spectra induced by energetic heavy-ion impact exhibits numerous overlapping lines. Unfortunately, the

complexity of the electron spectra is a principle problem in the field of Auger spectroscopy. Often the analysis of the complex target Auger spectra is possible only by means of statistical methods.

When the target atom is stripped to a few-electron system by impact of very heavy projectiles, simpler Auger spectra are produced. Fortunately, in this case the analysis of individual lines becomes possible. Thus, in the field of target Auger spectroscopy particular interest has been devoted to few-electron systems. Most such studies have been conducted using rare gas target atoms. This has been done to avoid further complications created when molecular targets are used.

The recoil momentum transferred in fast collisions is sufficiently small so that kinematic (Doppler) shifting effects are negligible, in general. However, kinematic broadening effects may play a significant role in target Auger spectroscopy. The Auger electrons from the target atom are influenced by the azimuthal broadening effect produced by the random direction of the recoil momentum.

The azimuthal broadening is relatively large for heavy particles incident at relatively low velocities. This has first been noted in $\text{Ne}^+ + \text{Ne}$ and $\text{Ar}^+ + \text{Ar}$ collisions studied by Cacak et al. [46] and Volz and Rudd [162] using projectiles of energies as low as 50 keV. Stolterfoht et al. [156] made the attempt to measure the Auger electron from the $\text{Ne}^+ + \text{Ne}$ system with high resolution. The result is shown in fig. 12. It is seen that the spectral structures are completely smeared out in the Auger spectrum. For 500-keV Ne^+ impact the azimuthal line broadening is estimated from eq. (3.2.9) to be ~ 20 eV which is much larger than the typical line separation of a few eV [156]. Therefore, the spectrum appears as a broad maximum although the instrumental resolution (2.6 eV) would be sufficient to resolve individual lines. In this case, it is impossible to perform high-resolution studies of the Auger electrons.

Broadening effects have been studied for light-ion impact by Matthews et al. [163]. For light projectiles the recoil effects are negligible, in general. However, azimuthal broadening becomes noticeable in the Ne-K Auger spectrum for proton energies as low as 150 keV.

There are different methods to avoid the broadening effects in the field of target spectroscopy. For instance, to reduce the broadening ΔE_ϕ , the range of the azimuthal angle ϕ could be limited by performing electron-ion coincidence measurements. However, the limitation of the counting rate

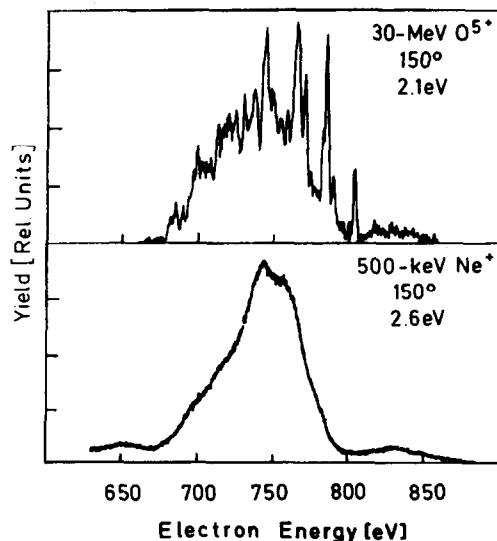


Fig. 12. Spectra of K-Auger electrons from the target atom Ne excited by 30-MeV O^{5+} [164] and 500-keV Ne^+ [156]. Observation angle is 150° and energy resolution (FWHM) is 2.1 eV and 2.6 eV as indicated.

imposes serious problems in the application of coincidence techniques in high-resolution studies of Auger electrons.

To reduce the azimuthal broadening effect, one generally tries to minimize the quantity $t_2^{1/2} \sin \theta$, see eq. (3.2.9). This can be done by measuring the electrons at extreme forward or backward angles [161]. However, the number of 0° or 180° measurement of the electrons is still rather limited in the field of target Auger spectroscopy. It appears promising to apply this method further in the future.

To date, the most important method to avoid the azimuthal broadening is to use projectiles of high energies. Due to the collision paradoxon (section 3.2), the recoil energy decreases as the projectile energy increases. Matthews et al. [47, 163] were first to apply the method of using high-energy projectiles as discussed in more detail further below. Similar results have been obtained by Burch et al. [164] using O^{5+} projectiles of energies as high as 30 MeV. The data are also given in fig. 12. The spectrum shows a rich line structure whose analysis allows to study in detail inner-shell vacancy states.

Figure 12 clearly demonstrates that several outer-shell electrons are removed in addition to the ionization of the inner shell. The multiple ionization gives rise to various satellite lines in the corresponding Auger spectra. Hence, information about the degree of outer-shell ionization may be obtained from the analysis of the satellite lines. In the following sections the satellite structures are studied in Auger spectra produced by light and heavy ions.

4.2. *K-Auger transitions*

The example chosen for K-Auger spectra refer primarily to neon as target atom. In the field of target Auger spectroscopy, neon has been used extensively so that most effects concerning multiple ionization may be demonstrated by means of this target atom.

Outer-shell ionization by light particles incident at high velocities results predominantly from electron shake-off [165]. According to the concept or the sudden approximation which is appropriate for fast collisions, the outer-shell orbitals are considered as being frozen during the collisions. After the collision partners have separated, the outer orbitals adjust to the increased Coulomb field due to the reduced screening resulting from the inner-shell vacancy. From this picture it is plausible that the degree of outer-shell ionization is not dependent of the excitation mode of the inner shell. In particular, the relative satellite intensity is independent of the projectile provided that it is sufficiently fast. This is shown in fig. 13 where Ne-K Auger-spectra are compared for photon, electron and proton impact measured by Krause et al. [166] and Stolterfoht et al. [63]. The spectra are nearly identical indicating that the sudden approximation is rather good for the particles used. Similar results have been obtained for the K-Auger spectra of Ar by Schneider et al. [167].

The observation that protons produce the same Auger spectra as electrons and photons cannot be generalized. When protons are incident at lower energies, the satellite intensity increases significantly. This has first been shown by Edwards and Rudd [168] using protons of 300 keV. In this case, the projectile affects significantly the outer shell in addition to the ionization of the inner shell. Thus, the satellite intensity is enhanced with respect to that expected from the shake-off process.

The enhancement of the satellite intensity in K-Auger spectra produced by proton impact has been observed in several studies [163, 168–170]. The results by Schneider et al. [169] are shown in fig. 14. It is seen that for protons of 100 keV the relative satellite intensity reaches values as large as 80%. The analysis of the energy dependence of the satellite intensity has shown that capture of outer-shell electrons plays an important role at low projectile energies [169, 170].

Vacancy production in the outer shell in addition to inner-shell ionization increases strongly when

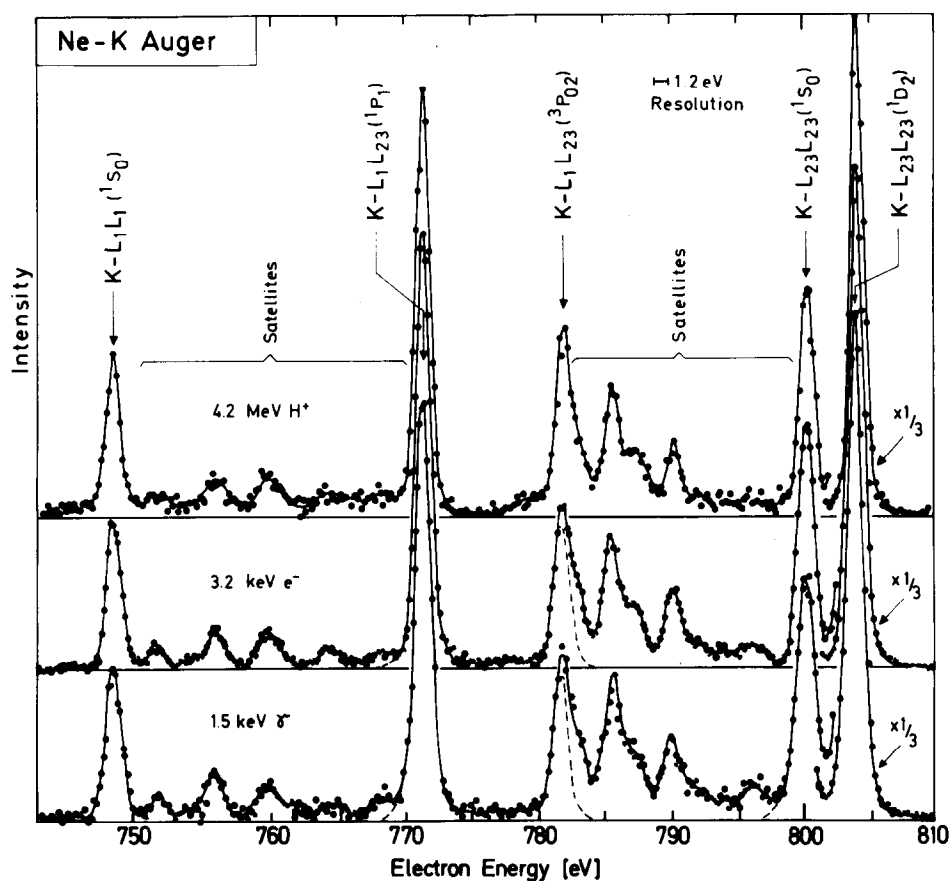


Fig. 13. Neon-K-Auger spectra produced by 4.2-MeV H^+ [63], 3.2-keV e^- [166], and 1.5-keV X-rays [166]. Note the similarity of the spectra. From ref. [63].

heavy particles are used as projectiles. Thus, heavy ion-induced Auger spectra differ significantly from those produced by light ions. This has been demonstrated by Matthews et al. [47, 163] who studied Ne-K-Auger electrons by means of 33-MeV O^{5+} impact. The Auger spectra plotted in fig. 15 exhibit individual line structure indicating the difference between heavy-ion impact and electron impact with regard to multiple ionization. For instance, it is seen that in the 33-MeV O^{5+} spectrum the diagram lines labeled D are only weakly excited.

Matthews et al. [47, 171] made the attempt to identify the line structure by means of calculated transition energies obtained from the HF-code by Froese-Fischer [97]. Similar calculations have been made by Bhalla et al. [172] and Kauffman et al. [173]. The results by Matthews et al. [47, 171] are shown in fig. 15. The calculated energies are ordered in rows each of which is attributed to a certain number of L-shell vacancies prior to the Auger transition. The theoretical data indicate that the 33-MeV $O^{5+} + Ne$ spectrum is composed of a large number of individual lines whose overlap complicates their spectral analysis.

Simpler Auger spectra are obtained when relatively heavy projectiles are used. The effect of heavier projectiles may be seen from fig. 16 where various Ne-K-Auger spectra are compared [49, 63, 164, 174]. The calculated transition energies indicate that the mean energy of the satellite lines decreases as the

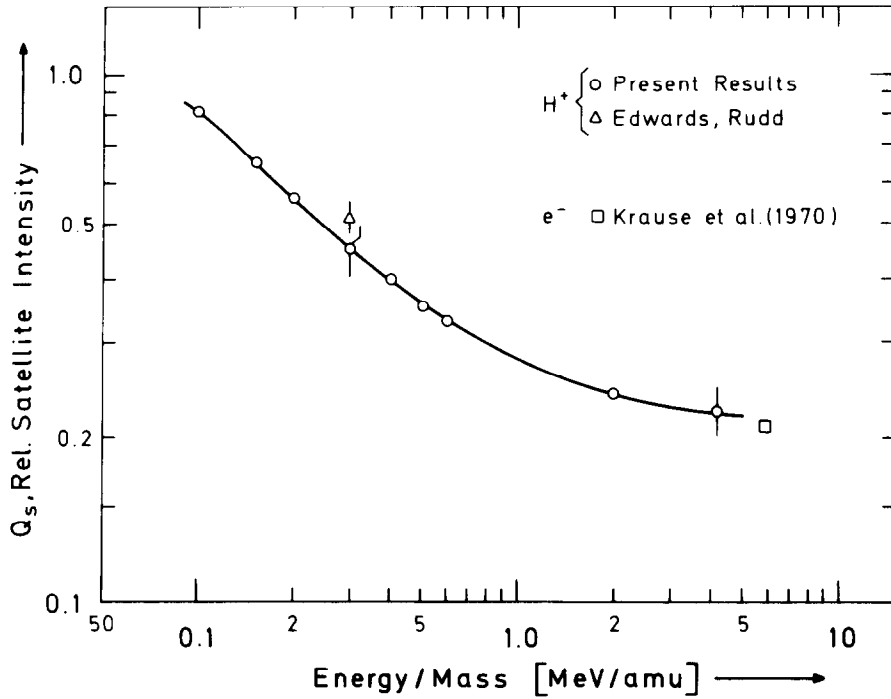


Fig. 14. Relative intensity of all satellite lines in the Ne-K-Auger spectrum excited by H^+ and e^- impact. The H^+ data are from Edwards and Rudd [168] and Schneider et al. [169]. The e^- data are from Krause et al. [166].

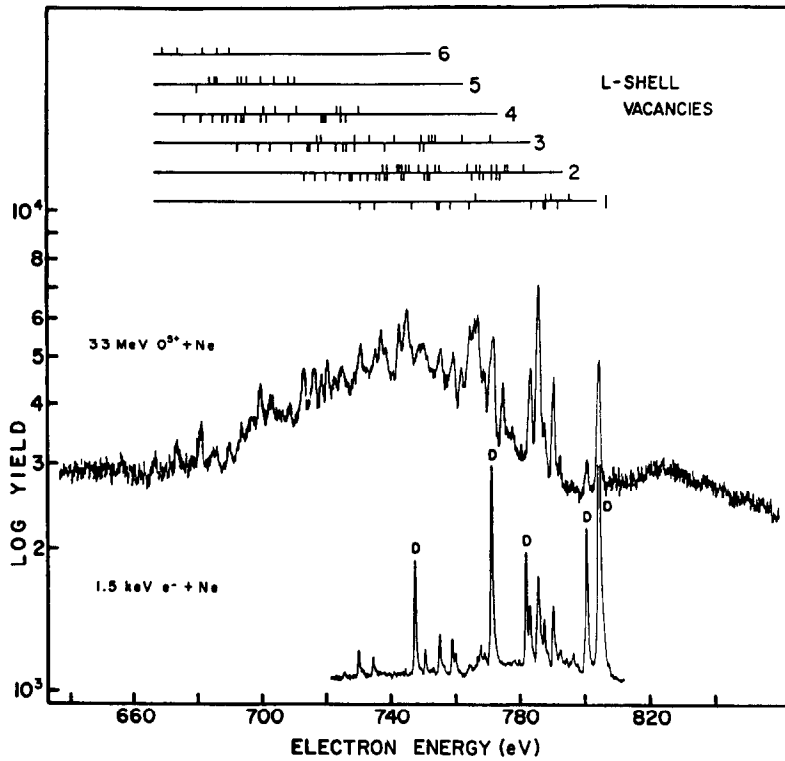


Fig. 15. Comparison of Ne-K-Auger spectra produced by 33-MeV O^{5+} and 1.5-keV e^- impact. Diagram lines are labelled D. Calculated transition energies are shown in rows labelled by the number of L-vacancies. From Matthews et al. [47].

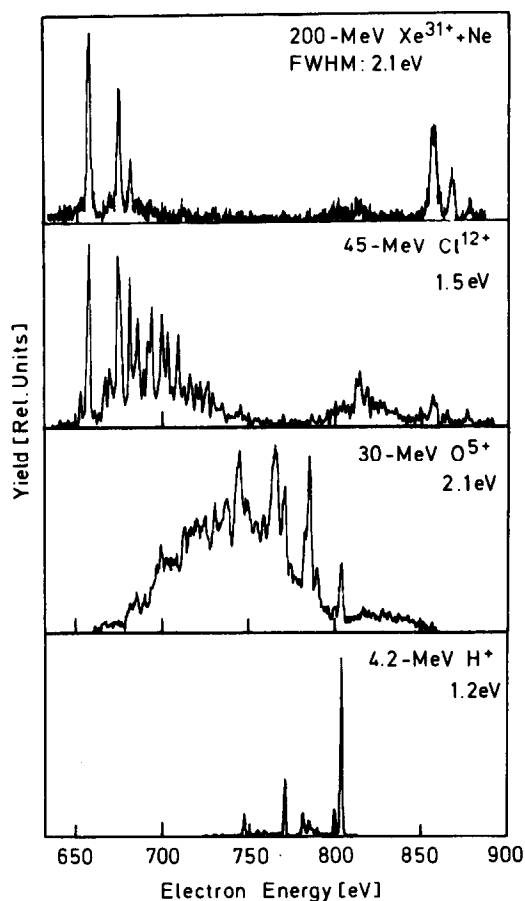


Fig. 16. Comparison of Ne-K-Auger electron spectra produced by 4.2-MeV H^+ [63], 30-MeV O^{5+} [164], 45-MeV Cl^{12+} [174] and 200-MeV Xe^{31+} [49]. Energy resolution [FWHM] is indicated. From Stolterfoht et al. [49].

number of L-shell vacancies increases. This phenomenon occurs because the sum of the binding energies of the initial electrons increases faster with increasing vacancy number than does the binding energy of the final state electron [175]. Hence, the centroid energy of the Auger spectrum is shifted to lower energies when the degree of multiple ionization increases. Therefore, from the spectra in fig. 16 it is concluded that the degree of outer-shell vacancy production increases strongly with increasing nuclear charge of the projectile.

Accordingly, multiple ionization is particularly large for the $Xe^{31+} + Ne$ system whose spectrum shows exclusively lines due to 3-electron states [49]. This indicates that heavy projectiles may strip almost all electrons from the L-shell in a single collision. It is seen that only a few lines remain in the Auger spectrum. Actually, the $Xe^{31+} + Ne$ spectrum is as simple as that for H^+ impact. This similarity is understood from the fact that H^+ produces a few-hole system, whereas Xe^{31+} produces a few-electron system.

Since the three-electron system plays an important role in the field of target Auger spectroscopy, it is instructive to study Li itself. Ziem et al. [176] bombarded Li atoms in the vapour phase by protons and helium. Figure 17 compares results for 100-keV H^+ and 200-keV He^+ impact. The energy scale is calibrated by means of the $1s(2s2p^{1,3}P)^2P$ states whose energies have been measured with high accuracy

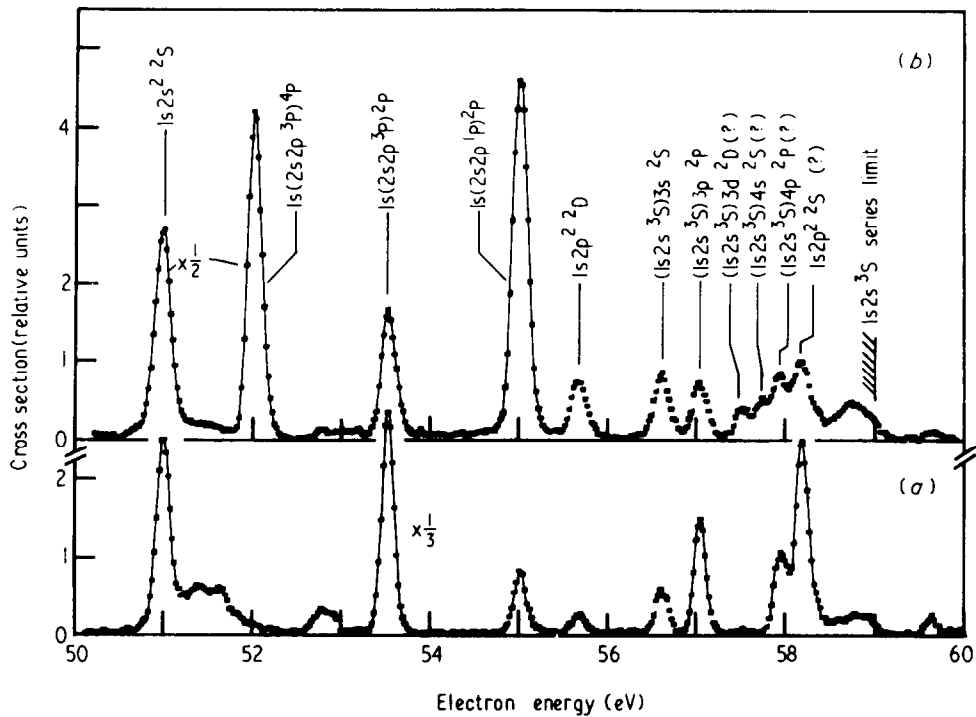


Fig. 17. Lithium-K-Auger spectra produced by 100-keV H^+ (a) and 200-keV He^+ (b). From Ziem et al. [176].

by Ederer et al. [177] using the method of photoabsorption; see also Berry et al. [178]. It is interesting to note that H^+ impact does not produce quartet states since their excitation would require (unlike) spin-flip events. However, He^+ does excite the $1s2s2p^4P$ state by electron exchange processes. It is noted that the He^+ spectrum is qualitatively equal to that produced by 200-MeV Xe^{31+} on Ne.

With regard to the ability of fast heavy ions to strip the target atom to a Li-like configuration, it is interesting to consider heavier systems. To date, the heaviest target atom that has been studied as a few-electron system in the field of target Auger spectroscopy is Ar. Mann et al. [20] bombarded 6-MeV/u U^{39+} and U^{66+} on Ar to investigate multiple ionization of the target atom. The results are shown in fig. 18. It is seen that the projectile charge state of 39 is not sufficient to strip Ar down to a three-electron system. This is not only due to the enlarged number of target electrons, but also due to the fact that the L- and M-shell require different velocities to achieve optimum ionization [20].

However, few-electron configurations for Ar are produced when the projectile charge state is increased to 66. In fig. 18 the inset shows the most prominent lines due to Li-like states. Mann et al. [20] noted that the width of the metastable states $1s2s2p^4P^o$ and $2s2p^2^4P^e$ are significantly broader than expected from the instrumental resolution. This indicates that an appreciable amount of recoil energy is transferred to the target atom. The analysis of the azimuthal broadening effect shows that the recoil energy of ~ 60 eV is transferred in the collision system 6-MeV/u $U^{66+} + Ar$ [20].

The study of the target atom Ar shows that the method to produce few-electron systems in single collisions is limited. Since 6-MeV/u U^{66+} may be considered as one of the most efficient projectiles with respect to target ionization, it is unlikely that target atoms heavier than Ar may essentially be stripped. Hence, the atomic number of ~ 20 appears as an upper limit for the method to produce few-electron systems in single collisions.

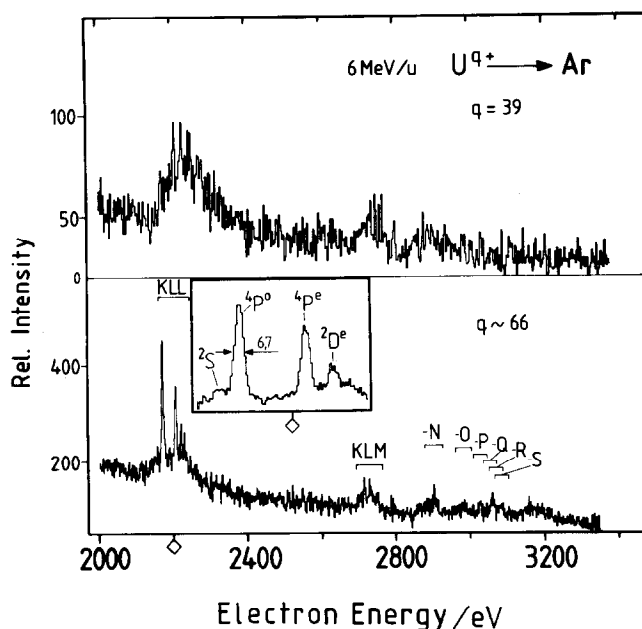


Fig. 18. Argon-K-Auger spectra produced by 6 MeV/u U^{39+} and U^{66+} impact. The inset gives an expanded part of the lower spectrum showing some Li-like lines. From Mann et al. [20].

The U impact data clearly show that the multiple L-shell ionization is dependent on the projectile charge. Hence, questions arise about the role of the projectile charge state in the process of outer-shell vacancy production. First studies concerning the incident charge state have been made by Moore et al. [179] who measured Ne-K-Auger spectra using 35-MeV O^{6+} and O^{8+} impact. The results are given in fig. 19 indicating a significant increase of the multiple L-shell ionization with increasing charge state. For instance, the O^{8+} projectile produces the Li-like Auger lines which are so important for heavier projectiles (fig. 16).

The increase of the degree of multiple ionization with increasing charge state has been observed in various studies [20, 50–53]. It is difficult, however, to analyze the projectile charge state dependence on a quantitative basis. Various attempts have been made to introduce an effective charge for the projectile by estimating the screening effect of the projectile electrons [50, 53, 180]. These attempts will be discussed in more detail in the following section.

Multiple ionization effects have also been inspected with respect to a variation of the projectile energy. Comparison of the spectra produced by 500-keV Ne^+ and 30-MeV O^{5+} (fig. 12) suggests that the L-shell ionization is rather independent of the projectile energy. However, this finding cannot be generalized. Schneider et al. [50] showed for Ne projectiles with energies as high as 290 MeV that the degree of outer-shell ionization decreases with increasing projectile velocity. This observation is plausible, since the optimum outer-shell ionization is expected for projectiles whose velocity matches the velocity of the outer-shell electron. However, Ne projectiles of several hundred MeV are faster by about one order of magnitude than the L-shell electron of the Ne-target.

The dependence of the outer-shell ionization on the projectile energy is demonstrated in fig. 20. The data were measured by Mann et al. [20] for the Kr + Ne system. It is noted that the velocity of the Ne-K-shell electron and that of the projectile match at about 2 MeV/u. It is seen that the degree of

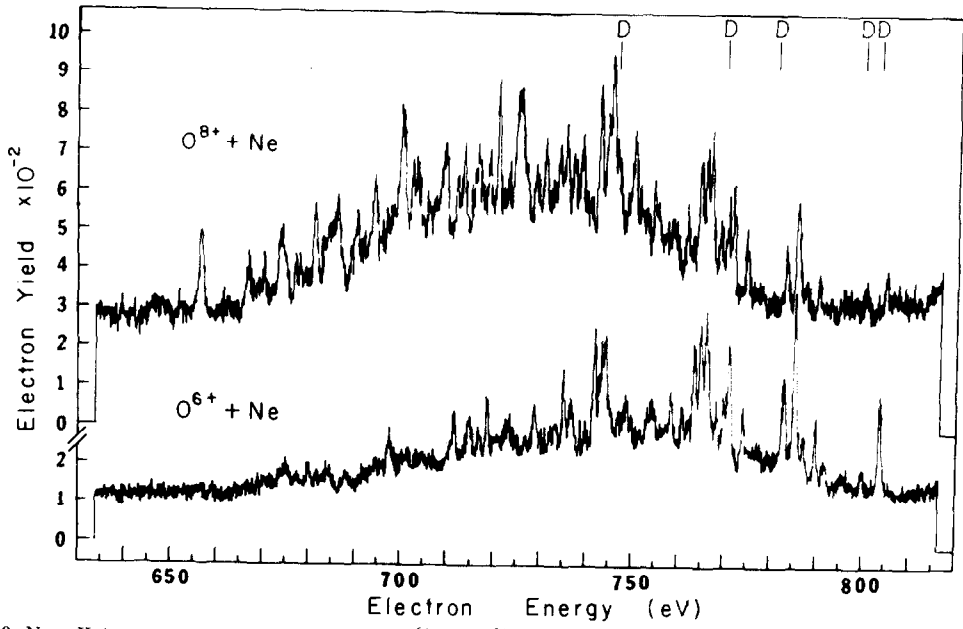


Fig. 19. Neon-K-Auger spectra produced in 35-MeV O^{6+} and O^{8+} impact. Diagram lines are labelled D. From Moore et al. [179].

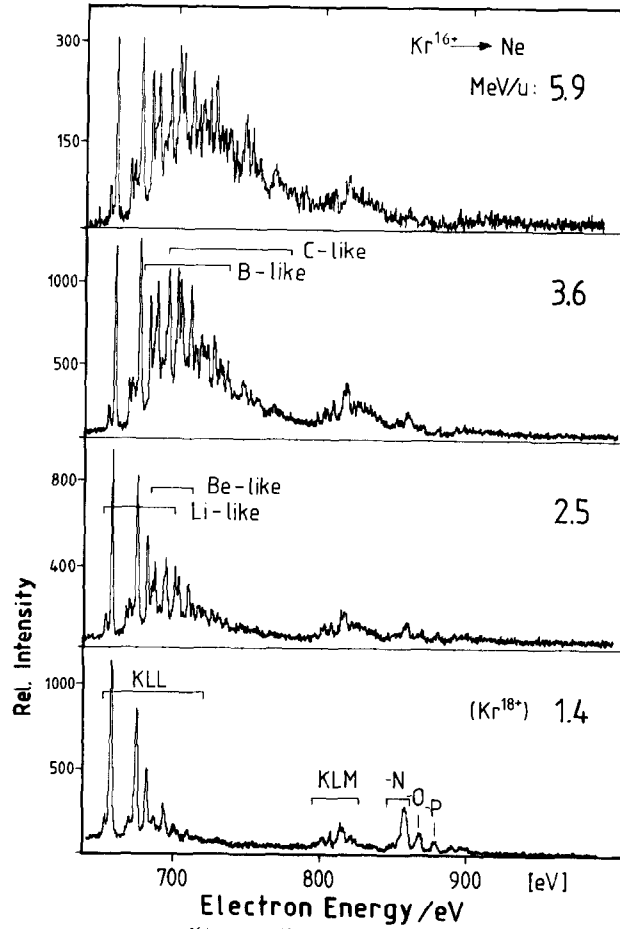


Fig. 20. Neon-K-Auger spectra produced by Kr^{16+} and Kr^{18+} of energies ranging from 1.4 to 5.9 MeV/u. From Mann et al. [20].

multiple ionization decreases significantly as the projectile energy increases from 1.4 MeV/u to 5.9 MeV/u. Hence, to a certain extent it is possible to 'scan' the charge state of the target atom by varying the projectile energy.

Finally, the production of hypersatellites in the Ne-K-Auger spectra shall be discussed. Strong population of double K-vacancy states have been observed, when completely stripped projectiles are used. In fig. 21 results are shown for 25-MeV F^{7+} , F^{8+} and F^{9+} on Ne measured by Woods et al. [52]. For F^{7+} and F^{8+} impact the shape of the spectra is similar to those observed for O^{5+} impact (fig. 16). Most of the intensity is found in one peak near 720 eV. At ~ 830 eV a second peak is seen probably due to the excitation of higher-lying Rydberg states. However, in the F^{9+} spectrum the valley of the two peaks is filled and at ~ 915 eV another peak is visible. Calculated transition energies [52] also given in

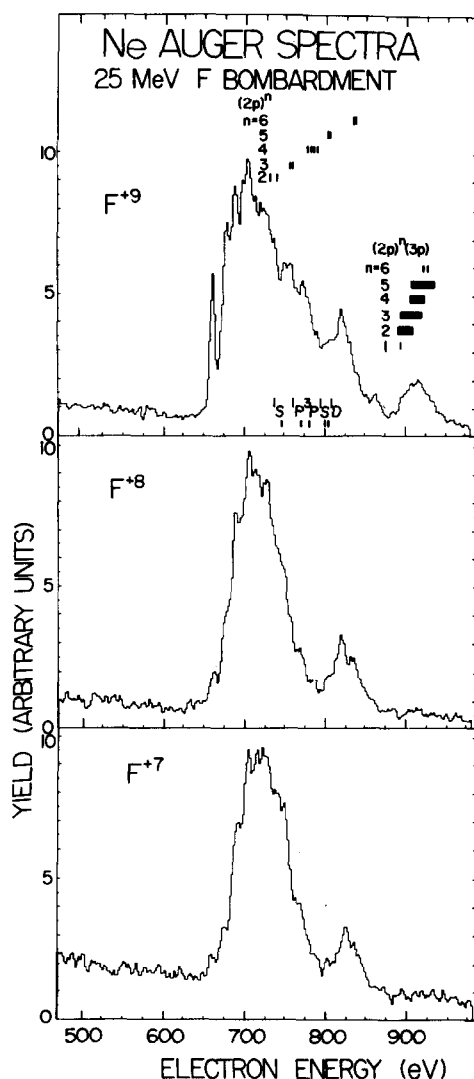


Fig. 21. Neon-K-Auger spectra produced by 25-MeV F^{7+} , F^{8+} and F^{9+} . Calculated transition energies for the initial configurations $(2p)^n$ and $(2p)^n 3p$ are shown. From Woods et al. [52].

fig. 21 show that the intensity near 750 eV is due to hypersatellite lines from the initial configuration $2p^n$ whereas the peak near 915 eV is due to the configuration $2p^n 3p$.

The reason for the fact that F^{9+} does and F^{7+} (or F^{8+}) does not produce hypersatellites is that a significant fraction of K-vacancy production by highly stripped ions occurs via electron capture into the K-shell of the projectile. For F^{9+} two electrons may be captured whereas for F^{8+} the transfer of only one electron is possible. Woods et al. [52] found the variation of the hypersatellite intensity with varying projectile energy is consistent with the related Brinkmann–Kramer calculation for electron capture. This finding demonstrates that electron capture is a mechanism contributing to K-shell vacancy production in ion–atom collisions.

4.3. L- and M-Auger transitions

Auger spectra resulting from L-shell excitation have extensively been studied using the target atom Ar. The specific feature of the L-Auger spectrum is that the L_2 – L_3 fine structure-splitting is visible so that the number of lines is essentially doubled. Thus, the L-Auger spectra are more complex than the corresponding K-Auger data. With ion impact, first high resolution measurements of the Ar-L-Auger spectrum have been performed by Volz and Rudd [162]. In the experiments, H^+ projectiles were used within the energy range of 50 to 300 keV. Volz and Rudd [162] have studied primarily the branching ratios for formal transitions from initial L_2 and L_3 vacancy states.

Figure 22 shows an example for the Ar-L-Auger spectrum produced by 400-keV H^+ impact [181]. The spectrum shows 12 diagram lines, half of them are attributed to initial L_2 vacancies and the other are due to L_3 vacancies. Although the resolution of 0.35 eV is rather high, it is often not sufficient to avoid the overlap of closely-lying lines. Ridder et al. [182] achieved a higher resolution of 0.15 eV in measurements using 200-keV H^+ impact. Figure 23 shows the results demonstrating that with the present resolution it is possible to observe indications of the natural line width in the diagram lines. Nevertheless, due to the complexity of the Ar-L spectrum line blending cannot completely be avoided.

The ion impact studies of the normal lines are in accordance with the corresponding measurements using electron impact, see e.g. Mehlhorn and Stahlherm [183] and Werme et al. [184, 185]. A detailed

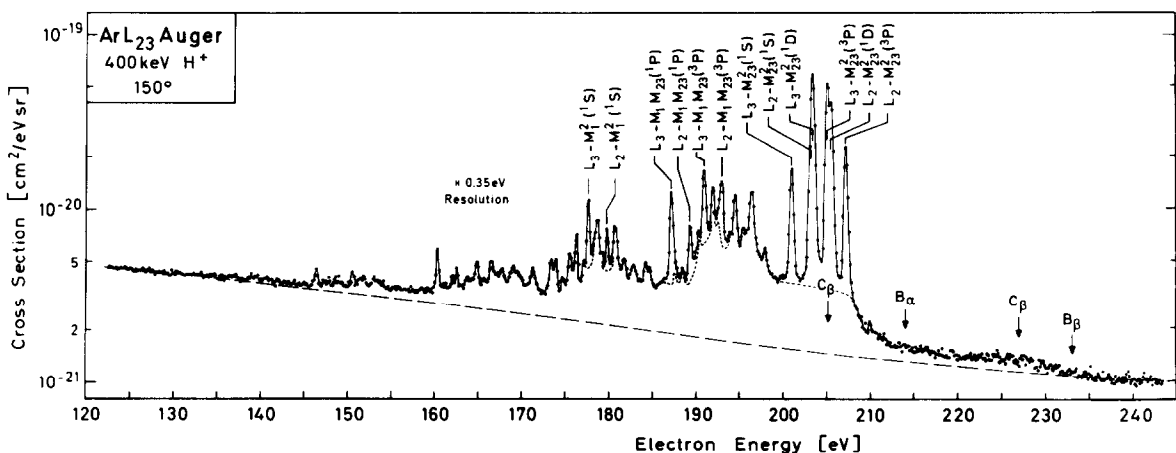


Fig. 22. Argon- L_{23} -Auger spectrum observed at 150° by 400-keV H^+ impact. Normal lines are marked. Energies of Auger electrons from initial states involving the occupation of 4s and 3d levels are labelled B_α , C_α , B_β and C_β . From Stolterfoht et al. [181].

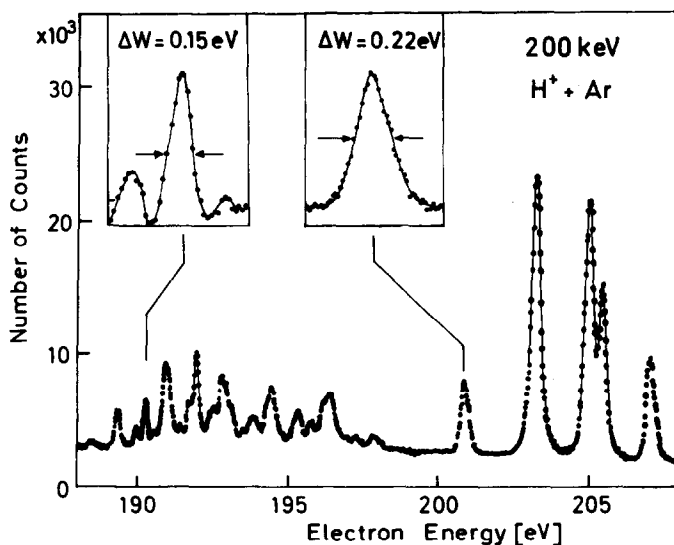


Fig. 23. Argon-L₂₃-Auger spectrum produced in 200-MeV H⁺ + Ar collisions. The normal line shown in the right-hand side inset exhibits partially the natural line widths of the L₂₃-vacancy state. From Ridder et al. [182].

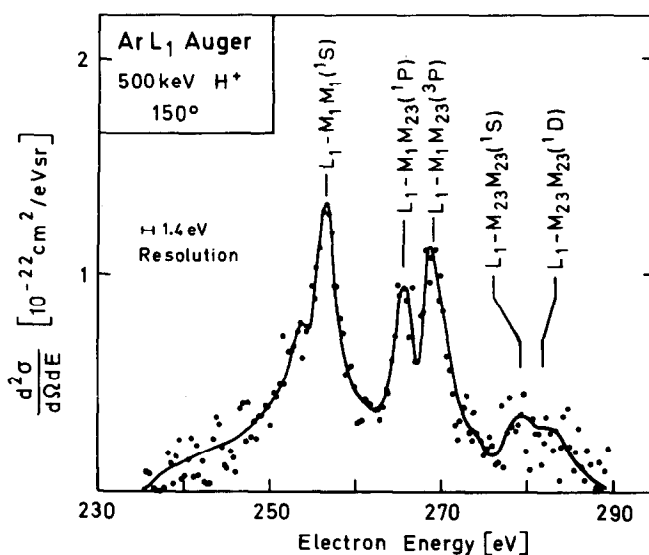


Fig. 24. Argon-L₁-Auger spectrum observed at 150° by 500-keV H⁺ impact. Continuous background is subtracted. From Stolterfoht et al. [181].

theoretical analysis of the Ar-L-Auger spectrum has been made by McGuire [139]. In that work, the doublet conventionally assigned to L₂₃-M₁M₁(¹S) has been proposed to be reassigned to a CI satellite connected with L₂₃-M₁M₂₃(¹P). Furthermore, Ridder et al. [128] performed a high-resolution study of the fine structure splitting of the L₂₃-MM(³P) states in accordance with the mixed coupling calculations by Asaad and Mehlhorn [126].

The L₁-Auger spectrum is difficult to study, since it can barely be seen above the continuous electron background. This is due to the fact that most L₁-vacancies decay by Coster-Kronig transition giving rise

to electrons of energies near 30 eV [186]. Nevertheless, a noticeable L_1 -Auger spectrum remains near 250 eV as shown in fig. 24. The data are produced by 500-keV H^+ impact using an energy resolution of 1.4 eV [181]. Mehlhorn [186] found a natural L_1 -line width of 1.84 eV which is considerably larger than the L_{23} -line width of 0.13 eV [187]. This is due to the Coster–Kronig transitions which enlarge the L_1 -level width, see eq. (1.2.2).

In figs. 22 and 23 the Ar-L-Auger spectrum exhibits a large number of satellite lines originating from the ionization of the outer M-shell in addition to the removal of the L-shell electron. The complexity of the Ar-L satellite structures requires a detailed study of the Auger spectrum. For light ion impact the total intensity of the satellite lines has been determined by Stolterfoht et al. [181, 188] and Watson and Toburen [189] whose results are given in table 5. It is seen that for H^+ impact about half of the spectral intensity originates from satellite lines. When helium is used as projectiles, the relative satellite intensity is found to be even larger. Due to screening effect, the satellite line production is slightly reduced for He^+ impact in comparison with He^{2+} impact.

There are different mechanisms producing M-shell vacancies in addition to the vacancy in the L-shell. Apart from electron shake-off [165] and successive Coulomb-excitation of the inner and outer shell, Coster–Kronig transitions following the production of L_1 vacancies are causing M-shell ionization. Similarly as the probability for electron shake-off, the probability for Coster–Kronig transition is nearly independent of the excitation mode. Hence, for L-Auger spectra one expects a rather high contribution of a constant satellite intensity in the Ar-L-Auger spectrum. Indeed, in the Ar-L-Auger spectra the relative satellite intensity for electron impact is found to be 0.35 [190] in comparison with 0.21 for the Ne-shell [166] (see also above).

As in K-Auger spectra, the number of satellite lines increases strongly in the L-Auger spectrum when heavy ions are used as projectiles. Heavy ion-induced Ar-L-Auger spectra have been measured by Volz and Rudd [162], Stolterfoht et al. [191], Johnson et al. [192], Schneider et al. [193], Folkmann et al. [194], and Matsuo et al. [195]. Figure 25 shows spectra obtained by Matsuo et al. [195] using 6.6-, 14.3- and 21.0-MeV Ar^{4+} impact. In these spectra only satellite lines are seen. In particular near 100 eV, the spectrum exhibits a pronounced peak pair which is attributed to the Na-like doublet state $1s^2 2s^2 2p^5 3s^2 \ ^2P$. This doublet has also been observed by Mann et al. [20]. It will be considered in more detail in conjunction with the projectile Auger spectra (section 5).

With regard to the Na-like configurations of Ar it is interesting to consider the L-Auger spectrum of Na itself. Figure 26 shows data measured with 300-keV H^+ impact on an Na-vapour target by Ziem et al. [196]. Similar results have been obtained by Theodosiou et al. [197] using also He^+ impact. The spectrum clearly shows the $1s^2 2s^2 2p^5 3s^2 \ ^2P$ doublet whose $J = \frac{3}{2}$ component has been studied in detail to verify the angular distribution of the ejected Auger electrons [196, 197]. Also, the spectrum shows some

Table 5
Intensity of all Ar-L satellite lines normalized to the total Auger intensity for H^+ , He^+ and He^{2+} impact

Energy/mass [keV/u]	H^+ Impact ^{a)}	He^+ Impact ^{a)}	He^{2+} Impact ^{b)}
100	0.58	0.82	–
250	0.49	0.74	0.83
500	0.41	–	0.67

a) Stolterfoht et al. [181].

b) Watson and Toburen [189].

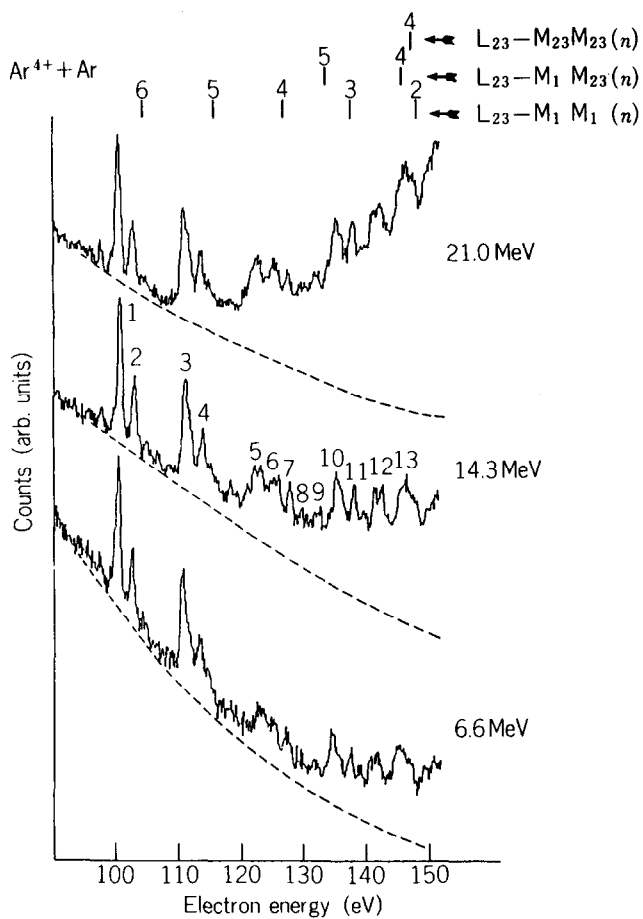


Fig. 25. Argon- L_{23} spectrum of Auger electrons from the target atom excited in 6.6-MeV, 14.3-MeV and 21.0-MeV Ar^{4+} collisions. Calculated transition energies given above the spectrum are labelled by the number of 3p holes in the initial state. From Matsuo et al. [195].

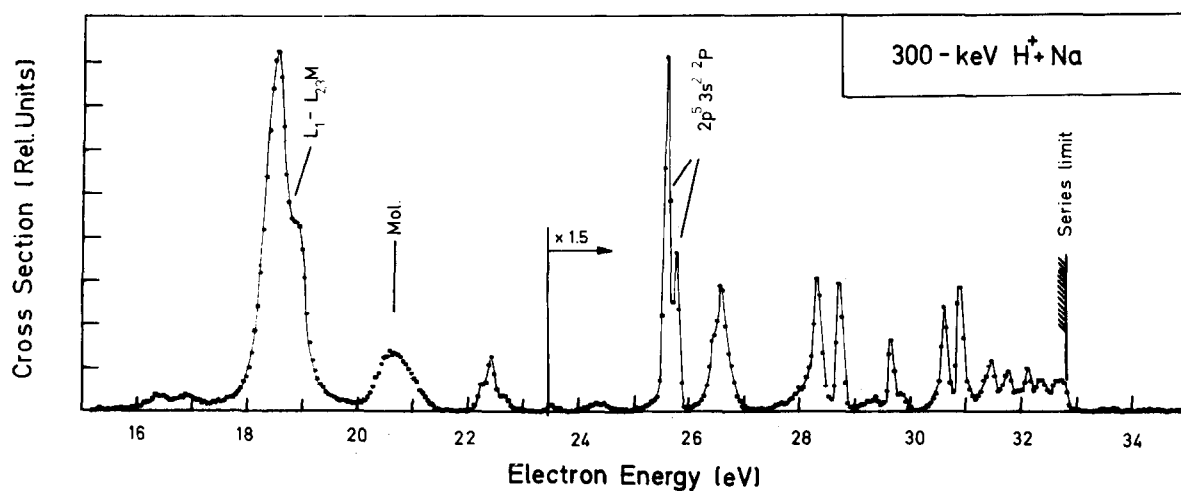


Fig. 26. Na-L-Auger spectrum produced by 300-keV H^+ impact. Continuous background is subtracted. From Ziem et al. [196].

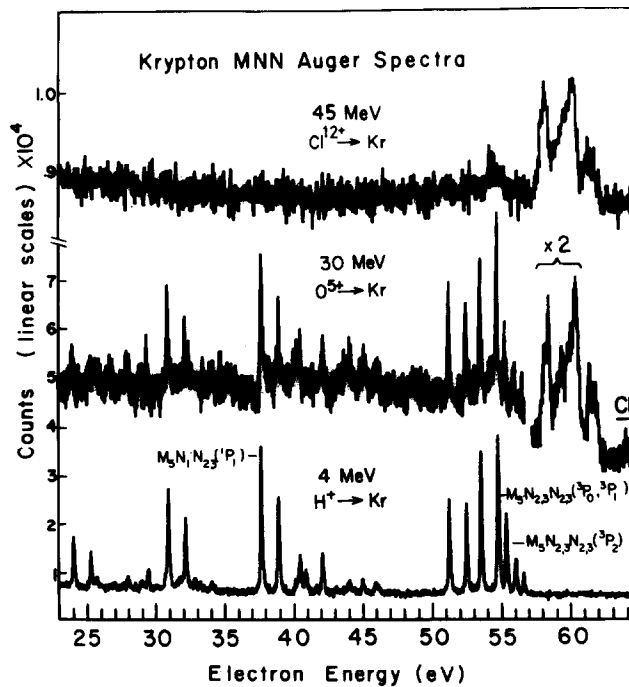


Fig. 27. Krypton-M-Auger spectrum produced at 90° by 3-MeV H^+ , 30-MeV O^{5+} and 45-MeV Cl^{12+} impact. Some diagram lines are marked. From Schneider et al. [193].

peaks due to $L_1-L_{23}M$ Coster-Kronig transitions. It is interesting to note that these transitions are energetically forbidden for Na-like Ar (section 5).

As an example for M-shell spectra, results for the target atom Kr are shown in fig. 27. The data are measured by Schneider et al. [193] using 4-MeV H^+ , 30-MeV O^{5+} and 45-MeV Cl^{12+} impact. As expected, the 4-MeV H^+ spectrum exhibits primarily normal lines. However, surprisingly, also the 30-MeV O^{5+} spectrum is seen to consist essentially of normal lines. Hence, the conclusion from K-Auger and L-Auger spectra that heavy ions produce primarily satellite lines, is not necessarily true for the M-shell.

Nevertheless, a few satellite lines are observed in the 30-MeV O^{5+} spectrum near 60 eV (fig. 27). This peak group is produced even more strongly by 45-MeV Cl^{12+} excitation. Schneider et al. [193] attributed the group to states involving the occupation of higher-lying Rydberg states. However, this line interpretation should not be regarded as conclusive. Further work is needed to study the systematics of the M-shell ionization.

4.4. Statistical analysis of the Auger spectra

4.4.1. Statistical relations

The large number of inner-shell vacancy states produced in most heavy-ion atom collisions suggests to apply statistical methods to analyze the Auger spectra. Furthermore, it appears useful to utilize average quantities for the interpretation of the experimental data [16].

For the analysis of multiple ionization the fraction f_s of the Auger spectrum due to satellite lines is considered, i.e.

$$f_s = \sigma_s / \sigma_1 \quad (4.4.1)$$

where σ_s is the cross section for producing satellite lines and σ_1 is the total cross section for ionization of the inner shell. In the impact parameter approach, the cross section for inner-shell ionization is obtained as

$$\sigma_1 = 2\pi \int P_1 b db \quad (4.4.2)$$

where P_1 is the impact parameter b dependent probability for ionization of the inner shell. When the processes of inner- and outer-shell ionization are uncorrelated, one may set

$$\sigma_s = 2\pi \int P_1 P_s b db \quad (4.4.3)$$

where P_s is the probability for producing vacancies in the outer shell. The probability $P_s = P_s^o$ is approximately constant within the inner-shell region where the integration (4.4.3) is performed so that $\sigma_s = P_s^o \sigma_1$. Then, it follows that the fraction of satellite intensity is equal to the probability for producing vacancies in the outer shell:

$$f_s = P_s^o \quad (4.4.4)$$

It is emphasized that both ionization as well as electron capture contribute to the vacancy production in the outer shell [170].

In violent collisions, the outer shell may become multiply ionized. Let P_n be the probability for producing the number of n vacancies with the normalization $\sum_{n=0}^{n_o} P_n = 1$ where n_o is the number of outer-shell electrons. Since any kind of outer-shell ionization contributes to the satellite line intensity, it follows that

$$P_s = \sum_{n=1}^{n_o} P_n = 1 - P_0 \quad (4.4.5)$$

The probability P_0 refers to the fraction of the Auger spectrum due to normal lines.

In the statistical treatment of outer shell excitation, multiple vacancy production is governed by a binomial distribution. For the L-shell ($n_o = 8$) it follows that

$$P_n = \binom{8}{n} p_L^n (1 - p_L)^{8-n} \quad (4.4.6)$$

where p_L is the single-particle probability for the removal of L-shell electrons. Equation (4.4.6) shows that all P_n 's may be calculated, if p_L or a single P_n is known. The application of the binomial distribution for the analysis of multiple ionization in ion-atom collisions has been proposed by Burch [198] and Hansteen and Mosebeck [199]. Recently, the use of the binomial distribution has been justified on an *ab-initio* basis by Åberg, Goscinski and collaborators [200, 201] using an information-theoretical approach.

Ionisation of 2s and 2p electrons may also be treated separately, i.e. one may use the extended

binomial distribution [53, 202]

$$P_{rt} = \binom{2}{r} p_{2s}^r (1 - p_{2s})^{2-r} \binom{6}{t} p_{2p}^t (1 - p_{2p})^{6-t} \quad (4.4.7)$$

where p_{2s} and p_{2p} are single-electron probabilities to create vacancies in the 2s and 2p subshells, respectively, and r and t are the corresponding vacancy numbers. From eq. (4.4.7) the probability P_n is derived as

$$P_n = \sum_{r,t} P_{rt} \quad (4.4.8)$$

with the constraint $r + t = n$. Evidently, for $p_{2s} = p_{2p}$ eqs. (4.4.6) and (4.4.7) yield the same result. From the probabilities P_n , the mean value for the number of outer-shell vacancies is obtained as

$$\bar{n} = \sum_{n=0}^8 n P_n. \quad (4.4.9)$$

It may readily be shown that $\bar{n} = 8p_L$.

4.4.2. Spectral analysis

Using eqs. (4.4.5) and (4.4.6) individual probabilities P_n for L-shell vacancy production may be evaluated from the satellite structure of the Auger spectra. It is recalled that the complete binomial distribution (4.4.6) is determined, if p_L or a single probability P_n is known.

For the case of 4.2-MeV H^+ the binomial distribution was derived from the probability P_0 to produce normal lines [16]. The results given in fig. 28 show that 4.2-MeV H^+ involve a noticeable probability for double L-shell vacancy production. Moreover, the statistical analysis for 100-keV H^+ impact indicates that the probability P_2 for producing two L-shell vacancies is nearly as large as the probability P_1 for producing a single L-shell vacancy. This shows that slow protons produce a significant amount of L-shell excitation when passing through the K-shell.

Similar as for H^+ -impact, the binomial distribution for O^{5+} -impact has been derived from the probability P_0 to produce normal lines [203, 204]. In the analysis, satellites due to the excitation of Rydberg states were disregarded. Also, P_1 was determined from the corresponding satellite intensity and it was found to be consistent with the binomial distribution [203]. For Cl^{12+} impact, P_6 was determined from the prominent Li-like lines occurring within 650 and 685 eV [16]. The results given in fig. 28 show that the degree of L-shell ionization increases significantly as the nuclear charge of the projectile increases.

From the binomial distributions in fig. 28, mean values \bar{n} for L-shell vacancy production are derived. For instance, $\bar{n} = 0.21, 2.9$ and 5.8 have been obtained for the projectiles 4.2-MeV H^+ , 30-MeV O^{5+} and 45-MeV Cl^{12+} , respectively [16, 203]. Furthermore, a functional relationship has been found between the centroid energy \bar{E}_c of the Auger spectrum and the mean number \bar{n} of outer-shell vacancies [16]. Figure 29 summarizes the data for various collision systems compiled by Schneider et al. [50], see also Kádár et al. [53]. The data in fig. 29 exhibit a linear relationship between \bar{E}_c and \bar{n} . This finding has been confirmed theoretically by Matthews [15] who calculated Auger energies as a function of the number of L-vacancies.

It is important to note that the data in fig. 29 are very valuable for cases where line-broadening

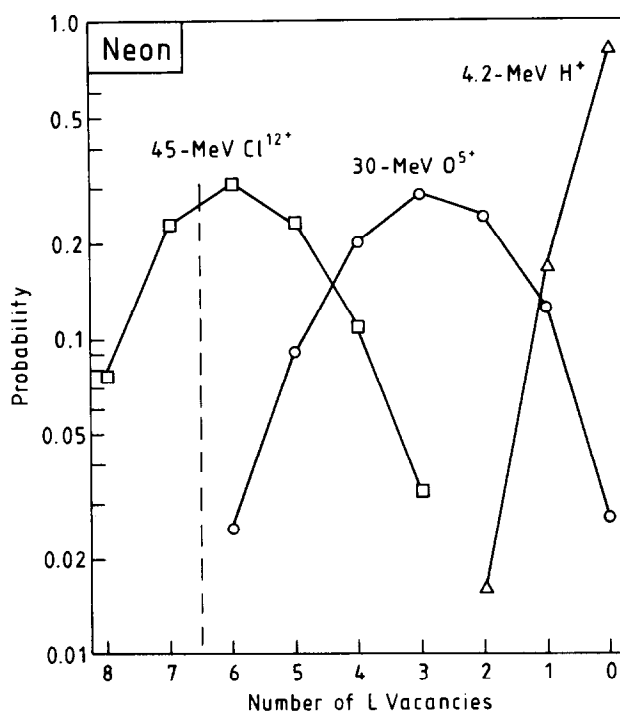


Fig. 28. Binomial distribution for the charge state in the L-shell produced during K-shell excitation of Ne by 4.2-MeV H⁺, 30-MeV O⁵⁺ and 45-MeV Cl¹²⁺. The results are from eq. (4.4.6) using data from the analysis of the spectra given in fig. 16.

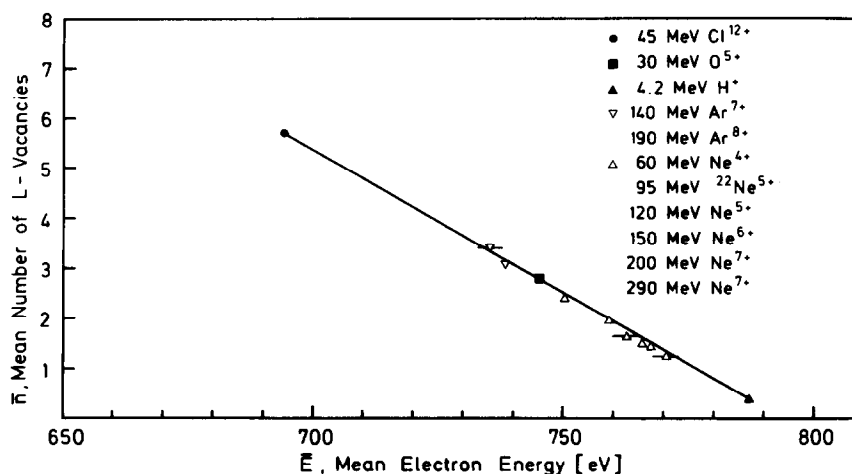


Fig. 29. Mean number \bar{n} of L-vacancies produced during K-excitation of Ne by various projectiles as a function of the mean energy \bar{E} of the Auger electrons. From Schneider et al. [50].

effects inhibit a detailed analysis of the Auger spectrum. For instance, the mean charge state of $\bar{n} = 2.8$ has been determined [156] for the 400-keV Ne⁺ + Ne spectrum in fig. 12. This shows that the degree of outer-shell ionization for 500-keV Ne⁺ impact is nearly the same as that for 30-MeV O⁵⁺ impact (fig. 12) for which $\bar{n} = 2.9$ was found as mentioned above.

From the binomial distribution (4.4.6) the single-electron probability p_L for the L-shell ionization is

obtained. In fig. 30 experimental results for Ne are summarized [53]. The data originate from Auger measurements by Schneider et al. [50], Kádár et al. [53], Mann et al. [20] and from X-ray measurements by Folkmann et al. [205].

Various attempts were made to evaluate the probability p_L theoretically [199, 206, 207]. The problem with this evaluation is that the probability p_L tends towards unity when multiple ionization becomes significant. Then, perturbation methods are expected to fail. In particular, the dependence of p_L on the square of the projectile charge Z_p predicted by the Born-approximation [199] or the binary encounter theory [206] are not supposed to be valid.

Sulik et al. [207] introduced a simple binary encounter model which includes features beyond first-order perturbation theory. The method is expected to be valid for projectile velocities v_p larger than that of the outer-shell electrons. Sulik et al. [207] obtain

$$p_L = 1 - \frac{1}{2}x^2 K_2(x) \quad (4.4.10)$$

where $x = 2Z_p/v_p$ and K_2 is the modified Bessel function [75]. It is noted that the Z_p/v_p scaling of p_L has been proposed previously [20, 50, 206].

Results from eq. (4.4.10) are given in fig. 30 where Z_p is replaced by the effective charge Z_{eff} . For $Z_p/v_p \ll 1$ the Z_p^2 dependence of p_L predicted by first-order perturbation theory is reproduced. Furthermore, p_L approaches 1 for $Z_p/v_p \gg 1$, as expected. In the range of intermediate Z_p/v_p values, p_L is about proportional to Z_p . The experimental values given in fig. 29 show good agreement with the theoretical results for small Z_p/v_p where perturbation theory is expected to be valid. In the intermediate Z_p/v_p range, good agreement is achieved between theory and results from X-ray measurements, whereas discrepancies occur when the theory is compared with results from some Auger measurements.

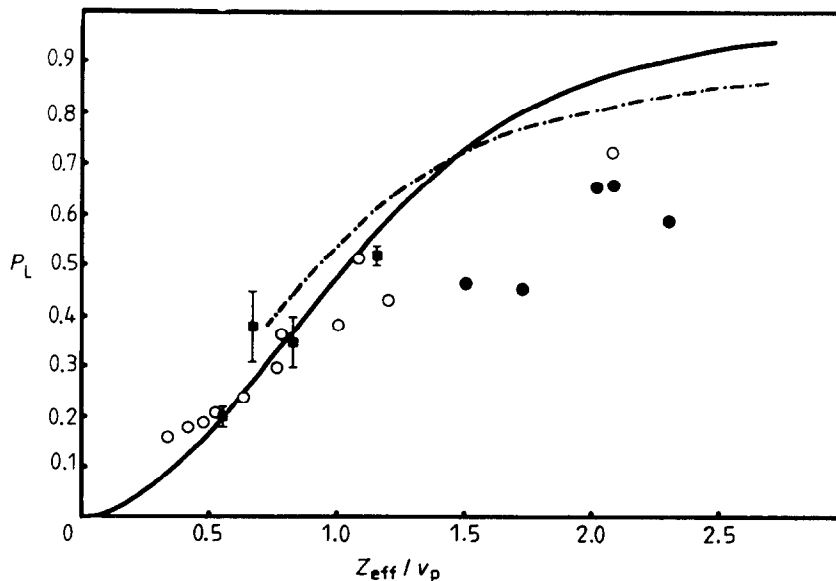


Fig. 30. Single electron probability for vacancy production in the L-shell as a function of the ratio of the effective projectile charge Z_{eff} and the projectile velocity v_p . Theoretical results (solid curve) are from Sulik et al. [207]. Experimental results from X-ray measurements [207] are from Folkmann et al. [205] (chain curve). Experimental results from Auger measurements are from Schneider et al. [50] (open circles), Mann et al. [20] (full circles), and Kádár et al. [53] (squares). From ref. [53].

It is difficult to judge the validity of the theoretical approach as well as the reliability of the experimental data. The theoretical results are based on a model assuming ionization to be the most significant for outer-shell vacancy production. However, it is very likely that electron capture plays an important role when a highly stripped projectile passes the target atom at small impact parameters [52]. Hence, it appears necessary to take capture processes into consideration when the probability p_L is calculated.

The experimental data for p_L are based on the assumption that outer-shell ionization is governed by a binomial distribution. Actually, this assumption has never been fully verified. The binomial distributions have been used extensively in the field of X-ray spectroscopy in good agreement with the experimental data [202]. However, because of the uncertainties in the fluorescence yields, it is difficult to draw definite conclusions from the X-ray analysis.

The verification of the binomial distribution would need the experimental determination of P_n for various charge states n . In Auger electron studies, only P_0 and P_1 [203] as well as P_0 and P_6 [53] have been determined simultaneously. In the first case, consistency was achieved with the binomial distribution. The latter case exhibits discrepancies which, however, may be attributed to differences in the ionization probabilities for the 2s and 2p electrons [53], see eq. (4.4.7).

Another problem involved in the experimental data is due to the fact that in cases where the projectile carries electrons, Z_p is replaced by some effective projectile charge Z_{eff} . To determine the effective charge, a simple classical model by Toburen et al. [180] has been applied as well as quantum mechanical models [53, 208, 209] based on first-order perturbation theory. Both types of models should be applied with caution to the complex collisions regarded here. It is felt that further work is needed to describe adequately the violent collisions where several electrons are affected simultaneously.

4.5. Analysis of individual lines

4.5.1. Lithium-like states

It is an important observation that the Auger spectra become simpler, when the nuclear charge of the projectile is strongly increased (fig. 16). The simplicity of the Auger spectra produced by very heavy projectiles allows the detailed study of individual Auger lines for few-electron systems [49].

Before studying heavier target atoms, a few comments about Li shall be made. As noted in conjunction with fig. 17, the energy scale of the Li spectrum was calibrated by means of the $1s(2s2p^{1,3}P)^2P$ states whose energies have been measured with high accuracy by Ederer et al. [177]. Thus, the transition energies for Li have been determined within a few tenths of meV [176]. In this case it appears challenging to test theoretical methods for the evaluation of the transition energies [177, 178]. In particular the Li atom is well suited to study effects originating from configuration interaction.

Among heavier systems, the Li-like Auger lines of Ne have been studied most extensively in the past [20, 47, 50, 53, 174, 210–212]. In table 6 experimental and theoretical transition energies are summarized. The accuracy of the relative energies measured by Matthews et al. [204] and Mann et al. [212] is about ± 0.3 eV. Absolute values are obtained with an accuracy of about ± 1 eV. The theoretical results originate from nonrelativistic calculations [171] using the HF code by Froese-Fischer [97] and from relativistic calculations [211, 212] using the DF code by Desclaux [98]. Also, relativistic results by Chen et al. [147, 148] are given. It is seen that the relativistic results are in far better agreement with experiment than the nonrelativistic data. It appears that relativistic calculations are required for Li-like Ne, whereas for neutral Ne nonrelativistic calculations yield results of satisfactory accuracy (section 2.2).

Table 6
Transition energies (in eV) for Li-like states of Ne. Final ionic state is $1s^2\ ^1S$

Initial state	Expt. (a)	Expt. (b)	Theory (c)	Theory (d)	Theory (e)
$1s2s^2\ ^2S^e$	652.2	651.7	656.3	652.7	–
$1s2s2p\ ^4P^o$	656.5	656.2	655.6	656.3	656.0
$1s2s2p\ ^2P^o$	668.9	668.9	668.2	668.9	668.7
$1s2p^2\ ^4P^e$			672.6	673.5	673.0
	674.1	673.6			
$1s2s2p\ ^2P^a$			672.3	675.6	675.6
$1s2p^2\ ^2D^e$	681.0	680.6	681.5	681.8	681.5
$1s2p^2\ ^2S^e$	–	–	–	693.3	693.4

a) Matthews et al. [204].

b) Mann et al. [212].

c) Matthews et al. [171] using the HF code by Froese-Fischer [97].

d) Schumann et al. [211] and Mann et al. [212] using the DF code by Desclaux [98].

e) Chen et al. [147, 148].

An interesting problem which emerges from the analysis of individual lines is whether the excitation of multiplet terms follows statistical rules. These rules would predict that the excitation probability of a multiplet term ^{2S+1}L is proportional to $(2S+1)(2L+1)$, i.e. the number of sub-levels involved. The statistical model is conventionally applied in the field of inner-shell excitation involving individual states. Such calculations lose their basis when mechanisms become important resulting in selective excitation of certain Auger states.

First indications for nonstatistical population of the KL-satellite line of Ne has been observed by Schmidt [213] and Bhalla et al. [214] using light-ion impact. To study heavier collision systems, Matthews et al. [210] analyzed the data of 45-MeV $Cl^{12+} + Ne$ presented previously (fig. 16). Figure 31 shows the low-energy part of the spectrum containing the Li-like lines. The experimental data are compared with a theoretical spectrum derived on the basis of the $(2S+1)(2L+1)$ excitation rule. In the analysis the probabilities for the removal of 2s and 2p electrons are assumed to be equal. It is seen that the states based on the configurations $1s2s^2$ and $1s2s2p$ are overpopulated in relation to the configuration $1s2p^2$. Matthews et al. [210] suggested that the $1s2s^2\ ^1S$ state is populated by selective cascade feeding transitions.

However, according to eq. (4.4.7) the enhanced production of the configuration $1s2s^2$ (and also $1s2s2p$) in the 45-MeV $Cl^{12+} + Ne$ spectrum may be explained by the favoured removal of the 2p electron in comparison with the 2s electron [49]. Such effect is expected, since the 2p electron is less bound than the 2s electron. On the other hand, the analysis of the 200-MeV $Xe^{31+} + Ne$ spectrum (fig. 16) has shown that the excitation of the $1s2s^2$ configuration is less probable than expected from the statistical rules. In this case, the removal of the 2s electron appears to be favoured in comparison with the 2p electron [47]. Similar results have been found by Kádár et al. [53] using 5.6-MeV/u Ne^{10+} and Ar^{6+} impact on Ne. This may be an indication for the fact that in specific collision systems the removal of L-shell electrons is caused by electron capture rather than by ionization. In fast collisions the capture of a more tightly bound electron is often favored.

Selective cascade feeding is most likely expected to occur for the $1s2s2p\ ^4P^o$ state. It is the lowest-lying member of a series of metastable quartet states which may cascade down by radiative transitions [47, 215]. The cascade feeding of the quartet state is a well-known phenomenon in the field

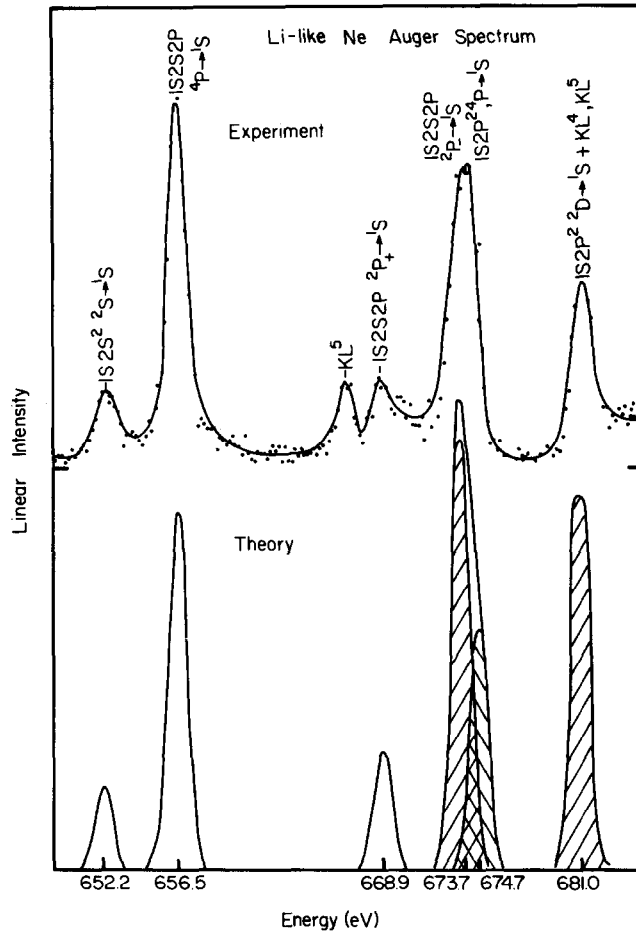


Fig. 31. Comparison of the experimental Ne-K-Auger spectrum produced by 45-MeV Cl^{12+} impact with a theoretical spectrum based on the assumption of statistical line excitation. From Matthews et al. [210].

of beam-foil spectroscopy [55, 56]. In the present 45-MeV $\text{Cl}^{12+} + \text{Ne}$ spectrum, it was found that the line due to the $1s2s2p\ ^4P$ state is excited with higher probability than expected from statistical rules [210]. The overpopulation of the $1s2s2p\ ^4P$ state was observed to be even stronger in the 200-MeV $\text{Xe}^{31+} + \text{Ne}$ spectrum [47].

4.5.2. Recoil Auger spectroscopy

In $\text{Xe}^{31+} + \text{Ne}$ spectrum the peak group between 650 eV and 680 eV is attributed to the configurations $1s2s^2$, $1s2s2p$ and $1s2p^2$ as discussed in conjunction with fig. 16. Apart from this, another peak group is observed in the range of 850 eV to 900 eV. This group has been identified as being due to configurations such as $1s2s4p$ and $1s2p4p$ [49, 212]. Hence, the two peak groups are attributed to configurations implying outermost electrons with the principal quantum numbers $n=2$ and $n=4$. Naturally, the question arises why lines do not occur due to configurations with $n=3$ which are expected around 800 eV.

The answer is that configurations neither with $n=3$ nor with $n=4$ are produced with significant probability in the primary collision. The configurations with $n=4$ are selectively created in secondary

collisions with the target gas atoms. The secondary collision process can occur when the target gas pressure is increased. This has been shown in 125-MeV $\text{Kr}^{19+} + \text{Ne}$ collisions where the lines in the 850 eV to 900 eV energy range have been found to be significantly enhanced in relation to the total intensity of the spectrum [216].

A conclusive description of the secondary collision process producing autoionizing states has been given by Mann et al. [212, 217]. Impact of heavy ions produces, among others, He-like Ne from which a significant fraction is in the metastable state $1s2s\ ^3S_0$. These metastable states have lifetimes of 91 ns, so that charge exchange collisions occur between recoil ions and other target atoms. (The metastable state $1s2p\ ^3P$ lives only 9 ns so that secondary capture is rather unlikely.)

In fig. 32 the secondary capture process is illustrated. Electrons are transferred from the target atom to the recoil ion producing Li-like Ne in an autoionizing state. Since the recoil atoms have very low energies of the order of a few eV, the capture process takes place under extremely resonant conditions favoring the population of levels with certain n quantum numbers. For Ne target atoms, preferential capture into the $n = 4$ levels of the Ne^{8+} recoil in the metastable state $1s2s\ ^3S$ takes place. Then, the autoionizing configuration $1s2p4l$ is produced by a transfer-excitation process [218].

The selectivity of the secondary charge transfer process has been demonstrated by Mann et al. [217] adding other gas components in the target region. In collision between metastable Ne^{8+} and He, the production of the configuration $1s2s4l$ is favored. This may be seen from fig. 33, where Auger spectra within the 800 eV to 900 eV energy range are shown for the collision system 56-MeV $\text{Ar}^{12+} + \text{Ne}$ with various gas admixtures. Mann et al. [212, 217] use a particular short-notation to specify the lines. For instance, the state $1s2s(^3S)nl\ ^{2S+1}L$ is abbreviated by 3Sn assuming that the state energies are not significantly affected by the angular momentum l and by the coupling to the term ^{2S+1}L . This assumption is valid for Rydberg electrons with $n \geq 4$. Figure 33b shows that the secondary collisions

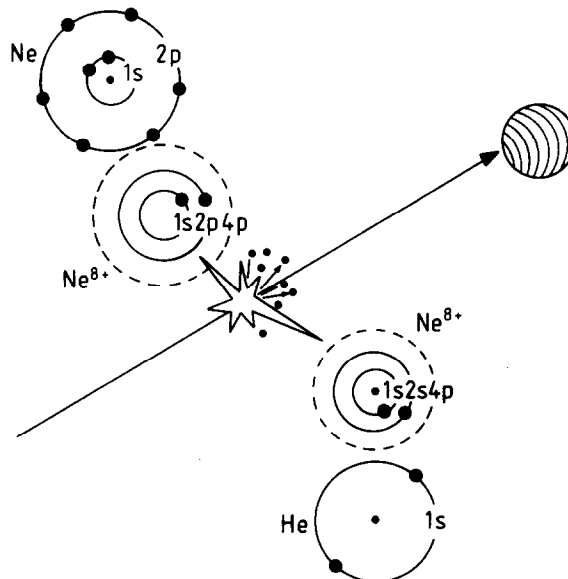


Fig. 32. Diagram illustrating the process of secondary capture of electrons by the recoil ions produced in violent ion-atom collisions. Note that different states are occupied when collisions with different gas target occur.

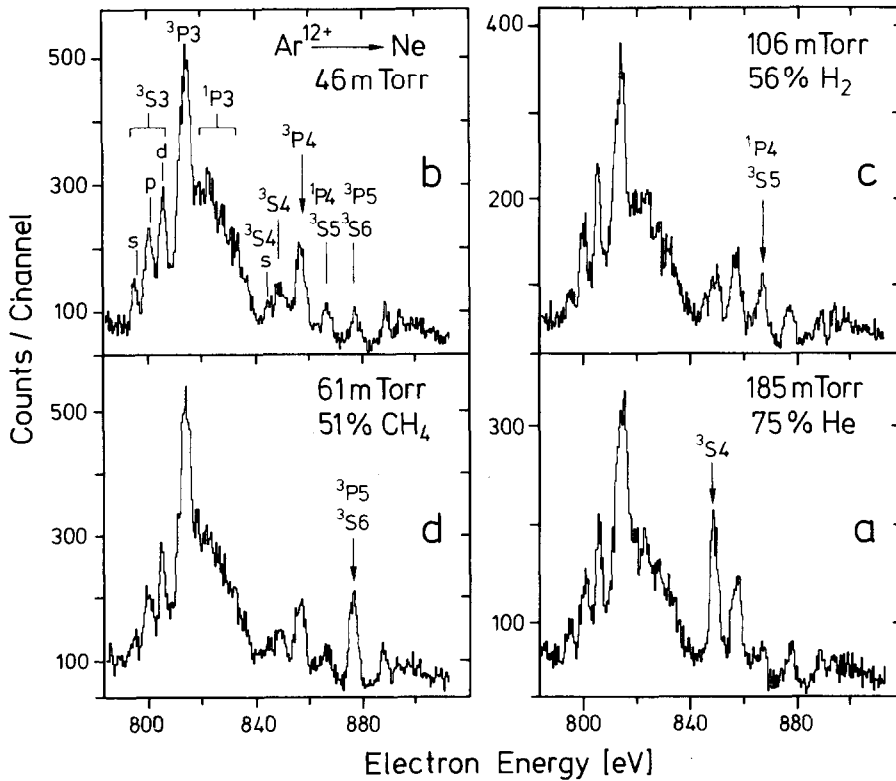


Fig. 33. Neon-K-Auger produced by 56-MeV Ar^{12+} impact. The spectrum in (b) is obtained using a pure Ne gas target of 46 mTorr. The spectra in (a), (c) and (d) are obtained with contaminations of He, H_2 and CH_4 in the Ne gas targets as indicated. The label e.g. $^3\text{P}5$ denotes $1s2p(^3\text{P})5l^{2s+1}\text{L}$. From Mann et al. [212].

with the Ne target gas populates the $^3\text{P}4$ states. Similarly, figs. 33a, c and d demonstrate that the gas admixtures He, H_2 and CH_4 enhance primarily the states $^3\text{S}4$, $^3\text{S}5$ and $^3\text{S}6$, respectively.

The selective electron capture may be understood by means of the classical over-barrier model [219, 220]. It assumes that charge exchange takes place resonantly when the binding energy B_n of the electron captured into the shell with quantum number n is equal to the binding energy B_0 of the neutral collision partner increased by the Coulomb energy $(q - 1)/R_c$. Here, q is the charge state of the ionic collision partner and R_c is the internuclear distance at which the charge exchange channel opens classically due to the receding potential barrier [221]. With use of the Rydberg formula for the binding energy $B_n = q^2/2n^2$ it follows for the principal quantum number

$$n \approx q \left[2B_0 \left(1 + \frac{q-1}{2q^{1/2} + 1} \right) \right]^{-1/2}. \quad (4.5.1)$$

Hence, n varies with varying ionization potential of the neutral collision partner. Excellent agreement was found between the principal quantum numbers n experimentally obtained for various target gas admixtures and the theoretical predictions [217].

Additional information about the dynamics of the secondary capture process is obtained, when the Auger spectra are recorded with some time delay after the collision event. In fig. 34 prompt and delayed spectra are compared for the collision system 56-MeV $\text{Ar}^{12+} + \text{Ne}$ [217]. The prompt spectrum

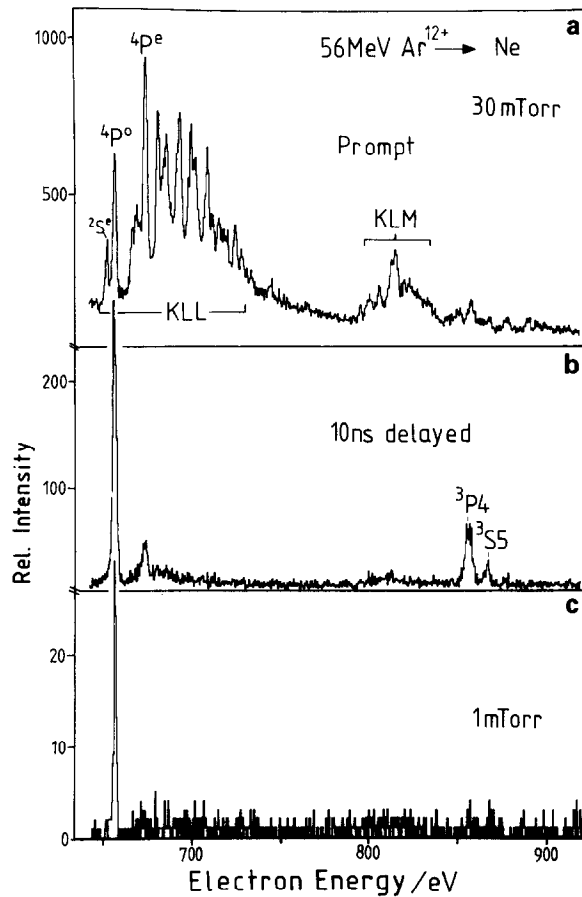


Fig. 34. Neon-K-Auger spectra produced by 56-MeV Ar^{12+} impact. The prompt spectrum is shown in (a). Spectra acquired with 30 mTorr and 1 mTorr target gas Ne and delayed by 10 ns are shown in (b) and (c), respectively. From Mann et al. [217].

exhibits numerous lines due to Li-, Be- and B-like states produced in the primary collisions. In the spectrum measured with 10 ns delay and with relatively low target gas pressure of 1 m Torr, only the line due to the metastable state $1s2s2p\ ^4P_{5/2}^o$ survives. This is understood, since the $^4P_{5/2}^o$ state has a relatively long life time of 10.4 ns [211].

In the delayed spectrum recorded with higher target gas pressure of 30 mTorr, the secondary capture peaks 3P_4 and 3S_5 appear. This is expected since their formation takes place within the life time (91 ns) of the Ne^{8+} recoils in the metastable states $1s2s\ ^3S$.

The delayed 30-mTorr spectrum exhibits an additional line which is attributed to the metastable $1s2p^2\ ^4P^e$ state. This line is a direct proof for the cascade feeding mechanism discussed previously [49, 210]. States produced by secondary capture involving a Rydberg electron may be of quartet type, e.g. $1s2p3s\ ^4P^o$. Due to the *LS*-coupling selection rule (table 3), such states have relatively small Auger decay rates, so that the radiative decay to the lowest member $1s2p^2\ ^4P^e$ dominates. In fact, also the $1s2s2p\ ^4P^o$ state is affected by cascade feeding, so that its intensity is enhanced (fig. 14).

Strong indication for the feeding of the quartet states by secondary capture processes is that the corresponding lines are broadened. In the capture process considered here, a highly ionized particle

approaches a neutral atom without much Coulomb interaction. However, by the charge exchange event, two ions are formed which repel each other strongly. Thus, in the out-going part of the collision the (exothermic) Coulomb energy $E_{ex} = (q - 1)/R_c$ is shared between the collision partners. Hence, the ion emitting the Auger electron is moving giving rise to kinematic line broadening effects. The line broadening is clearly seen by comparing the $1s2s2p^4P^o$ lines in figs. 34b and c.

To calculate the broadening ΔB_s due to secondary capture, Mann et al. [212] have given a simple formula whose derivative is similar to that for eq. (3.2.9):

$$\Delta B_s = 4 \left[\varepsilon E_{ex} \frac{M}{M_0(M + M_0)} \right]^{1/2} \quad (4.5.2)$$

where M and M_0 are the masses of the recoil ion and the neutral atom, respectively, and ε is the energy of the Auger electron.

In the high-energy collisions considered here, the exothermic energy E_{exo} is usually larger (typically 30 eV) than the recoil energy (≈ 5 eV). Hence, in general, the broadening from eq. (4.5.2) dominates the azimuthal broadening from eq. (3.2.9). Mann et al. [217] calculated the line broadening by means of eq. (4.5.2) for various collision systems in good agreement with the experimental data.

The process of secondary capture has also been studied by means of Ar-L-Auger electrons [51, 194]. As discussed in section 4.2.2, Ar may be multiply ionized in violent collisions. For instance, Ne-like Ar may be produced and, hence, the metastable states $1s^22s^22p^53s^3P_{02}$ are excited, among others. These states live sufficiently long so that secondary collisions with atoms of the target gas or admixtures occur. Then, electrons are transferred to higher-lying orbitals of the recoil ions. Results by Folkmann et al. [194] are given in fig. 35. It shows prompt and delayed Auger spectra originating from Ar recoils produced by 5.9 MeV/u U^{66+} projectiles. It is seen that secondary collisions with the target atoms Ar favor the occupation of the 6s and 6p orbitals. Alternatively, the admixture He and NH_4 populates primarily the 4f and 6d orbitals, respectively, thus, various Auger transitions in Na-like Ar have been investigated in detail [194]. It should be added that the electron capture by Kr^{8+} in the configuration $3d^{-1}3s$ has been studied recently [222].

4.5.3. Molecular Coulomb explosion

The repulsion of the collision partner after the charge exchange event may be regarded as a Coulomb explosion. Similarly, the picture of Coulomb explosion may be applied to molecular target species which become multiply ionized in a violent collision. Due to the strong Coulomb forces produced, the molecule will disintegrate quickly. Hence, fragments of the molecule are ejected from the center-of-mass similar to an explosion [223–225].

The spectra of the prompt Auger electron from the exploding system exhibit features of the molecular compound. The life time of the promptly decaying Auger states is small in comparison with the disintegration of the molecule. Hence, the molecular Auger spectra are rather complicated and their interpretation lies outside the scope of this article. Details about the analysis of molecular Auger spectra may be obtained elsewhere [225, 226].

The $1s2s2p^4P_{5/2}^o$ state of light ion lives some nanoseconds which is long enough to survive the Coulomb explosion. Hence, contrary to the prompt Auger spectra, lines due to metastable states reveal characteristic information of the molecular fragments. The Coulomb explosion has the primary effect of transferring kinetic energy to the ejected molecular fragments. Hence, the electrons from the metastable states are ejected from moving emitters, so that kinematic line broadening effects occur.

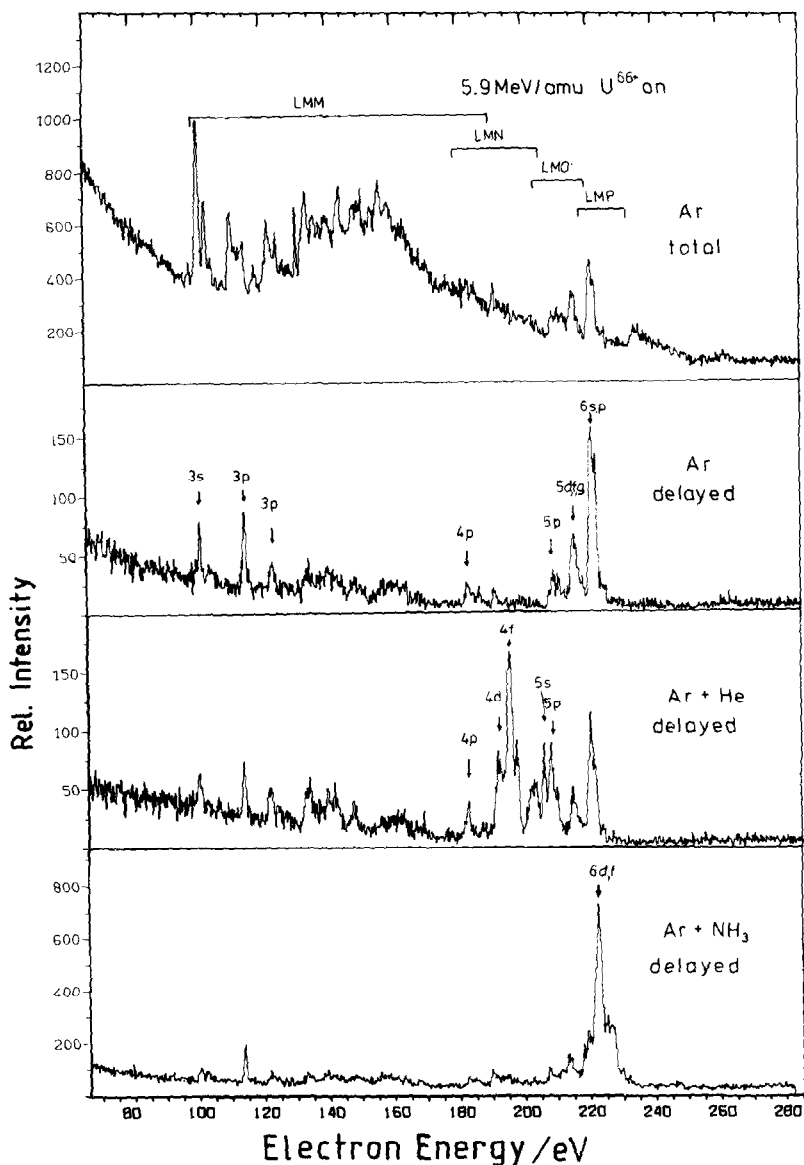


Fig. 35. Prompt and delayed Auger spectra produced in collisions of 5.9 MeV/u U^{66+} projectiles with Ar target with admixtures He and CH_4 . The delayed spectra are accumulated 10–30 ns after the beam pulse. From Folkmann et al. [205].

This may be seen in fig. 36 showing data obtained with 56-MeV Ar^{12+} impact by Mann et al. [224]. The figure depicts the $1s2s2p\ ^4P$ line for carbon originally bound in the molecular compounds CH_4 and CO.

The width of the 4P may be understood from the steric structure of the molecules CH_4 and CO depicted in fig. 36. Since C is located in the center of gravity of the CH_4 molecular, it is plausible that the carbon fragment has a relatively low velocity after the Coulomb explosion. Alternatively, the carbon fragment from CO has a rather high velocity after the Coulomb explosion. Accordingly, the Auger line attributed to the $1s2s2p\ ^4P$ state is relatively narrow for CH_4 , whereas significant broadening occurs in the case of the gas target CO.

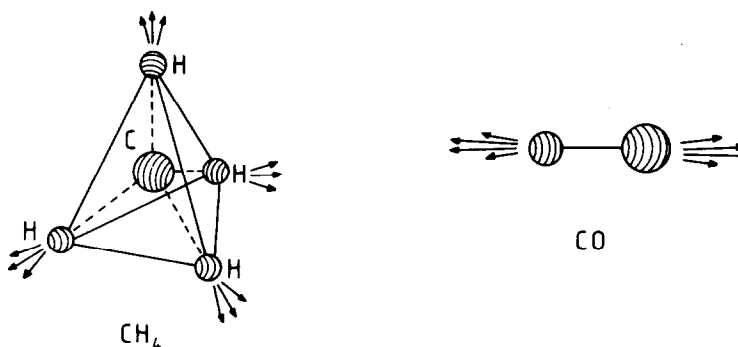
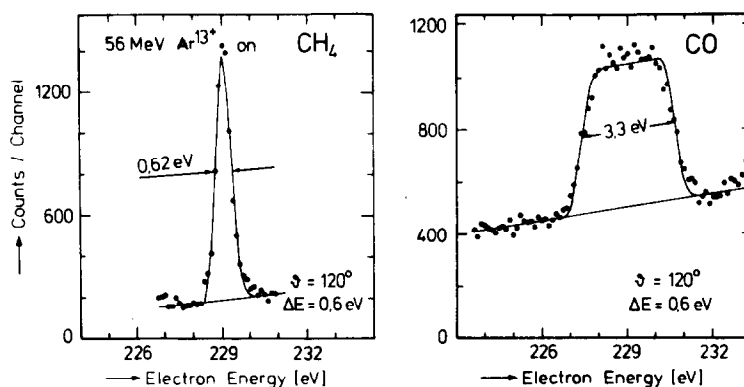


Fig. 36. Carbon-K-Auger spectra produced by 56-MeV Ar^{13+} impact on CH_4 and CO demonstrating the process of Coulomb explosion. Auger spectra are from Mann et al. [225].

For a given molecule, the width of the $1s2s2p^4P$ line increases with increasing nuclear charge of the projectile. This is shown in fig. 37 for CO_2 bombarded by 56-MeV Ar^{12+} , 118-MeV Kr^{18+} and 1.4 GeV U^{66+} [218]. The observed increase of the Auger line width is due to the increase of the degree of multiple ionization in the collision which enhances the strength of the molecular explosion.

Since the secondary capture in the outgoing part of the collision and the Coulomb explosion of two molecular fragments are similar processes, the same formula may be used to calculate the corresponding broadening effects, see eq. (4.5.2). In the case of Coulomb explosion, the (explosion) energy $Z_a^* Z_b^* / R_0$ is to be inserted for E_{ex} where Z_a^* and Z_b^* are the effective charges of the fragments a and b. The distance R_0 refers to the bond length of the molecule. For polyatomic compounds it may be assumed in an approximation that the molecule disintegrates into the emitter and the remaining (ionic) molecule [225]. From eq. (4.5.2) Mann et al. [224, 225] derived quantitative results for the shape of the Auger line in good agreement with the experimental results. From the comparison of the experimental and theoretical results information about the bond length and the effective charges of the molecular fragments have been obtained.

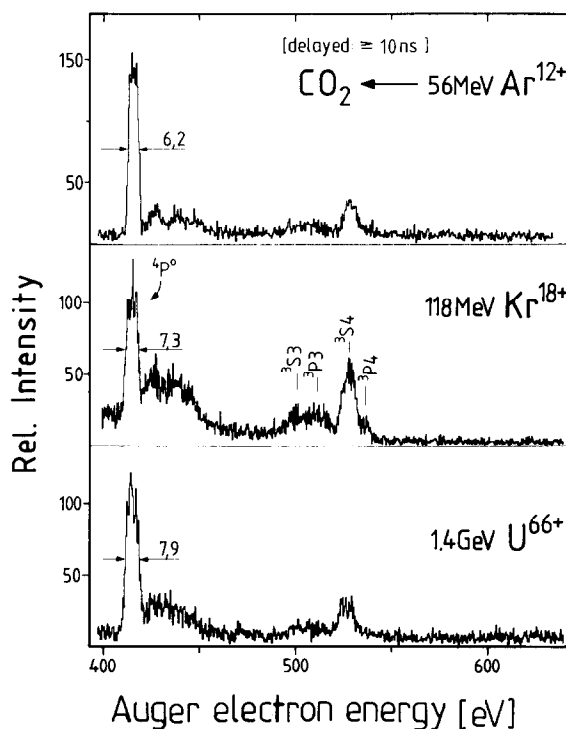


Fig. 37. Carbon-K-Auger spectra produced by 56-MeV Ar^{12+} , 118-MeV Kr^{18+} and 1.4-GeV U^{66+} impact on CO_2 . From Mann [218].

5. Projectile Auger spectroscopy

5.1. General considerations

The important potential of the projectile Auger spectroscopy is its access to atomic species generally bound in molecular compounds. In the ion source used with the particle accelerator, the molecular compounds break apart, and free ions may be extracted. Hence, studies of isolated atoms are possible for a large variety of atomic species. In particular, information about Auger states may be obtained for isoelectronic sequences.

Projectile Auger electrons originate from moving emitters which have rather high velocities. Hence, the Auger lines observed in the laboratory frame of reference are strongly influenced by kinematic effects. In particular, the polar broadening effect produced by the finite acceptance angle of the spectrometer plays a significant role. Hence, specific effort is needed to perform high-resolution studies of Auger electrons from fast projectiles.

In the field of projectile Auger spectroscopy, foils were often used as targets. The beam-foil technique initiated by Sellin, Pegg and collaborators [55, 56] for Auger electrons is similar to that used in the field of optical spectroscopy [227]. The life time of the Auger states is sufficiently long, so that most Auger decays take place after the projectiles have emerged from the foil surface. Hence, generally, the projectile Auger electrons originate from an isolated atom and, thus, the corresponding Auger spectra yield information about the atom free of solid state effects.

The use of a foil has the advantage that a rather localized target region is defined with respect to the direction of the beam. Hence, foil excitation supplies an accurate zero for time delay measurements,

when the Auger emission is observed at some distance away from the foil. The beam-foil technique allows the determination of life times of the order of nanoseconds. In the field of Auger spectroscopy such life-time measurements are relevant for metastable states, e.g. $1s2s2p\ ^4P$ for Li-like ions.

The disadvantage of the foil target is the energy and angle straggling of the ion beam which may create considerable line broadening (section 3). Also, the incident ion suffers charge changing collisions during the passage through the foil so that without coincidence measurements the experimenter has no control over the charge state of the particles emitting the Auger electrons. Moreover, foil excitation populates readily higher-lying Rydberg states which, in turn, may subsequently repopulate Auger states of interest [55]. To avoid such problems it is desirable to perform experiments under *single* collision conditions.

Unfortunately, as in the field of target Auger spectroscopy, the projectile Auger lines are so numerous that difficulties occur with respect to line blending. This is primarily due to the fact that lines of various charge of the projectile contribute to the Auger spectra. These problems can partially be avoided by using light atoms such as Li or Be studied in detail by Rødbro et al. [57].

In principle, the problems of line blending in the Auger spectra may be reduced using electron-ion coincidence techniques. In coincidence experiments reported by Thomson et al. [228], Haggmann et al. [229], Schumann et al. [211] and Suter et al. [230] the charge state of the projectile is determined after the Auger electron is emitted. Unfortunately, the correlation between the charge state during Auger decay and that of the ion subsequently analyzed is not always unique because of the possibility of multiple subsequent Auger transitions. Also, in coincidence experiments problems arise with respect to limited statistics. With the coincidence techniques available to date, it appears difficult to achieve the counting rates required in the field of high-resolution electron spectroscopy.

To reduce the line blending for complex systems, it is useful to limit the number of charge states of the projectile. This may be achieved using the method of electron capture [59]. Before the collision, the projectile is prepared in high charge states including metastable states, so that vacancies occur in inner shells. Then, during the collision, electrons are captured in outer shells and autoionizing states are formed. Thus, He- or Li-like configurations have been studied [59]. It is noted however, that the selective electron capture is not so well suited for many electron systems.

Another method to obtain Auger spectra for a specific projectile charge state is achieved by using light target atoms as shown by Itoh et al. [61]. Light particles have the ability to act as a “needle” in selectively ionizing or exciting the inner shell without disturbing the outer shell. Needle ionization may be considered as an example of the more general concept of *ion surgery* where one or, at most, two electrons are ionized, or captured in the projectile ion without affecting its other electrons. In the *ion-surgery* picture the projectile ion is not considered to be a simple Coulomb point source but rather a structured particle whose properties can be investigated by the action of the light incident target atom.

Hence, the *needle ionization* preserves the incident outer shell charge state during the collision and the population of higher-lying Rydberg states is minimized. However, the method of *needle ionization* has the disadvantage that it requires light target atoms (H_2 or He) which limit the cross section for Auger electron production.

The ability of light particles to act like a needle is a well-known phenomenon in the field of target Auger spectroscopy, e.g. see the H^+ impact data in fig. 16. However, the method of target spectroscopy allows the study of few-hole systems only, when light-incident particles are used in the experiment. Contrary to that, projectile Auger spectroscopy has access to a wider range of electronic configurations, since the charge state of the incident ion may be varied. Hence, *needle ionization* allows the study of Auger electrons from various selected charge states of the projectile [61].

It is important to note that the methods of needle ionization and selective electron capture are

applicable in rather different energy ranges. Electron capture is important when the incident velocities are about equal to the velocity of the electrons in the outer-shell orbit of interest. Alternatively, for needle ionization the incident velocity is required to be significantly larger than that of the outer-shell electrons.

5.2. Kinematic effects

Since kinematic effects are of particular importance for projectile Auger electrons, some of their characteristic properties shall be discussed. As noted in section 3, two types of kinematic effects are relevant for the Auger lines. First, there are kinematic broadening effects which originate primarily from instrumental deficiencies. It is an essential condition for the applicability of the projectile Auger spectroscopy that the broadening effects are significantly reduced. The second type of kinematic effects originates from the (Galilei) transformation from the projectile frame to the laboratory frame of reference. It will be shown that these effects may favorably be used in the studies of projectile Auger electrons [231].

5.2.1. Line-broadening effects

The techniques to avoid the broadening effects on the projectile Auger electrons measured at non-zero observation angles are not straightforward. Both the azimuthal broadening ΔB_ϕ (eq. (3.2.9)) and the polar broadenings ΔB_θ (eq. (3.2.11)) are important for the projectile electrons. In particular, the influence of polar broadening effect is critical so that care is to be taken to keep the defining slits of the electron analyzer sufficiently small.

Fortunately, the azimuthal and polar broadening effects are important for different projectile energy ranges. It is recalled that ΔB_ϕ and ΔB_θ dominate at low and high incident energies, respectively. Hence, there is an intermediate energy range where high-resolution measurements of projectile Auger electrons are favorable. Close inspection of ΔB_ϕ and ΔB_θ show that the optimum intermediate energy refers to an incident velocity roughly equal to the velocity of the inner-shell electron under consideration. At this incident energy, also the maximum cross section for excitation of the inner-shell electrons is achieved. Taking K-shell Auger electrons as an example it is noted that the optimum energy ranges from about 200 keV to 20 MeV when the projectile nuclear charges increase from 3 to 10.

An effective method to reduce significantly the broadening effects for the projectile is to measure the electrons under extreme forward angles. Both the azimuthal and polar broadenings minimize at small electron observation angles (section 3). This has been demonstrated by Rødbro et al. [57] and Bisgaard et al. [232] using electron observation angles of a few degrees. Figure 38 compares Auger spectra from 250-keV $\text{Li}^+ + \text{He}$ collisions measured at 60° and 5° [232]. The data clearly show the effect of reduced line broadening at forward observation angles.

At the observation angle of 0° , the broadening effects reach their minimum. In fact, the first-order expressions (3.2.9) and (3.2.11) vanish for 0° so that the broadening is determined by the second-order effect [61, 233]. For example, with the analyzer acceptance angle of 0.5° , the polar broadening is reduced by about *two* orders of magnitude at 0° (section 3). Hence, the method of zero-degree Auger spectroscopy is of great potentiality for high-resolution studies of projectile electrons.

Measurements of autoionization and Auger electrons under 0° have been performed by Lucas and Harrison [60], Suter et al. [230, 234], Anderson et al. [235] and Kvale et al. [236]. Itoh et al. [61] have shown that projectile Auger electrons can be studied under conditions of high resolution at incident energies as large as 100 MeV.

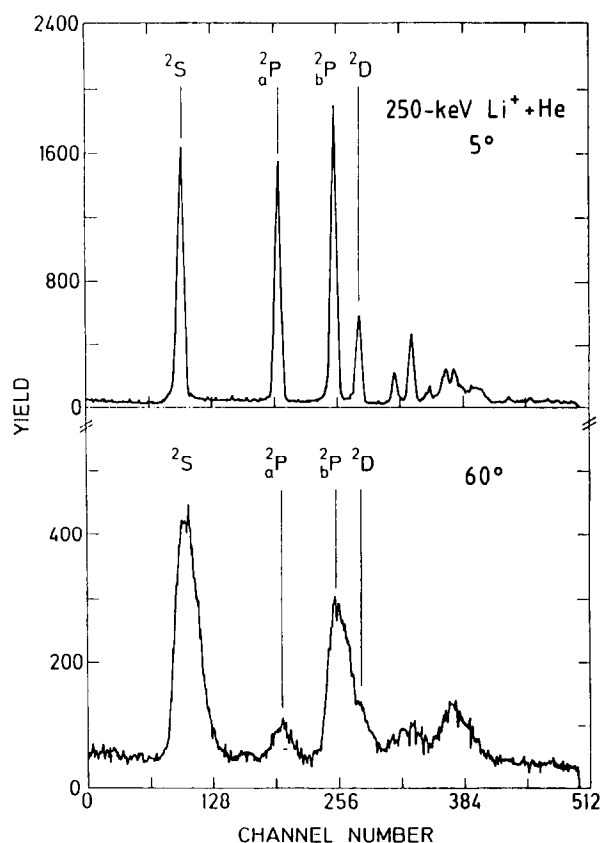


Fig. 38. Lithium-Auger spectra from 250-keV $\text{Li}^+ + \text{He}$ collisions. Electron observation angles are 5° and 60° as indicated. From Bisgaard et al. [232].

5.2.2. Frame transformation effects

The frame transformation effects, which change the position, width and height of an Auger line are denoted as shifting, stretching and enhancing, respectively (section 3). These effects are most significant for the electron observation angle of 0° . As an example, fig. 39 shows projectile electron spectra observed at 0° from collisions of 300-keV He^+ on He [231]. The data observed in the laboratory (LAB) system are transformed back into the projectile rest frame (PRO).

It is seen that the frame transformation influences strongly the position, width and height of the spectral lines. The shifting factor ε/ε' is about equal to 5. (As in section 3, ε and ε' denote the electron energy in the laboratory and projectile rest frame, respectively.) The stretching factor $\Delta\varepsilon/\Delta\varepsilon'$ is equal to 2.3. The line maxima are enhanced by the same factor. This follows from the fact that the stretching factor as well as the enhancement factor are (nearly) equal to the square root of the shifting factor, see eqs. (3.2.3) and (3.2.6). Hence, it follows the simple rule that the enhancement of the line integral (i.e. height times width) is of the same magnitude as the shifting factor.

The frame transformation effects may advantageously be applied in the measurements of the Auger electrons. For instance, the emitter rest frame energies of certain autoionization lines are so small that instrumental problems arise with the detection of the corresponding electrons. In this case, the shifting effect may be utilized to locate the lines into an energy range which is readily accessible to the electron spectrometers.

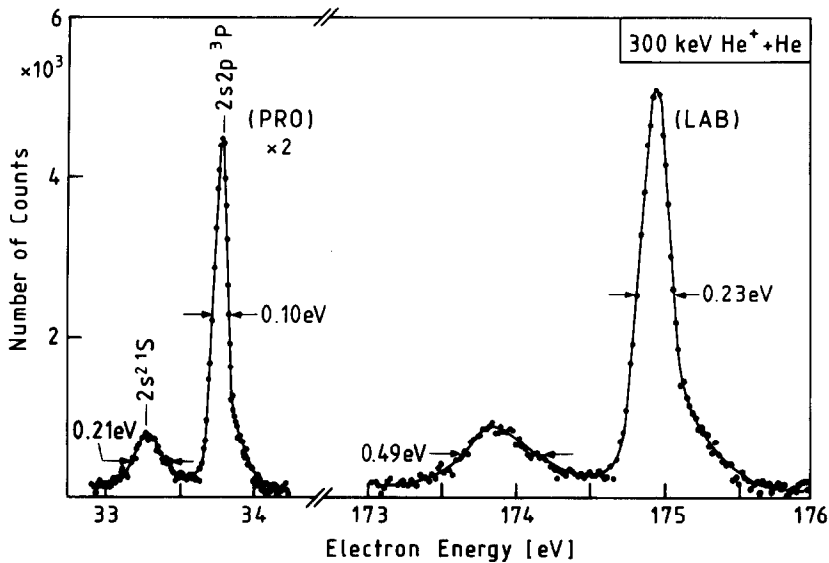


Fig. 39. Projectile autoionization lines from collisions of 300-keV He^+ on He observed in the laboratory (LAB) rest frame and transformed into the projectile (PRO) rest frame. From Stolterfoht et al. [231].

Similarly, the stretching effect may be applied in measurements which require extremely high resolution, e.g. in measurements of the natural line widths. Light atoms such as He have Auger line widths of about 0.1 eV (fig. 3). A resolution of this magnitude is difficult to achieve at ion accelerators. Hence, it is useful to stretch the line kinematically so that it becomes comparable with the spectrometer resolution. In fig. 39 the spectrometer resolution amounts to 0.23 eV as seen from the width of the $2s2p\ ^3P$ state in the LAB system. This state has a negligible natural line width so that its observed width represents the instrumental resolution. With the resolution of 0.23 eV it would be difficult to detect the natural line width of the $2s^2\ ^1S$ state of 0.14 eV [4]. However, the instrumental resolution is sufficient to observe the *stretched* natural line width of 0.32 eV. It is seen that the instrumental width and the stretched natural line width add up (about in quadrature) to 0.49 eV in the LAB system.

It should be pointed out that the stretching effect is of advantage only if the absolute value $\Delta\varepsilon$ of the resolution is about constant with varying electron energy ε . Often the relative resolution $\Delta\varepsilon/\varepsilon$ is constant in the experiments. Then, the stretching effect results in a loss of the effective resolution [61]. It is readily seen that the relative energy width is enhanced by the stretching factor $(\varepsilon/\varepsilon')^{1/2}$.

In fast collisions the (Galilei) frame transformation produces also a doubling of the Auger lines (section 3). The doubling effect is demonstrated in fig. 40 where results for 79.41-MeV $\text{Ar}^{5+} + \text{He}$ collisions are depicted [237]. Ar-L shell electrons ejected with about 100 eV at 180° and 0° in the projectile rest frame are shifted near the energies of 550 eV and 2200 eV, respectively. It is noted that the low (L) energy spectrum is the reflected image of the high (H) energy spectrum. After the laboratory-to-projectile rest frame transformation, the two spectra are found to be identical within the statistical errors [61], see also fig. 41.

The comparison of the transformed spectra allows the determination of the reduced projectile energy t_1 as well as the Auger electron energy ε' with relatively high accuracy. For 0° observation angle, eq. (3.2.1b) yields the relations

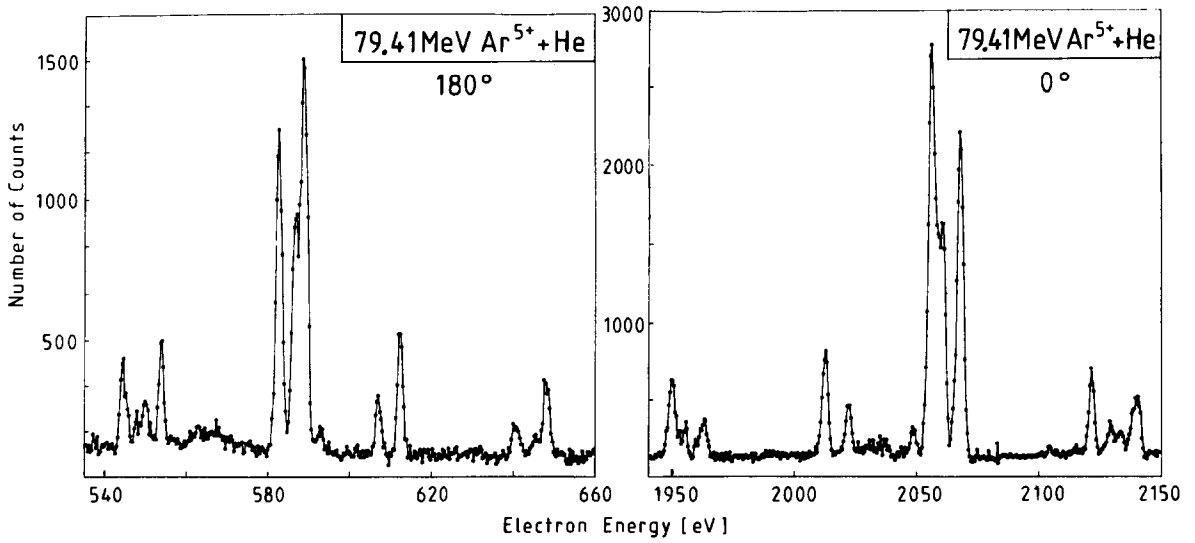


Fig. 40. Argon-L-Auger spectra from collisions of 79.41-MeV $^{40}\text{Ar}^{5+}$ on He observed in the low (L) energy range and the high (H) energy range of the laboratory frame of reference. From Schneider et al. [237].

$$\varepsilon_H = (t_1^{1/2} + \varepsilon'^{1/2})^2 \quad (5.2.1a)$$

$$\varepsilon_L = (t_1^{1/2} - \varepsilon'^{1/2})^2 \quad (5.2.1b)$$

where ε_L and ε_H are energies of corresponding Auger lines in the low and high energy range, respectively. The two eqs. (5.2.1) allow for the determination of the two unknown quantities t_1 and ε' . In practice, one adjusts the projectile energy until the corresponding Auger lines coincide in positions as shown in fig. 41. The results suggest that the adjustment procedure yields the projectile energy with the accuracy of $\sim 10^{-4}$ in the present case.

In addition, rather accurate Auger energies may be obtained. In the field of Auger spectroscopy, principle problems arise from the contact potentials which produce uncertainties in the absolute energy of 1–2 eV. It is important to note that for projectile Auger electrons, whose energies are shifted kinematically to higher values, the contact potentials lose relative importance. When the energies are transformed back to the projectile rest frame, the uncertainty by the contact potentials is reduced by the factor $\sim (\varepsilon'/t_1)^{1/2}$ (eq. (3.2.3)). Hence, for fast collisions ($t_1 \gg \varepsilon'$), a significant reduction of the uncertainty due to contact potentials may be achieved [61].

5.3. K-Auger transitions

Most experiments concerning projectile Auger electrons have been performed to study K-Auger spectra. A great number of these experiments have been devoted to projectile ions which are stripped to few electron systems. Thus, projectile K-Auger spectra have been measured predominantly for two to five electron ions. Elements with atomic number as high as 18 have been studied.

The early high-resolution experiments of projectile Auger electrons have been made using the method of beam-foil spectroscopy [55, 56], i.e. the electrons were observed delayed in time. These measurements take advantage of the fact that the Auger electrons from promptly decaying states do not

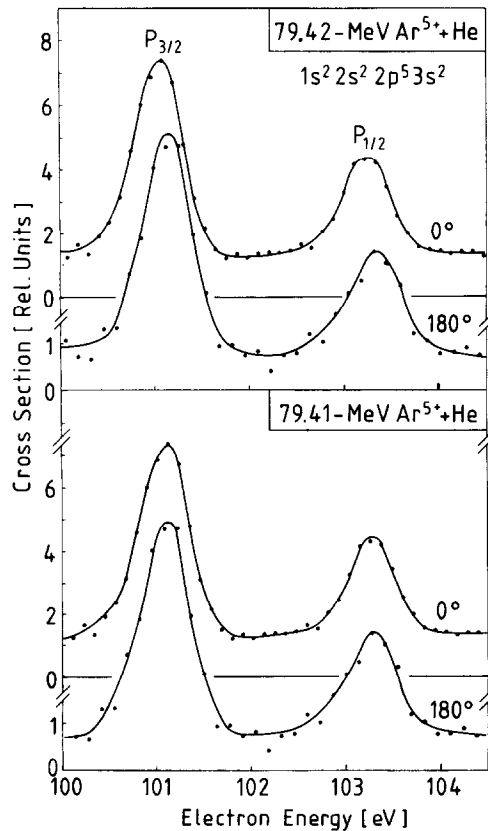


Fig. 41. Argon-L-Auger spectra from collisions of Ar^{5+} on He transformed from the low (L) energy range and the high (H) energy range of the laboratory rest frame (fig. 40) into the projectile rest frame. Projectile energies of 79.42 MeV and 79.41 MeV are adopted as indicated.

contribute to the measured electron spectrum. Hence, the time delay measurements yield relatively simple Auger spectra where individual lines are well separated. Thus, detailed information can be obtained about the life time of the corresponding metastable states.

Since these early experiments the interest in the states of highly excited projectile ions has increased significantly and prompt Auger electrons have also been studied in detail [57, 58]. Generally, the prompt Auger spectra are of great complexity and their analysis requires a considerable effort. Methods to analyze the projectile Auger spectra are presented in the following discussion. In the next section 5.3.1, the attention is focused on the analysis of the prompt spectra. Section 5.3.2 is devoted to metastable states.

5.3.1. Analysis of prompt electrons

Schneider et al. [58], Johnson et al. [238], Groeneveld et al. [239] and Bruch et al. [240] reported on measurements of prompt Auger electrons from fast projectiles. Both foil and gas targets were applied in the experiments. Figure 42 shows typical C-K-Auger spectra measured by Schneider et al. [58]. In the Auger spectra, the line at the lowest energy is due to the Li-like states $1s2s^2\ ^2S$ and $1s2s2p\ ^4P$. The latter state is metastable and it is preferentially observed in the time delayed spectrum [56]. Apart from this, the spectra consist of many overlapping lines which were suggested to be due to three- and four-electron configurations of the emitting projectile ion.

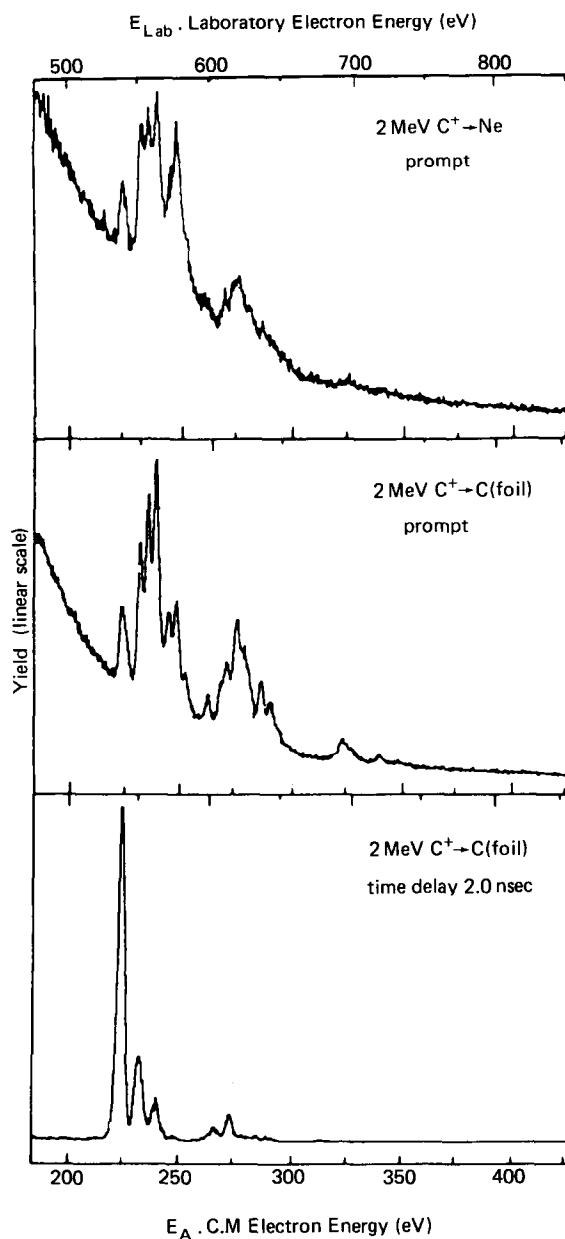


Fig. 42. K-Auger spectra of carbon resulting from 2-MeV C impact on Ne and thin C foils. The electron energy refers to the projectile frame. The bottom spectrum was measured downstream from the exciter foil corresponding to 20 ns delay time. From Schneider et al. [58].

An interesting aspect of the work by Schneider et al. [58] is that the Auger spectra obtained with both gaseous and solid targets are nearly equal (fig. 42). Similar observations have been made by Bruch et al. [241] and Rossner et al. [242]. Obviously, after several collisions in the foil, the outer-shell configuration of a projectile is very similar to that produced in a single violent collision where the target atom passes through the K-shell of the projectile. It appears in the two cases that the formation of the projectile charge state is determined by general statistical laws which are independent of the specific

processes involved in the collisions. Similar inferences have been obtained within the framework of the information-theoretical approach by Åberg and Goscinski [200, 201].

A systematic study of the carbon and oxygen projectile Auger spectra have been made by Schneider et al. [243–245] and Bruch et al. [241]. Experimental results for Auger transition energies of oxygen [241, 244] are given in table 7. In the experiments, various parameters such as the incident energy, the projectile charge state, and the atomic number of the target atoms were changed to verify their influence on the measured Auger spectra. Results by Bruch et al. [241] are depicted in fig. 43 which shows oxygen-Auger spectra for various charge states of the incident projectile. In the experiments particular attention has been devoted to the creation of double K vacancy states which can be seen near 520 eV in the Auger spectra (fig. 43).

With increase of the beam velocity, Auger lines at lower energies were found to be preferentially excited. This is explained by the increase of multiple outer-shell ionization as discussed in detail for target Auger spectra in section 4.2. As expected, the polar line broadening effect was found to increase as the incident energy increases. Similarly, as heavier target atoms are used, the projectile scattering angle increases giving rise to an increase of the azimuthal broadening effect.

Apart from this, the variation of the target atom (He, Ne, Ar and Kr) as well as the projectile charge state appear to have small effects on the overall shape of the Auger spectra (fig. 43). This is a further indication for the statistical nature of violent collisions between heavy particles where the memory on

Table 7
Experimental energies (in eV) of K-LL Auger transitions in Li- and Be-like systems

Final ionic state	Initial state	Li (a)	Be (b)	B (c)	C (d)	O (e)	Ne (f)	Line ass. (g)
<u>Li-like</u>								
$2s^2\ ^1S$	$1s2s^2\ ^2S$	50.97	96.1	154.9	227.2	412.6*	652.7*	A1
	$1s2s2p\ ^4P$	52.04	97.6	156.8*	229.6*	416.0	656.5	A2
	$1s(2s2p\ ^3P)^2P$	53.52*	100.6	161.2	235.5	425	668.6	A3
	$1s(2s2p\ ^1P)^2P$	55.01*	102.8*	164.1	238.9	430	673.4	–
	$1s2p^2\ ^2D$	55.67	104.2	166.3	242.2	–	682 [†]	–
<u>Be-like</u>								
$1s^22p\ ^2P$	$1s2s^22p\ ^3P$	–	101.0	–	235.4	424	667.3	B3
	$\ ^1P$	–	102.1	162.9	238.2	428.5	673.8	A4, B5
$1s^22s\ ^2S$	$1s2s^22p\ ^3P$	–	104.9	167.3	243.4	–	683.2	B6
$1s^22p\ ^2P$	$1s2s2p^2\ ^3P$	–	102.2	162.9	237.1	426.2	670.3	B4
	$\ ^3P$	–	–	–	–	–	684.0	A5
$1s^22s\ ^2S$	$1s2s2p^2\ ^5P$	–	106.1	169.0	245.1	438.2	686.2 ^{††}	B7
	$\ ^3D$	–	–	174.5	252.6	449	700.5	A6, B10

* used for energy calibrations.

a) Rødbro et al. [253] using results from Ederer et al. [177] for calibration.

b) Rødbro et al. [253] using results from Kennedy and Carroll [254] for calibration.

c) Rødbro et al. [253] using results from Chung and Bruch [255] for calibration.

d) Rødbro et al. [253] using results from Bruch et al. [256] for calibration.

e) Bruch et al. [241] and Schneider et al. [244] using calculations with the method by Schwarz and Chang [246] for calibration.

f) Itoh et al. [268] using theoretical results from Schumann et al. [211] for calibration.

g) The line assignment refers to fig 47.

[†] obtained from fig. 4 in ref. [268].

^{††} misprinted in ref. [268].

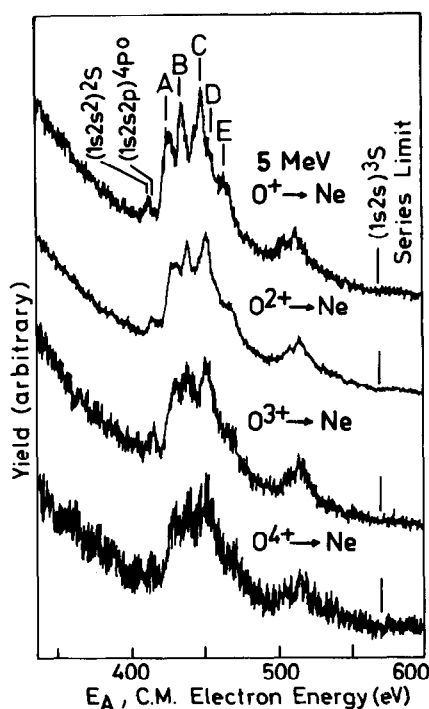


Fig. 43. K-Auger spectra of oxygen produced by 5-MeV O^+ , O^{2+} , O^{3+} and O^{4+} impact on Ne. Observation angle is 23.7° . The electron energy refers to the projectile frame. From Bruch et al. [241].

incident properties such as the charge state are lost. However, as shown further below, in collisions with light target atoms (e.g. H_2 or He) the incident charge state influences strongly the projectile Auger spectra.

Schneider et al. [243, 245] and Bruch et al. [241] performed extensive multiconfiguration calculations to further analyze the projectile Auger spectra. The calculations are based on the generalized Brillouin theorem (GBT) method used by Schwarz and Chang [246]. Various results for Li- and Be-like states are given in table 8. In general, the theoretical results are found to be in good agreement with the earlier calculations by Safronova and Kharitonova [247], Feldman and Cohen [248], Høloien and Cohen [248], Høloien and Geltman [249], Goldsmith [250] and Lipski et al. [251]. The theoretical analysis made possible the identification of various unknown lines in the Auger spectra. However it was also anticipated that the origin of many spectral structures remained undetermined due to problems caused by overlapping lines.

Further advances to analyze the K-Auger lines from few-electron systems have been made by Rødbro et al. [57, 252, 253]. To reduce the problems caused by the complexity of the Auger spectra, Rødbro et al. [253] used the simplest atomic species available with an inner 1s electron i.e. Li, Be, B and C. With regard to the line-broadening effects, an optimum incident energy of a few hundreds of keV was chosen in the experiments as pointed out in the foregoing section. Furthermore, the electrons were observed at rather small emission angles as previously proposed by Bruch et al. [241]. Hence, significant improvements were achieved with respect to the spectral resolution. Figure 44 shows a typical spectrum of Auger electrons from Be projectiles with a single K vacancy. Similar results have been obtained for hypersatellite spectra associated with double K vacancy states.

Table 8

Calculated energies (in eV) of K-LL-Auger transitions in Li- and Be-like systems. The quantity ΔE_{2s-2p} denotes the energy difference between the final ionic states $1s^2 2s^2 S$ and $1s^2 2p^2 P$. The branching ratio refer to the decay to the same final ionic states of Ne

Final ionic state	Initial state	C (a)	O (b)	Ne (c)	Ne branching ratio (d)
<u>Li-like</u>					
$2s^2 \ ^1S$	$1s2s^2 \ ^2S$	227.5	412.6	652.7	-
	$1s2s2p \ ^4P$	229.9	416.0	656.3	-
	$1s(2s2p \ ^3P)^2P$	235.9	424.7	668.9	-
	$1s2p^2 \ ^4P$	238.3 ⁺	428.3 ⁺	673.5	-
	$1s(2s2p \ ^1P)^2P$	239.3	429.5	675.6	-
	$1s2p^2 \ ^2D$	242.3	434.4	681.8	-
<u>Be-like</u>					
$1s^2 2p^2 P$	$1s2s^2 2p^3 P$	235.9	424.2	667.8	0.57
	1P	238.5	428.5	674.5	1.00
$1s^2 2s^2 S$	$1s2s^2 2p^3 P$	243.6	436.2	683.8	0.43
	1P	246.5	440.5	690.5	0.0035
$1s^2 2p^2 P$	$1s2s2p^2 \ ^3P$	237.5	426.7	669.9	0.16
	3P	243.6	436.4	684.7	1.00
	3D	244.3	437.0	684.9	0.12
	3S	248.2	442.5	696.3	0.25
	1D	248.3	443.4	696.6	0.51
	3P	249.9	444.9	695.8	1.00
	1P	-	-	701.4	1.00
	1S	252.2	449.3	703.4	0.72
$1s^2 2s^2 S$	$1s2s2p^2 \ ^5P$	245.5	438.7	686.0	0.84
	3P	-	448.4	700.8	0
	3D	252.3	449.0	701.2	0.88
	3S	256.2	454.5	708.3	0.75
ΔE_{2s-2p}		8.0	12.0	16.0	-

(a) Schneider et al. [243] using the method by Schwarz and Chang [246]. The present data are generally 0.3 eV lower than those by Bruch et al. [256] whose results have been applied to calibrate the experimental results in table 7.

(b) Bruch et al. [241] using the method by Schwarz and Chang [246].

(c) Schumann et al. [211] and Mann et al. [212] using the DF code by Desclaux [86].

(d) The data are derived from the transition rates given by Chen and Craseman [144].

⁺ From Chen et al. [149].

Rødbrø et al. [253] made a specific effort to investigate various instrumental effects which influence the energy of the measured electrons. Energy calibrations of the Li and Be were made using results from high-precision photoabsorption measurements [177, 254]. Hence, accurate transition energies were determined for a large number of single and double core excited states. In addition, a detailed comparison was made with previous experimental and theoretical results. Most of the experimental results [253] are summarized in table 7.

Recently, the boron and carbon data obtained by Rødbrø et al. [253] were reanalyzed by means of

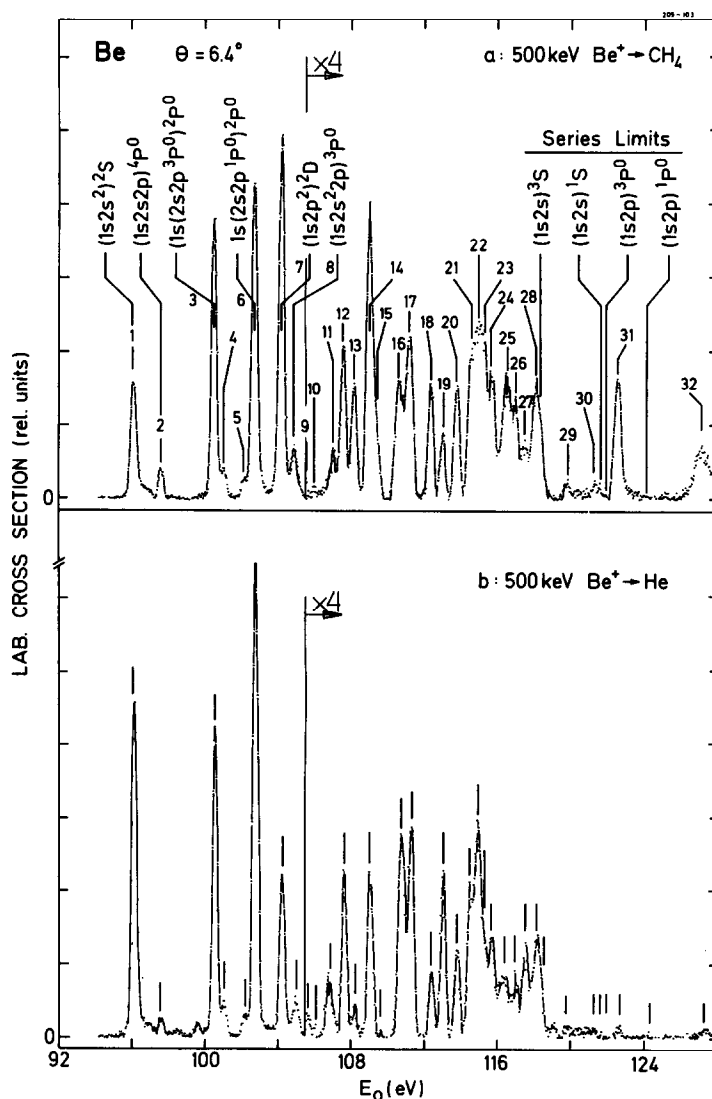


Fig. 44. K-Auger spectra of beryllium resulting from 500-keV Be⁺ impact on CH₄ (a) and He (b). Observation angle is 6.4°. The electron energy refers to the projectile frame. From Rødbro et al. [253] where also the key to the line assignment is given.

accurate calculations of Chung and Bruch [255] and Bruch et al. [256]. The calculations are based on the saddle-point method developed by Chung [257]. Further results for boron have been obtained by Luken and Leonhard [258] using the unrestricted Hartree-Fock approach [259]. The theoretical results [255, 256] were used to improve the energy calibration of the boron and carbon data for which no photoabsorption measurements exist. However, it should be noted that the previous energy calibrations [253] are correct to within 0.15 eV.

For He- and Li-like states Rødbro et al. [253] collected all data available for elements with atomic numbers as high as 16. These data were used to establish semiempirical scaling rules suitable to determine the Auger transition energies for isoelectronic sequences. The (initial) state energy is expressed in terms of a power series of the inverse atomic number, i.e. $E = Z^2 \sum_n E_n Z^{-n}$ which may be

Table 9
Semiempirical K–LL transition energies (in eV) for He-like isoelectronic sequence [253].
The data are obtained from eq. (5.3.1) using the coefficients given in the appendix A2

Initial state	Li	Be	B	C	O	F	Ne
$2s^2\ ^1S$	70.56	121.52	186.11	264.34	461.72	580.87	713.66
$2s2p\ ^3P$	71.36	122.58	187.39	265.80	463.43	582.64	715.46
$2p^2\ ^1D$	74.22	126.69	192.79	272.50	472.80	593.39	727.59
$2s2p\ ^1P$	74.67	127.39	193.72	273.64	474.28	595.00	729.32

evaluated within the framework of perturbation theory. Isoelectronic sequences have been studied by several authors, e.g. Chan and Stewart [260], Wiese and Weiss [261], Drake and Dalgarno [262], and Doyle et al. [263].

For practical purposes it is sufficient to retain the first three terms of the series, i.e.

$$E = E_0 Z^2 + E_1 Z + E_2 . \quad (5.3.1)$$

The expansion coefficient E_0 , E_1 and E_2 determined by Rødbro et al. [253] are given in the appendix A2. It should be kept in mind that the power series expansion does not account for relativistic effects so that its application is limited to light atoms. Semiempirical results from eq. (5.3.1) for the He-like states of light elements are given in table 9.

In spite of the effort to improve the instrumental resolution, Rødbro et al. [253] encountered serious difficulties in attempting to analyze the Auger spectra for boron and carbon. Heavier elements involve a copious amount of Auger transitions. For example, 132 transitions exist for Li-, Be- and B-like configurations from which 104 transitions are associated with the B-like system alone. To obtain more than only qualitative results for the heavier elements, specific care is needed to excite a limited number of lines in the Auger spectra.

Methods to restrict the number of Auger lines in a spectrum are (i) time delay measurements, (ii) electron–ion coincidence measurements, (iii) needle ionization, and (iv) electron capture. Each method has certain advantages and restrictions as pointed out in the previous section. Electron capture and needle ionization will be considered in more detail in the following discussion.

Studies of projectile Auger electrons by means of selective electron capture have been performed by Newcomb et al. [59] and Dillingham et al. [264]. The experiments have been made using carbon, nitrogen, oxygen and fluorine projectiles with zero, one and two electrons. The incident energy was chosen to be about half an MeV per nucleon which is adequate to achieve a significant probability for electron capture. Transfers of electrons are required to produce Auger states for incident bare and one-electron ions.

For bare projectiles, it is necessary to capture *two* electrons in excited states. This is seen from fig. 45 showing results for 0.67-MeV F^{9+} on Ar by Dillingham et al. [264]. As expected the figure exhibits hypersatellites which are attributed to configurations $2lnl'$ with $n \geq 2$.

For incident one-electron ions, Dillingham et al. [264] found lines due to Li-like configurations only. This shows that *double* electron capture into excited states is the leading mechanism for producing the Auger states in the collision systems studied. Hence, transfer excitation collisions [265, 266] where a single electron is captured and the K electron of the projectile is excited simultaneously produces a negligible contribution to Auger electron production in the collision systems considered here.

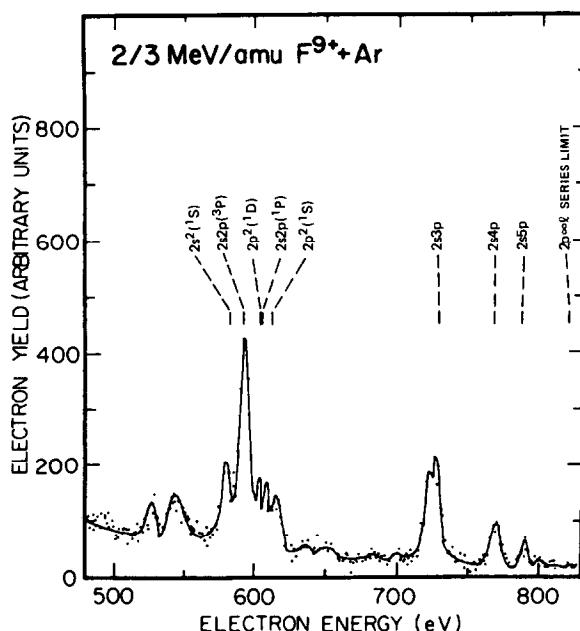


Fig. 45. K-Auger spectrum of fluorine produced by 0.67-MeV/u F^{9+} impact on Ar. The electron energy refers to the projectile rest frame. The spectrum shows hypersatellites with the initial states $2ln'$. From Dillingham et al. [264].

Single electron capture is responsible for the formation of Auger states in the case of incident two-electron ions. Similarly as in the case of one-electron ions, K-shell excitation of the projectile is a negligible mechanism. Rather, the observed Li-like states are formed by electron capture into the metastable state $1s2s^3S$. This process was studied extensively for slow recoil ions in section 4.5.2. Particle accelerators produce a significant fraction of metastable particles in the ion beam as will be discussed further below. Newcomb et al. [59] and Dillingham et al. [264] anticipated a fraction of 5% to 25% of metastables in the F^{7+} beam in accordance with the work by Terasawa et al. [267].

The studies by Newcomb et al. [59] and Dillingham et al. [264] are primarily devoted to collision mechanisms rather than to spectroscopic details. The energy resolution is often insufficient to separate lines attributed to individual initial states, e.g. $1s2s^2S$ and $1s2s2p^4P$. Emphasis is given to the analysis of line groups associated with a certain principal quantum number n . Absolute cross sections were determined for single and double electron transfer into excited states with $n = 2$ to 5 and higher. It is remarkable that (except for He) the cross sections for double electron capture are found to be of the same order of magnitude ($\sim 10^{-17} \text{ cm}^2$) as the corresponding cross sections for single capture. This shows that capture into excited states is an important process for the ion velocities studied [59, 264].

The method of needle ionization has been applied by Itoh et al. [61, 266, 268]. The principles of needle ionization are outlined in fig. 46 where features of target and projectile spectroscopy are compared. The figure emphasizes that in violent heavy ion-atom collisions, various charge states are randomly produced. This is a principle problem in the field of target Auger spectroscopy where the recoil atom is multiply ionized in a single collision. To limit the number of states, the target atom has to be almost totally stripped so that only few-electron configurations can be studied in detail.

The method of needle ionization provides access to a wider range of configurations in addition to the advantage that the number of states is limited. This is achieved by using light target particles which do not disturb the outer shell of the projectile during the inner-shell ionization or excitation event. The idea

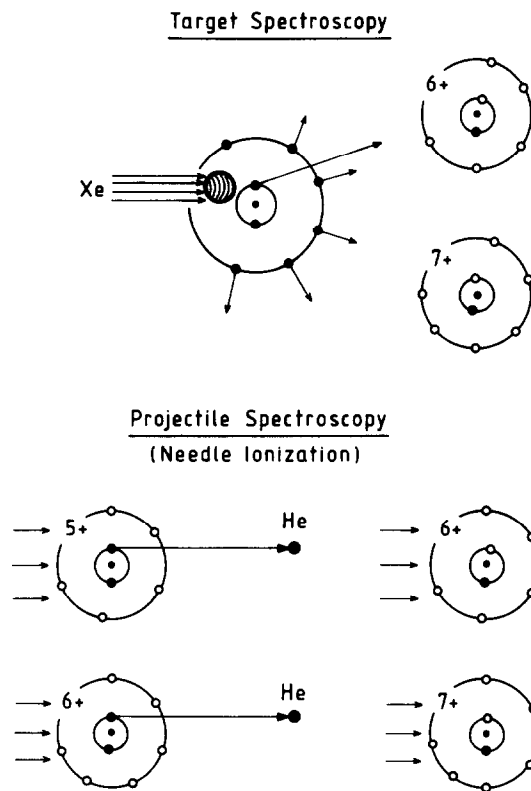


Fig. 46. Schematic diagram demonstrating the main features of target and projectile spectroscopy. The projectile is ionized by light target atoms to conserve the outer-shell state of the projectile. This technique is referred to as needle ionization. From Stolterfoht et al. [231].

is to perform a sudden removal of the inner-shell electron so that the outer shell may be considered as being frozen. Also, it is expected for highly ionized projectiles that shake-off probabilities are small.

It is obvious that needle ionization works best when fast projectiles are used. Hence, generally, the outer shell remains in its ground state and, therefore, the occupation of higher Rydberg states which give rise to cascade transitions are not expected to occur. Rather, it may be assumed that the ion encounters the collision in a metastable state, when the outer shell is *not* in its ground state configuration after the collision. Thus, direct information about possible metastable ions in the beam is obtained.

Neon-K-Auger spectra measured by Itoh et al. [268] for the collision systems 70- and 100-MeV $\text{Ne}^{q+} + \text{He}$ are shown in fig. 47. The data refer to the incident charge states $q = 4, 5$ and 6. The projectile spectra are compared with Ne-K target-Auger data [174] already discussed in section 4.2.1 (fig. 16). The target spectrum is a composition of all Auger lines from the projectile spectra shown. It is obvious that difficulties exist with the analysis of the complex target spectrum.

In fig. 47 the projectile spectra for incident Ne^{6+} , Ne^{5+} and Ne^{4+} are dominated by lines due to Li-, Be- and B-like states, respectively. An overview of the corresponding Auger transitions is given in fig. 48 [269]. The line assignments for the Ne^{6+} and Ne^{5+} spectra are indicated in table 7. In comparison with the analysis by Itoh et al. [268] a few lines were reassigned taking line intensity arguments into account. They are based on branching ratios (table 7) derived from transition rates by Chen and Crasemann [144]. For instance, the lines A4 and A5 are attributed to the Be-like states $1s2s^22p^1P$ and

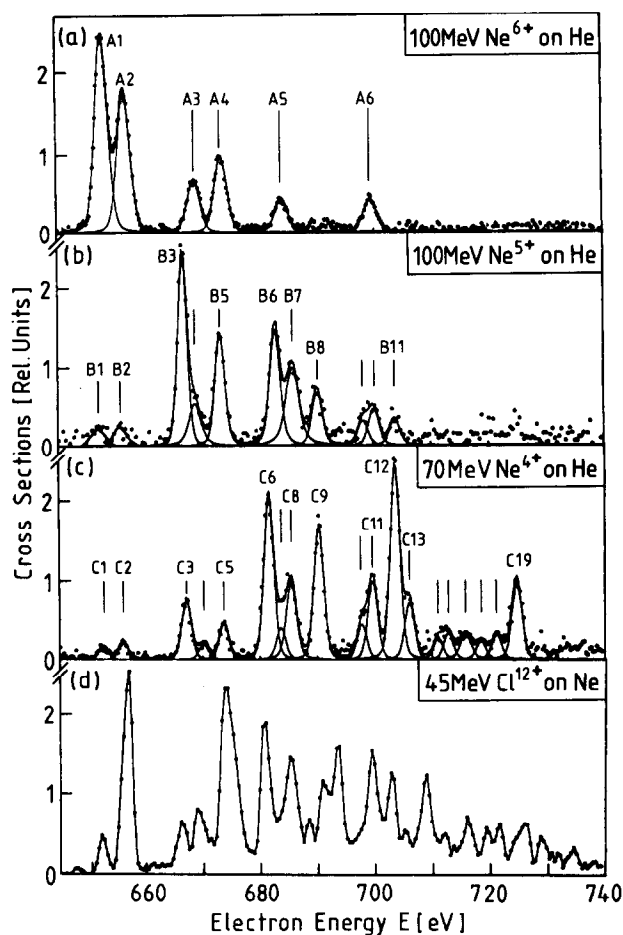


Fig. 47. K-Auger spectra of neon produced in collisions of Ne^{q+} on He. The data are obtained with 100-MeV Ne^{6+} (a), 100-MeV Ne^{5+} (b) and 70-MeV Ne^{4+} (c). Electron observation angle is 0° . The electron energy refers to the projectile rest frame. In (d) the Ne target spectrum measured by Schneider et al. [174] is shown for comparison. From Itoh et al. [268].

$1s2s2p^2\ ^3P$, respectively. The lines B8, B9 and B11 are very likely due to boron-like configurations.

In fig. 47 the prominent lines are produced by the removal of the projectile $1s$ electron into the continuum. Hence, the most probable charge state of the emitting ion is one unit higher than the incident charge state. However, in addition, there are lines produced by excitation of the projectile $1s$ electron to a bound state. Hence, each spectrum implies a certain contribution from the charge state equal to the incident one. For instance, in the Ne^{6+} spectrum the intensity fraction of the Be-like lines A4, A5 and A6 amounts to about 30%. Other charge states produced e.g. by electron capture can be completely neglected. However, double ionization plays a certain role for the Ne^{4+} spectrum [268]. There, the method of needle ionization which assumes the removal of a single electron, reaches its limits.

Finally in this section, a comparison is made between the experimental and theoretical transition energies given in tables 7 and 8. The number of experimental studies of prompt Auger electrons is still limited so that only existing data are presented (except for Li). However, the theoretical studies are more numerous so that the choice of the data presented is somewhat arbitrary. The theoretical data

enough so that their decay length reach some centimeters or meters and, hence, their life times may be studied by means of the beam-foil spectroscopy method.

There are various types of metastable states involving quite different decay mechanisms:

Parity-forbidden transitions. This type of transition has an initial (final) state whose total parity differs from the parity of its orbital angular momentum and it has a final (initial) ionic state with zero orbital angular momentum. A typical example for this type of transition involves the initial even parity state $2p^2\ ^3P^e$. The decay to the final state $1s\epsilon p\ ^3P^o$ is not possible, since it has odd parity (table 3). The state actually decays through the breakdown of the *LS*-coupling scheme induced by spin-orbit interaction. It produces the mixing with other states of even angular momentum (S, D, etc.) so that the decay to final state of even parity becomes possible. In section 2.3 it is shown that the transition rate out of the metastable state is obtained from the transition rate of the admixed state weighted by the square of the mixing coefficient, see eq. (2.3.11).

Spin-forbidden transitions. This type of transition involves an initial and a final ionic state whose spins differ by more than $1/2$. Thus, in *LS*-coupling the ejected electron is not able to carry away the spin which is set free by the Auger transition. In general, the spin of the initial state is larger than that of the final ionic state, since the former involves one electron more. The Auger transitions associated with some high-spin states of few-electron neon ions are shown in fig. 48.

The Li-like system forms the metastable state $1s2s2p\ ^4P$ which has been discussed previously. The only possible nonradiative transition leads to the final state $1s^2\ ^1S$ whose spin differs from the initial state by $3/2$. Different decay modes are to be considered for the three levels $^4P_{1/2}$, $^4P_{3/2}$ and $^4P_{5/2}$ of the configuration $1s2s2p$. The first two levels mix with the corresponding doublet levels $^2P_{1/2}$ and $^2P_{3/2}$ of the same configuration. This mixing is caused by spin-orbit interaction similar as in the case of parity-forbidden transitions.

The $^4P_{5/2}$ level cannot mix with any other level of the same configuration. Hence, its decay becomes rather improbable. The decay proceeds via the magnetic spin-orbit or spin-spin interaction (table 3). These interactions involve two-body operators causing direct transitions to the $1s^2\ ^1S$ final state. It should be noted that the long-lived component $^4P_{5/2}$ of the $1s2s2p$ configuration is rather unique. The $^4P_{5/2}$ level of the configuration $1s2p^2$ mixes with the $^2D_{5/2}$ level of the same configuration by the spin-orbit interaction and, thus, it may decay more rapidly.

Other quasi-forbidden transitions. Apart from the metastable states whose decay is strongly suppressed by specific selection rules, there are states whose transition rates are more or less weakly reduced by specific effects. Examples for this type of state are the $1s2snl\ ^{2S+1}L$ states involving a Rydberg electron. The decay of these states is governed by the well-known n^{-3} law which may produce rather long lifetimes. The dependence of the life time on the angular momentum l is expected to be governed by an even higher power law.

In addition, the Pauli principle may influence the Auger transition rates. For instance, Li-like states $(1s2s\ ^1S)nl\ ^{2S+1}L$ and $(1s2s\ ^3S)nl\ ^{2S+1}L$ have rather different Auger decay rates as n increases. The first one may decay via the (direct) two-electron transition $2s \rightarrow 1s$ and $nl \rightarrow \epsilon l'$, whereas the second one can only decay via the rather improbable (exchange) transition $nl \rightarrow 1s$ and $2s \rightarrow \epsilon l'$. The life times of the states considered here, may cover the whole range between the approximate limits 10^{-9} to 10^{-15} s set by the metastable states and the promptly decaying states, respectively.

In the field of projectile Auger spectroscopy, spin-forbidden states have been studied predominantly. Early Auger spectroscopy experiments concerning high-spin states have been performed using the method of beam-foil spectroscopy. Donnally et al. [270], Sellin et al. [271] and Pegg et al. [272] reported on life-time measurements for the $1s2s2p\ ^4P$ state of oxygen and fluorine. In fig. 49 typical

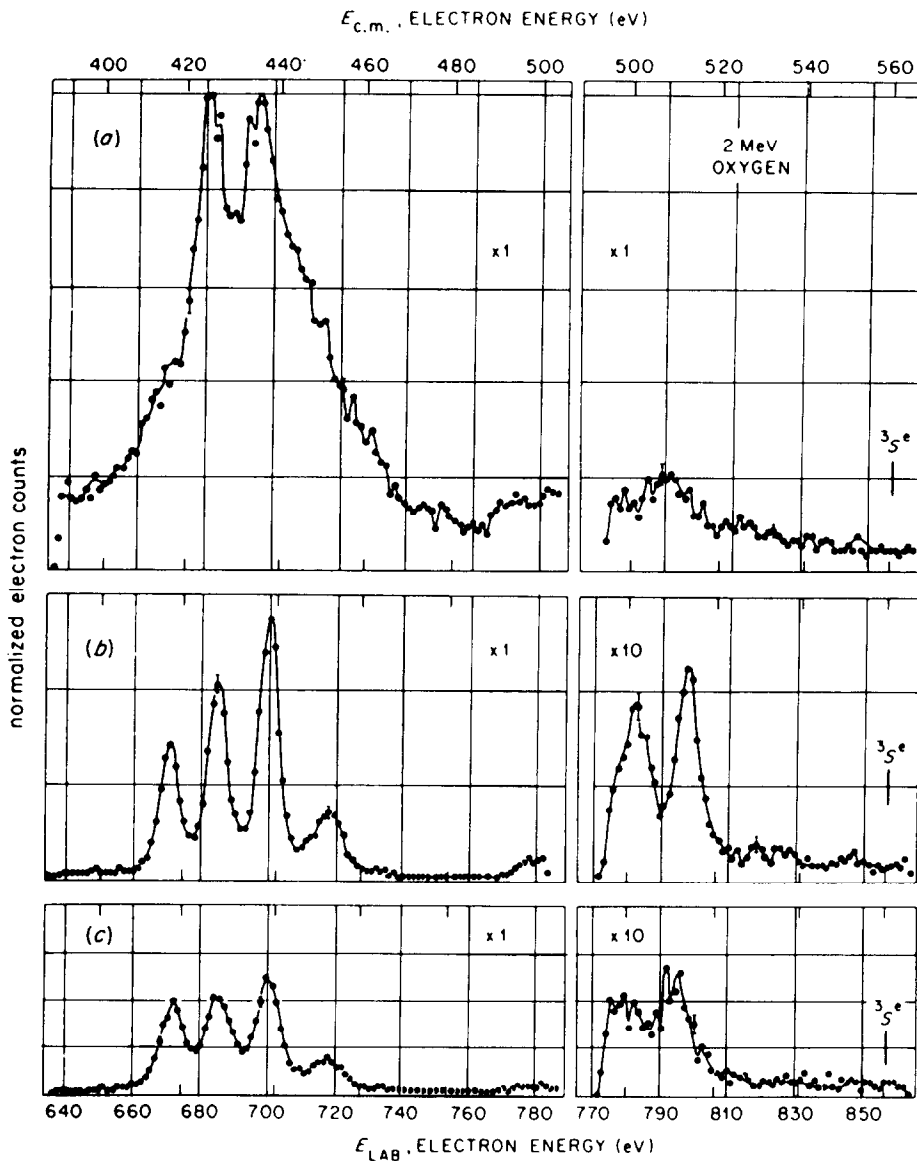


Fig. 49. Spectra of K-Auger electrons from 2-MeV foil excited oxygen. The electron energy refers to the laboratory frame. In (a) prompt spectra are given. In (b) and (c) the electrons are delayed by 0.7 and 1.0 ns, respectively. From Pegg et al. [272].

examples are given for delayed Auger spectra of oxygen measured by Pegg et al. [272]. The figure shows a prompt spectrum observed directly at the exciter foil and delayed spectra detected at different locations downstream from the exciter foil. It is seen that the prompt spectrum is only weakly structured whereas the delayed spectra exhibit separated lines. Hence, the different decays of the metastable states $1s2s2p^4P$, $1s2s2p^2^5P$, and possibly $1s2s2p^3^6S$ may be observed. In the high-energy part of the spectra lines due to configurations $1s2l3l'$ are visible.

Further life-time experiments were made by Sellin et al. [273] and Pegg et al. [274, 275] for chlorine and argon, by Pegg et al. [276] for sulfur, by Haselton et al. [277] for aluminum and silicon, and by

Table 10
Theoretical and experimental life times [in ns] for the $1s2s2p$ 4P states of light ions

Initial state	C	O	Ne	Al	S	Ar
$^4P_{1/2}$ theory	3.69 ^a	1.08 ^a	0.42 ^a	0.095 ^b	–	0.0057 ^b
$^4P_{1/2}$ expt.	–	2.0 ^d	0.40 ^c	–	–	–
$^4P_{3/2}$ theory	13.2 ^a	4.4 ^a	0.90 ^a	0.061 ^b	–	0.0021 ^b
$^4P_{3/2}$ expt.	–	8.0 ^d	1.6 ^c	–	–	–
$^4P_{5/2}$ theory	117 ^a	28.4 ^a	9.8 ^a	2.8 ^b	–	0.59 ^b
$^4P_{5/2}$ expt.	–	25 ^c	10.4 ^e	2.9 ^f	1.1 ^g	0.66 ^h

a) Chen et al. [149].

e) Schumann et al. [211].

b) Chen et al. [147].

f) Haselton et al. [277].

c) Donnally et al. [270].

g) Cocke et al. [282].

d) Richard et al. [280].

h) Sellin et al. [273].

Schuman et al. [211] for neon. These measurements are reviewed in the articles by Sellin [55] and Pegg [56] who discussed also life-time studies using methods [278–283] other than electron spectroscopy. Experimental results obtained from the beam-foil experiments are given in table 10.

More recent studies of metastable states by means of the electron-spectroscopy method has been made by Bruch et al. [284, 285] using beryllium and boron projectiles. Furthermore, Schneider et al. [243, 245] and Bruch et al. [241] studied carbon and oxygen, respectively, as partially shown in the previous section. In these experiments, gas targets were also used under single collision conditions. With heavy target atoms, various electron loss and capture events can occur in a single collision so that high spin states may readily be produced. Possible decay schemes for some high spin states are seen in fig. 48. Results for the Li-like state $1s2s2p$ 4P and the Be-like state $1s2s2p^2$ 5P are already discussed in section 5.3.1. The B-like state $1s2s2p^3$ 6S and the C-like state $1s2s2p^3s$ 7S have been studied by Schneider et al. [245]. In fig. 50, a Grottrian diagram is shown for the quintet system of Be-like carbon [245].

Several theoretical studies have been devoted to the decay modes of high-spin states of few electron ions. Calculations concerning the $1s2s2p$ 4P multiplet are attractive, since they allow a sensitive test of the magnetic spin–other orbit and spin–spin interaction mechanisms. Early theoretical studies by Manson [286] and Balashov et al. [287] provide reasonable estimates of the life time for the $1s2s2p$ $^4P_{5/2}$ state of light ions. Discrepancies between theory and experiment, however, occur for ions with $Z \geq 10$. These discrepancies have been removed by Cheng et al. [288] using relativistic (DS) wave functions in their calculations. Similar results have been obtained by Bhalla and Gabriel [289]. It is noted that accurate life-time calculations of the $1s2s2p$ $^4P_{5/2}$ state requires that one takes into consideration the M_2 radiative decay branch to the ground state. Hence, in addition to the life time, the calculations give information about the fluorescence yield.

It appears that the different life-time calculations for the $^4P_{5/2}$ state yield results which agree with each other rather closely [147, 148]. This is not true, however, for the $^4P_{1/2}$ and $^4P_{3/2}$ states which can decay through small admixtures of doublet components in addition to the magnetic interactions. The mixing coefficients are extremely sensitive on the atomic structure model used in the calculations. It was noted by Chen et al. [148] that a 7% error in the transition energy produce a change in the transition rate by an order of magnitude. To obtain accurate mixing coefficients, it is usually not sufficient to account for spin–orbit interaction alone in the energy matrix. Rather, it is necessary also to include additional relativistic effects represented by the Breit operator (section 2.1.1).

the Be-like lines A4, A5 and A6, i.e. from the intensity fraction of the triplet lines A5 and A6. Both methods yield a value close to 50% for the fraction of the metastable Ne projectiles [293]. Similar considerations yield a fraction of 40% for the metastable quartet states in the incident five-electron Ne ions.

The observed fractions of metastable projectiles appear to be surprisingly large. The numbers may be understood, if a statistical population of the multiplets is assumed. For instance, the fraction of all triplet states formed by the configurations $1s^22s^2$, $1s^22s2p$ and $1s^22p^2$ amounts to 65%. (This fraction might be altered by cascade transitions.) Statistical population of the multiplets is very likely to occur after the beam emerged from the stripping media (foil or gas) generally used with the high-energy accelerator. Since the levels 3P_0 , 3P_1 and 3P_2 for first row atoms have life times [79, 294] of the order of seconds, microseconds and milliseconds, respectively, practically all metastable ions survive their travel through a typical beam line of several tens of meters. Hence, the near statistical population of the metastable states observed at the location of the experimental set-up appears to be plausible.

5.4. L-Auger transitions

In general, the analysis of L-Auger electrons from fast projectiles requires a considerable amount of effort. This is primarily due to the problems involved in the complexity of the L-Auger spectra as has been shown in early projectile Auger measurements conducted by Volz and Rudd [162] and Stolterfoht et al. [191] with the $\text{Ar}^+ + \text{Ar}$ collision system. Spin-orbit interaction in the initial states as well as in the final state enhances considerably the number of possible Auger transitions. Hence, a typical L-Auger spectrum contains numerous overlapping lines and peak structures are generally associated with line groups rather than with individual lines. The analysis of individual lines is possible only in specific cases.

Individual lines are visible in L-Auger spectra from ions with near closed-shell configurations. For instance, the Auger spectra of rare gas atoms with a single L vacancy and a filled M shell have been analyzed in detail previously. The normal lines of the Ar-L Auger spectrum discussed in section 4.3 may be considered as an example.

Furthermore, near closed shell configurations occur in Na-like ions. As discussed in section 4.3, the Auger spectrum of Na itself has been studied in detail previously by means of target spectroscopy methods. Theoretical data for the Na configuration $2p^53s^2$ and $2p^53s3p$ are given in table 11. (In this section the printing of the passive 1s and 2s electrons will be suppressed.)

Studies with the method of projectile spectroscopy have been conducted by Pegg et al. [295] for Auger electrons from alkali atoms. Similar measurements of Ne have been made by Bisgaard et al. [296]. For the experiments, the projectile energy was chosen within the range of a few tens of keV. The polar broadening effect is sufficiently small so that individual lines are resolved in the Auger spectra. An example for the Auger spectrum of magnesium is given in fig. 51.

The lines in the magnesium spectrum may be identified using the theoretical data in table 11. The first prominent line at low energies (~ 35 eV) is attributed to the Na-like state $2p^53s^2\ ^2P$. It is seen that the resolution of about 0.2 eV is sufficient to exhibit the fine-structure splitting of the $P_{1/2}-P_{3/2}$ doublet.

The second and the third line in the magnesium spectrum are due to states associated with the Na-like configuration $2p^53s3p$. It is noted that this configuration involves also quartet states (table 11) which are metastable as shown by Pegg et al. [275] for Na-like chlorine. The structures at energies near 45 eV and higher are due to the configurations $2p^53snl$ involving a Rydberg electron with $n \geq 3$. As

Table 11
Calculated energies (in eV) of L-MM-Auger transitions in Na-like ions. The final ionic configuration is $2p^6$

Initial term	Angular momentum	Na	Mg	P	Ar	
		a)	a)	b)	c)	
$2p^5 3s^2 {}^2P$	3/2	25.74	35.20	64.67	102.57	
	1/2	26.21	–	65.68	104.77	
$2p^5 3s 3p {}^4S$	3/2	27.58	38.21	72.19	112.58	
	7/2	27.95	38.91	73.48	114.41	
				73.65	114.62	
	3/2			73.87	115.01	
4P	1/2			74.09	115.52	
	5/2			74.57	116.04	
	3/2	28.18	39.34	74.79	116.33	
	1/2			74.97	116.90	
$2p^5 3s({}^1P) 3p {}^2D$	5/2	–	39.51	75.68	118.15	
	3/2			75.31	117.50	
	2P	3/2	–	39.70	75.84	118.29
					75.59	117.68
2S	1/2	–	40.30	77.68	120.35	
	5/2	–	41.99	81.00	124.69	
$2p^5 3s({}^3P) 3p {}^2D$	3/2			81.52	125.57	
	2P	3/2	–	82.15	127.22	
				82.46	127.30	
	1/2			82.46	127.30	
2S	1/2		42.35	85.61	131.52	

a) Weiss, private communication in ref. [295].

b) Karim et al. [150].

c) Menzel and Mehlhorn [301] using the DF code by Grant [99].

pointed out in section 5.4.2, the states formed from the configuration $(2p^5 3s {}^3P)nl$ are expected to be rather long lived when n increases.

A systematic study of the L-Auger spectra including the Na-like isoelectronic sequence have been conducted by Dahl et al. [297] for the second row elements Na, Mg, Al, P and Cl as projectiles incident on Ar. In the experiments, the electrons were observed at 20° and the impact energy was chosen within the energy range of 10 to 90 keV. A typical example for the L-Auger spectra measured for Al is given in fig. 52. The data are obtained for the collision system 50-keV $Al^+ + Ar$.

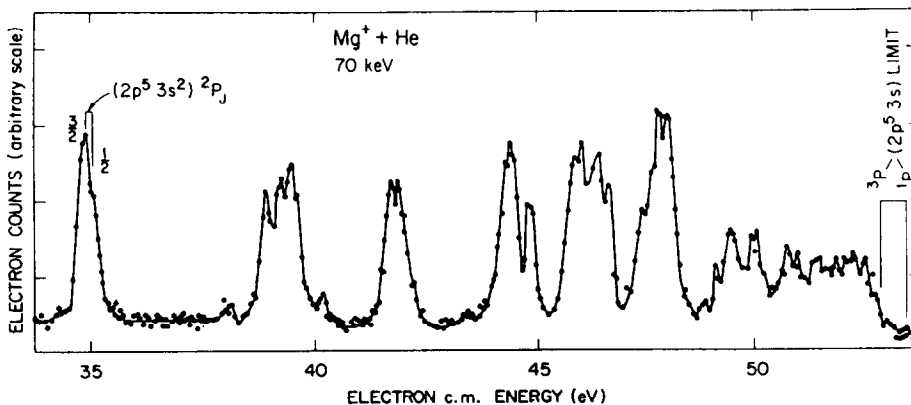


Fig. 51. L-Auger spectrum of magnesium produced in collisions of 70-keV $Mg^+ + He$. The electron energy refers to the projectile frame. From Pegg et al. [295].

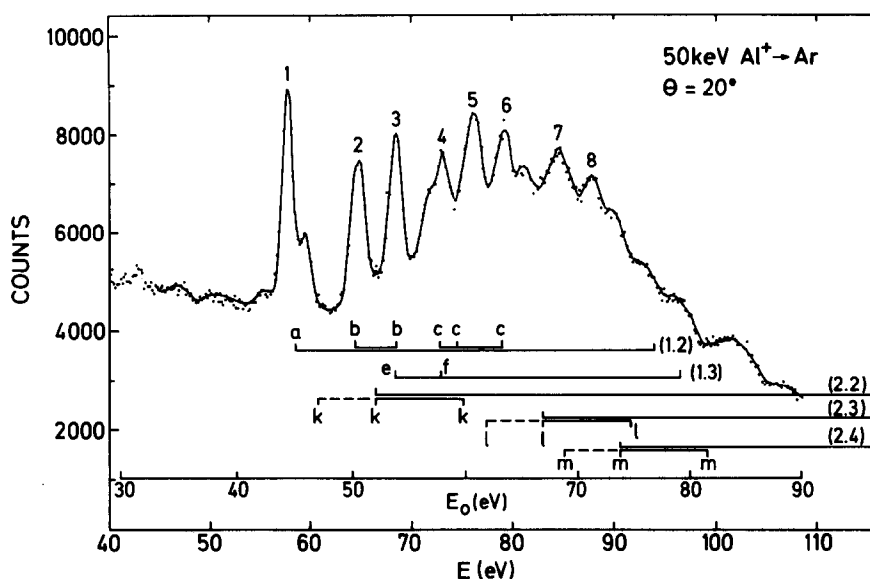


Fig. 52. L-Auger spectrum of aluminum produced in 50-keV $\text{Al}^+ + \text{Ar}$ collisions. Observation angle is 20° . The electron energy E_0 refers to the projectile frame and E refers to the laboratory rest frame. Energies are labeled (λ, ν) which indicates transitions $(\lambda - 1, \nu - 2)$ where λ is the number of initial $L_{2,3}$ vacancies and ν is the number of initial M electrons. From Dahl et al. [297].

In the Auger spectra measured by Dahl et al. [297] the first prominent line labeled 1 is attributed to the Na-like doublet $2p^5 3s^2 \ ^2P$ noted already in the magnesium spectrum (fig. 51). The other peaks are due to various configurations giving rise to several overlapping lines. An overview about the possible configurations may be obtained from the transition diagram in fig. 53 [269]. Although the diagram refers to the argon ion, it is well suited for similar elements to provide qualitative information about Auger transitions in Ne-, Na- and Mg-like systems.

In fig. 52 labels a, b and c are designated to the Na-like configuration with the outer-shell electrons $2p^5 3s^2$, $2p^5 3s 3p$ and $2p^5 3p^2$, respectively [297]. The labels e and f refer to the Mg-like initial configuration $2p^5 3s^2 3p$ decaying to the final states $2p^6 3p \ ^2P$ and $2p^6 2s \ ^2S$, respectively. From fig. 52 it is evident that it is difficult to analyze individual lines in the L-Auger spectra of elements heavier than Na and Mg.

Dahl et al. [297] performed a specific analysis of *double* L vacancy states. The energy-loss data by Fastrup et al. [298] show that the $4f\sigma$ promotion mechanism responsible for the L-shell excitation in the present collision systems favors the production of double L vacancy states. Indeed, the spectra give indication for the presence of various configurations associated with two L vacancies (labels k and m in fig. 52). The decay mechanisms of double-vacancy states considered by Dahl et al. [297] refer to the cascade transition $2p^6 \leftarrow 2p^5 3s^2 \leftarrow 2p^4 3s^2 3p^2$ (fig. 53).

An interesting feature of the Auger spectra measured by Dahl et al. [297] is the structure seen at energies below the prominent peak 1. This structure is found to be significant in the Auger spectra of Na and Mg, but it is observed also when heavier projectiles such as chlorine are used. Dahl et al. [297] attributed the low energy peak to Coster-Kronig transitions following the creation of vacancies in the L_1 shell. This explanation is certainly adequate for Na and Mg, however, it is questionable for the heavier elements. As the outer-shell charge state increases in heavier systems, Coster-Kronig transitions become energetically forbidden [299]. An alternative explanation for the low energy peak is that it

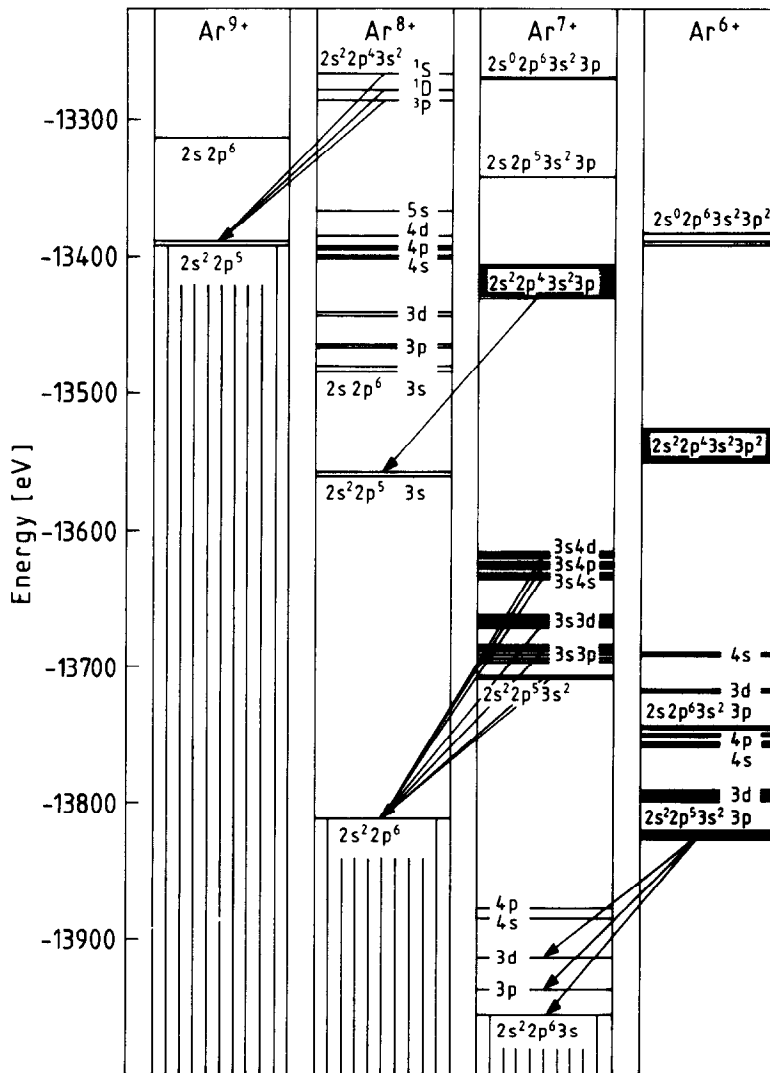


Fig. 53. L-Auger transitions diagram for F-, Ne-, Na- and Mg-like Ar. Various levels are shown referring to single and double hole states for the L_1 and $L_{2,3}$ shell. The diagram is based on calculations by Stolterfoht [269] using the DF code by Grant [99].

is due to the three-electron transition from the Mg-like configuration $2p^5 3s^2 3p$ to the final configuration $2p^6 3d$. This transition will be discussed in more detail below together with the Ar-L-Auger spectra.

A detailed spectroscopic analysis of the phosphorus-L-Auger spectrum has been conducted by Ridder and Schneider [299]. The projectile energy was chosen to be 500 keV. To maintain a small polar broadening effect, the electrons were observed at the forward angle of 9° . Furthermore, Ridder and Schneider [299] performed transition energy calculations using the HF code of Froese-Fisher [97]. In fig. 54, experimental and theoretical results for the phosphorus-L-Auger transitions are compared.

In the phosphorus spectrum, most spectral structures are recognized to be associated with Na- and Mg-like configurations, e.g. peak 2 is attributed to the $2p^5 3s^2 \ ^2P$ doublet. However, difficulties still exist in the identification of peak 1. Ridder and Schneider [299] suggested that this peak is attributed to a configuration with three L-shell vacancies. Alternatively, peak 1 may be considered to be designated to the three-electron transition $2p^6 3d \leftarrow 2p^5 3s^2 3p$ mentioned above.

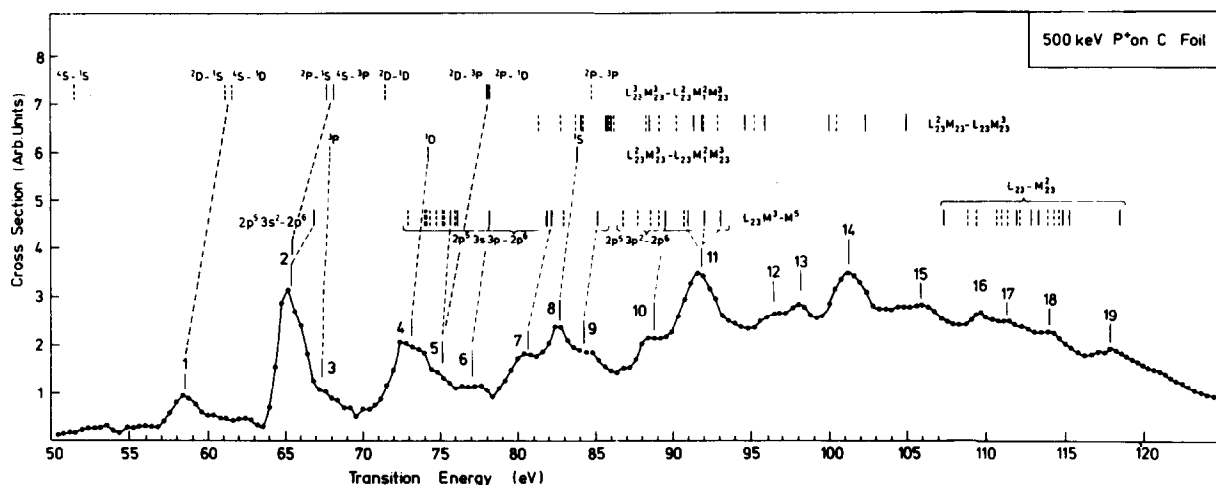


Fig. 54. L-Auger spectrum of phosphorus produced by 500-keV P^+ impact on a thin C foil. Observation angle is 9° . The electron energy refers to the projectile frame. Theoretical results from the HF code by Froese-Fisher are indicated above the spectrum. From Ridder and Schneider [299] where also the key to the line assignment is given.

Elaborate calculations using the intermediate coupling scheme and including configuration interaction have been performed by Karim et al. [150] for the phosphorus-L-Auger spectrum. The calculations were made for various Na-like configurations incorporating 3s, 3p and 3d electrons. Again, an overview about the transitions involved may be obtained from fig. 53. In table 11 theoretical results are given for the configurations $2p^5 3s^2$ and $2p^5 3s 3p$. Transition rates and fluorescence yields were determined in addition to the transition energies. Karim et al. [138] assigned almost all spectral structures observed in fig. 54.

In certain cases, extensive calculations of individual Auger transitions alone may be misleading. With the large number of states available in open shell ions, it is always possible to find an Auger transition suitable in energy to assign a given line. For instance, Karim et al. [150] were able to assign almost all peaks of the phosphorus spectrum (fig. 54) to states associated with Na-like configurations. However, it is very likely that also Mg- and Al-like configurations are present in the 500-MeV phosphorus ions emerging from the carbon foil.

The data for phosphorus may be considered as typical example for the serious difficulties encountered in the analysis of the L-Auger spectra. Phosphorus is an element with a half open M-shell for which a large number of L-Auger transitions are possible. For a first analysis it appears reasonable to conduct term-averaged calculations, in order to obtain an insight to the main features of the Auger spectrum [299]. In addition, it is useful to consider information about the projectile energy dependence of the peak intensities and the expected charge state of the excited ion.

As a result of the problems produced by the complexity of L-Auger spectra, it is particularly important to develop experimental methods which allows one to reduce the number of lines. Here, needle ionization gains specific importance. In fact, the first measurements by Itoh et al. [61] using needle ionization in conjunction with the method of zero-degree Auger spectroscopy were devoted to Ar-L-Auger spectra. An example of that work for the collision system $Ar^{5+} + He$ is given in fig. 55. In comparison with the data shown previously (figs. 51 and 52) the Ar spectrum is remarkably simple. This indicates that needle ionization is particularly useful for ions with several electrons.

The Ar spectrum consists of four peak groups attributed to Na- and Mg-like configurations which are shown in the transition diagram (fig. 53). States formed by the Na-like configurations [301] are given in

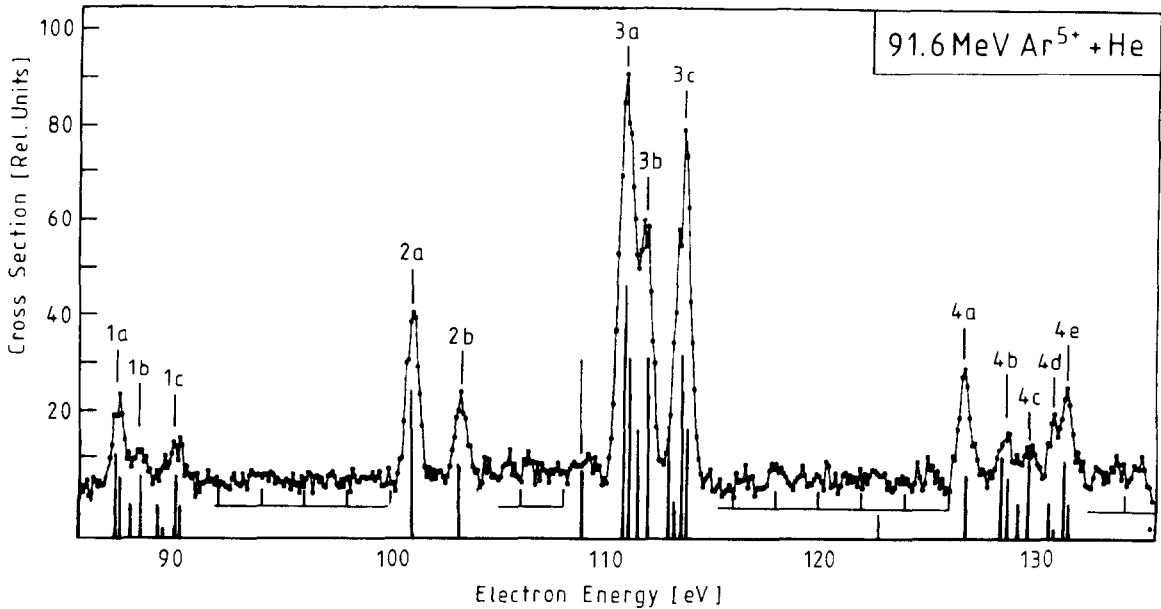


Fig. 55. L-Auger spectrum of argon produced in collisions of 91.6-MeV Ar^{5+} on He. The observation angle is 0° . The electron energy refers to the projectile frame. The vertical lines refer to theoretical transition energies calculated by Stolterfoht [269] using the DF code by Grant [99]. From Itoh et al. [61].

table 11. Group 2 clearly shows the line pair associated with the $2p^5 3s^2 \ ^2P$ doublet also observed for Ar by means of target spectroscopy [20, 195]. The line separation is equal to the $2p_{3/2} - 2p_{1/2}$ fine-structure splitting of 2.2 eV for Ar. Peak group 2 is created by the removal of the 3p electron in addition to the 2p electron indicating a breakdown of the needle ionization concept. However, in most cases, needle ionization works well. The single ionization of the 2p electron produces the Mg-like configuration $2p^5 3s^2 3p$. Peak groups 1, 3 and 4 are designated to the final configurations $2p^6 3d$, $2p^6 3p$ and $2p^6 3s$, respectively [61, 300].

Various states are attributed to the initial configuration $2p^5 3s^2 3p$. In LS coupling one obtains the 6 states 1S , 1D , 1P , 3S , 3D and 3P as shown in table 12. They form a basis for the 10 states obtained in intermediate coupling. The related expansion coefficient calculated by Hansen [302] are given in table 12. It is seen that, in several cases, no single LS coupling state dominates in the basis expansion. This indicates that the LS coupling scheme breaks down completely for the states considered here. Evidently, the application of the intermediate coupling scheme is needed for L-vacancy states of multiply ionized argon.

In table 12 the state energies are given relative to the Na-like ground state configuration $2p^6 3s$. The Auger decay into the corresponding final state is represented by the lowest lying arrow on the right hand side of the transition diagram in fig. 53. The corresponding transition energies are indicated by lines below the peak group 4 in the Ar-L spectrum (fig. 55). It is seen that the peak group 4 is well reproduced by the theoretical predictions. Similar results have been obtained by Sekiya et al. [303] for peak group 3.

Apart from changes in the intensities, the line structures of the peak groups 1 and 3 are equal to those of the peak group 4. This is due to the fact that the three line groups originate from the same initial states. The intensities for the different lines associated with a given initial state are determined by

Table 12

Square of the expansion coefficients of intermediate coupling states specified by the total angular momentum. The basis are LS coupling states formed by the Mg-like configurations $2p^53s^23p$, $3s3p3d$ and $3p3d^2$ as indicated. For the first configuration contributions to individual terms are given, for the other configurations all terms are summed. The energies [269] of the states are given relative to the Na-like ground state $2p^63s$. They are shifted by 2.2 eV to match the experimental data for the first ($J = 1$) line. From Hansen [302]

Total angular momentum	Energy [eV]	$3s^23p$					$3s3p3d$ all	$3p3d^2$ all	
		3S	3D	3P	1S	1D			1P
1	126.79	0.896	0.000	0.057	–	–	–	0.015	0.0017
3	128.49	–	0.960	–	–	–	–	0.018	0.0014
2	128.62	–	0.672	0.077	–	0.210	–	0.023	0.0014
1	129.28	0.005	0.440	0.192	–	–	0.322	0.017	0.0013
2	129.80	–	0.003	0.629	–	0.327	–	0.020	0.0013
1	130.80	0.000	0.513	0.104	–	–	0.343	0.017	0.0013
0	131.02	–	–	0.948	0.010	–	–	0.020	0.0017
2	131.44	–	0.285	0.253	–	0.421	–	0.019	0.0013
1	131.54	0.062	0.007	0.605	–	–	0.283	0.019	0.0013
0	140.62	–	–	0.010	0.939	–	–	0.029	0.0019

the relevant branching ratios, see eq. (1.2.6). It is seen that in some cases the branching ratios strongly favour certain final states. For instance, the line attributed to the lowest lying $J = 1$ state is found to be rather strong in peak group 4 whereas the corresponding lines are weak in the peak groups 1 and 3 [300]. Obviously, there is no selection rule which forbids transitions from the lowest lying $J = 1$ state to final configurations other than $2p^63s$. Here, specific transition rate calculations are needed to clarify the situation [303].

The appearance of the peak group 1 gives rise to intriguing questions. The good agreement between theoretical and experimental transition energies excludes doubts about the interpretation of peak group 1 as being due to the transitions between the configurations $2p^53s^23p$ and $2p^63d$. The comparison of the initial and final configuration indicates that *three* electrons are affected in the Auger decay [300]. The three-electron transition is not describable in first-order perturbation theory, since the Coulomb interaction involves a two-body operator. Hence, the description of the Auger effect producing the peak group 1 leads beyond the Wentzel Ansatz treating transitions between single configuration states.

It may be anticipated that configuration interaction produce admixtures of $3d$ electron in the initial state. Table 12 shows that the contributions of the configurations $2p^53s3p3d$ and $2p^53p3d^2$ to the initial state does not exceed 3% [302]. This value is too small to explain the peak group 1 which amounts to 12% in intensity relative to that of the groups 1, 3 and 4. Hence, it is not expected that configuration interaction in the initial state is important for peak group 1. Also, because of selection rules it is not possible to attribute peak group 1 to electron shake-up or configuration interaction in the final ionic state.

Alternatively, it is to be considered that interchannel configuration interaction plays a role in the final state [fig. 4]. Peak group 1 can be produced when the final state is a mixture of the channels $2p^63s\epsilon l$ (or $2p^63p\epsilon l$) and $2p^63d\epsilon l'$. Hence, the production of peak group 1 may be described in terms of the 'conventional' Auger transition from the initial configuration $2p^53s^23p$ to the configuration $2p^63s\epsilon l$ (or $2p^63p\epsilon l$) coupled by an interchannel interaction to the final state $2p^63d\epsilon l'$. These processes are shown schematically in fig. 56.

The $2p^63d\epsilon l - 2p^53s^23p$ transition which affects three electrons can be described using many-body

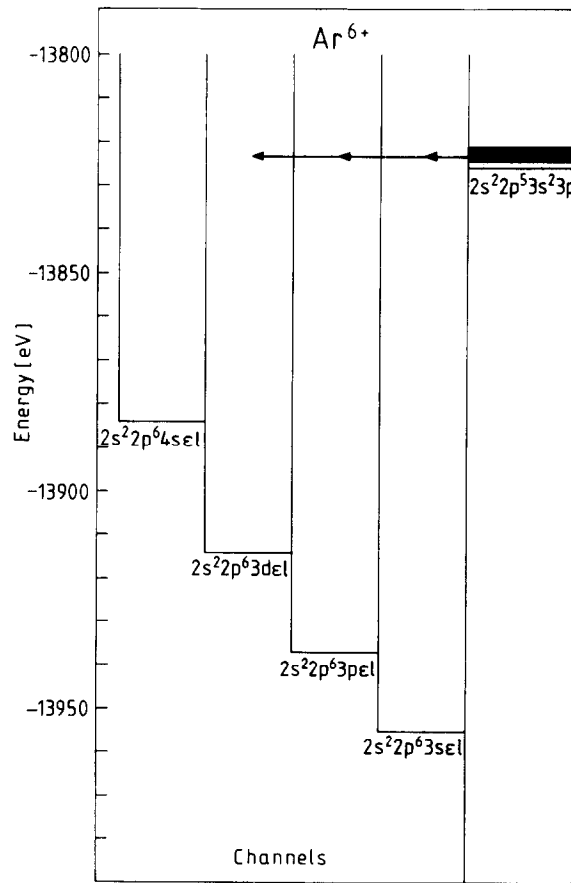


Fig. 56. L-Auger transition diagram of argon including final state channels. Apart from the 'conventional' Auger effect, interchannel transitions are shown. The diagram is based on calculations by Stolterfoht [269] using the DF code by Grant [99].

perturbation theory [102] in second order or the scattering approach by Åberg [78]. It is noted that the states produced in highly-ionized atoms give rise to interesting processes including higher-order effects on the Auger transitions.

5.5. Transitions involving Rydberg electrons

A vacancy collisionally created in a low-lying subshell of the atom is generally filled by an electron from a subshell with the same principal quantum number giving rise to a *Coster-Kronig* electron (section 1.2). The energy difference between the subshell orbitals is relatively small so that the energy of the ejected electron is comparably low. In fact, usually, the *Coster-Kronig* transitions are energetically forbidden in multiply ionized atoms. This has been pointed out for the $L_1-L_{23}M$ transition of Ar^{6+} in the previous section [299]. The *Coster-Kronig* transitions become possible, however, when loosely bound Rydberg electrons are present in the atom. Hence, the study of the electrons from the *Coster-Kronig* transitions provides information about Rydberg states occupied in the atom or ion.

The low-energy autoionization electrons are ejected only in a small cone of forward angles. Thus, it is useful to measure the autoionization electrons at an observation angle of 0° with respect to the

incident beam direction. In this case, the autoionization electrons are seen in the vicinity of the electron-loss to continuum (ELC) or the electron-capture to continuum (ECC) peak [60, 160, 304]. These cusp peaks are centered at an electron energy which corresponds to a velocity equal to the projectile velocity. The low-energy autoionization electrons are superimposed on the wings of the cusp peak as first observed by Lucas and Harrison [60]. Similar measurements [234, 235, 305–307] of the projectile autoionization electrons revealed a number of peaks which can be attributed to a series of Rydberg states.

Suter et al. [234] studied the configuration $1s^2 2pnl$ produced in collisions of heavy ions incident at several tens of MeV on Ar. The electrons spectrum obtained in 25-MeV $O^{4+} + Ar$ collisions is depicted in fig. 57. Superimposed above the electron loss maximum, the spectrum shows several peaks each of which is associated with a certain n -quantum number of the Rydberg electron.

When the O^{4+} is incident in its ground state configuration $1s^2 2s^2$ the configuration $1s^2 2pnl$ is produced by double excitation involving 2s electrons. The same configuration is produced by *single* 2s excitation, if the projectile is incident in the metastable state $1s^2 2s 2p^3 P$. In section 5.3.2 it was shown that the fraction of ions in this metastable state may amount to 50%. Hence, it is expected that the autoionization lines are produced mainly by single 2s excitation and that *triplet* states are primarily created.

In fig. 57 the spectrum provides a good example for line doubling effects (section 3). The structures at the low-energy side of the electron loss peak are produced as the reflected image of the structures at the high-energy side (see also fig. 40). Also, these effects have been observed by Anderson et al. [305] for C^{2+} , O^{4+} and F^{5+} and by Itoh and Stolterfoht [306] for Ne^{6+} . In general, after the transformation into the projectile frame the structures at the low- and high-energy side are found to be equal. This shows for the cases studied that in the projectile rest frame the probabilities for electron ejection at 0° and 180° are equal within the experimental uncertainties.

Further measurements of electrons from autoionizing Rydberg states have been made by Anderson et al. [235, 305] for Au^{q+} projectiles with the charge states $5 \leq q \leq 19$ and by Stolterfoht et al. for O^{3+}

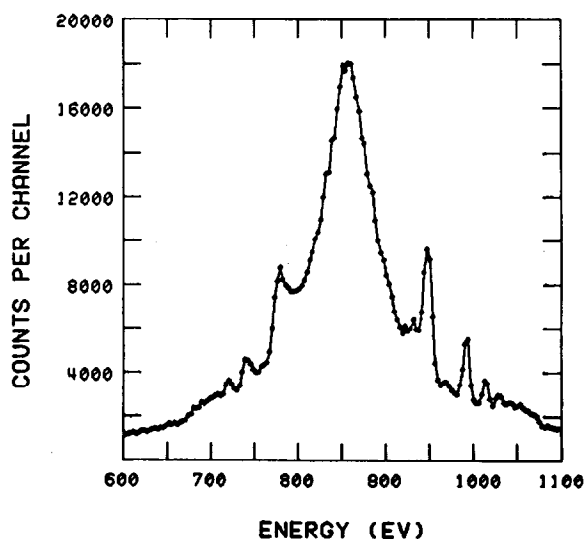


Fig. 57. Spectrum of electrons ejected at 0° in collisions of 25-MeV O^{4+} on Ar. The electron energy refers to the laboratory frame of reference. From Suter et al. [234].

[308] and Ne^{4+} [231]. In these collision systems various configurations are produced and the observed spectra are found to be rather complex so that a detailed analysis has not as yet been carried out. Therefore, the following discussion will be focused on the configurations $1s^2 2pnl$ which produce relatively simple spectral structures.

Measurements with improved resolution have been made by Schneider et al. [307] studying 85-MeV Ne^{6+} in collisions with He. The results obtained after the transformation into the projectile rest frame are shown in fig. 58. The spectrum clearly indicates a series of lines associated with the Rydberg states. It is seen that the *Coster-Kronig* transitions become energetically possible for $n \geq 7$.

If the term splitting and the spin-orbit splitting is disregarded, it follows for the energy of the ejected autoionization electrons that [234, 235]

$$\varepsilon_{nl} = \Delta E_{2s2p} - \frac{Q^2}{2(n - \mu_l)^2} \quad (5.5.1)$$

where Q is the effective charge of the atomic core seen by the Rydberg electron, μ_l is its quantum defect depending on the angular momentum l , and ΔE_{2s2p} is the energy difference between the 2s and 2p orbital. The quantity ΔE_{2s2p} is given for C^{3+} , O^{5+} and Ne^{7+} in table 8.

The spectrum by Schneider et al. (fig. 58) shows indications for the quantum defect of the Rydberg orbitals. For instance, the $n = 7$ peak group exhibits structures which can be associated with the angular momenta $l = 0, 1$ and higher of the configuration $1s^2 2pnl$. From these structures it is possible to obtain information about the population of the angular momenta of the Rydberg electron [307].

Further improvements of the resolution have been achieved in measurements dealing with the collision system 3.5-MeV $\text{C}^{3+} + \text{He}$ [308]. The results are shown in fig. 59. In collisions of C^{3+} on He, the incident configuration $1s^2 2s$ is converted to the configuration $1s^2 2pnl$ by a transfer-excitation process

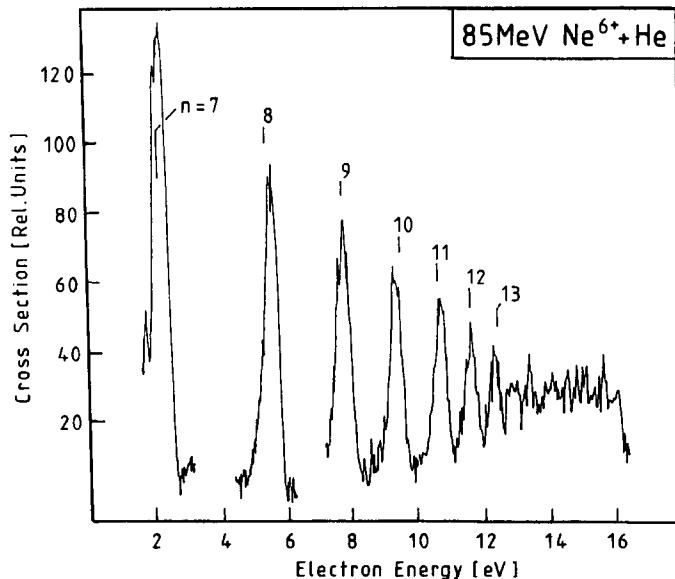


Fig. 58. Spectrum of electrons ejected at 0° in collisions of 85-MeV Ne^{6+} on He. The data representing the high-energy part of the laboratory rest frame spectrum are transformed into the projectile rest frame. From Schneider et al. [307].

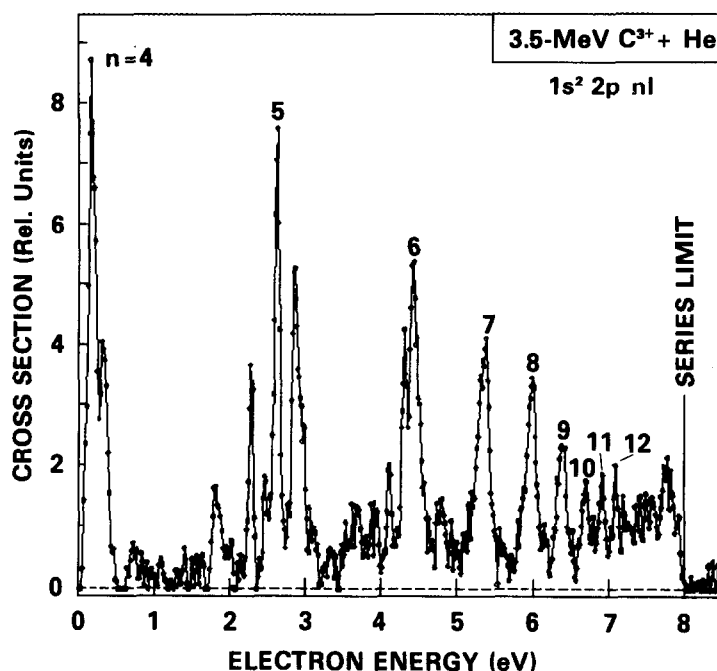


Fig. 59. Spectrum of electrons ejected at 0° in collisions of 3.5-MeV C^{3+} on He. The data are transformed into the projectile rest frame. They represent the high-energy part of the spectrum obtained at the laboratory rest frame. From Stolterfoht et al. [308].

[265, 305]. Hence, in this case the occupation of the Rydberg is associated with a capture event rather than with electron excitation as in the cases discussed before.

Figure 59 indicates that in the carbon ion the *Coster-Kronig* transitions become allowed for $n \geq 4$. The case $n = 4$ is particularly interesting, since part of the lines produced in that group fall below the zero energy threshold and some of the lines are produced just above the threshold [309]. For instance, a line is observed at 0.18 eV which is attributed to the term $1s^2 2p 4d^3 D$ [79]. Its line width has been observed to be as small as 20 meV in the projectile frame demonstrating that the technique of zero-degree Auger spectroscopy yields rather high-energy resolution.

It is noted that electrons of such low energy are difficult to measure with high resolution when they originate from target atoms which are practically at rest in the laboratory frame of reference. However, as seen in fig. 59, the present technique of kinematic line shifting inherent in the projectile spectroscopy method has access to energies in the sub-eV region.

It is seen that the intensity of the lines is decreasing with increasing n . For $n \geq 6$ it is found that the occupation of the n -quantum number follows the well-known n^{-3} law [308]. In fact, also the spacing of the lines associated with adjacent n quantum numbers is governed by the n^{-3} rule. Therefore, in the region where the lines overlap the spectral intensity is nearly constant until the series limit is reached.

To obtain more detailed information about the occupation of the angular momenta of the Rydberg electrons, the experimental data are compared with theoretical results for transition energies and autoionization widths provided by Griffin et al. [309]. Figure 60 shows results for the peak associated with the principal quantum number $n = 5$. It is seen that the term splitting produced by the coupling of the Rydberg electron with the 2p electron is not negligible as assumed in conjunction with eq. (5.5.1). In fact, the term splitting is of the same order of magnitude as the quantum defect. It is noted,

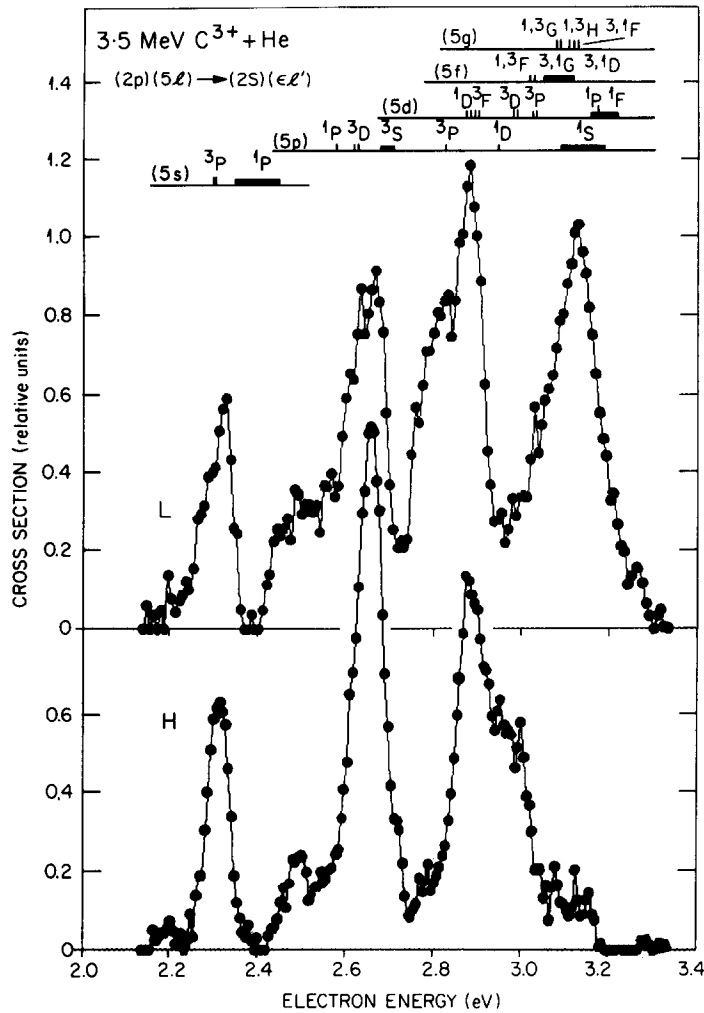


Fig. 60. Spectrum of the peak group associated with the configuration $1s^2 2p 5l$ produced in collisions 3.5-MeV C^{3+} on He. The electron energy refers to the projectile rest frame [301]. The term energies and widths given above the spectrum are from calculations by Griffin et al. [309]. The labels H and L refer to electrons emitted at 0° and 180° , respectively, in the projectile rest frame. From Yamazaki et al. [311].

however, that the spin-orbit splitting is small for the C^{2+} carbon ion studied here. But, for instance Ne^{6+} studied by Schneider et al. [307] shows significant term splitting produced by spin-orbit interaction.

In fig. 60 the spectrum exhibits three prominent peaks which may be attributed to the angular momenta of the Rydberg electron. The first peak is due to the single term $1s^2 2p 5s \ ^3P$ which represents the s state of the Rydberg electron. Similarly, the second peak is composed of lines attributed to the p state of the Rydberg electron. The third peak, however, is a composition of lines due to the angular momenta p, d and, possibly, f. Estimates show that the contributions from the p state amounts to a fraction of about 0.3. Hence, from the line intensities it follows that in collisions of 5-MeV C^{3+} on He, the angular momenta s, p and d are produced with the approximate probabilities of 0.2, 0.5 and 0.3, respectively. For lower projectile energies the contribution from the s state is found to be enhanced [308].

The results for the excitation probabilities are obtained under the assumption that the ejection of the autoionization electrons is isotropic, i.e. the magnetic quantum numbers of a given term are equally populated. It is noted that Auger transitions regarded in fig. 60 where the final ion remains in an S state, the present method of zero-degree spectroscopy is sensitive only to the intensity attributed with the magnetic quantum number $M_L = 0$. Observations of nonstatistical population of the magnetic quantum numbers, i.e. the alignment of the autoionization states produced, have been reported previously [196, 197]. In addition, deviations from the backward–forward symmetry in the electron ejection produced by post-collision Stark mixing of closely lying states of different parity have been observed in the experiment [310]. Figure 60 shows similar asymmetries produced by direct overlap of the closely lying resonances [311]. Hence, certain caution is needed when total cross sections are extracted from electron measurements performed at one observation angle. Future work appears to be required to study the full angular distribution of the electrons from autoionizing Rydberg states.

Acknowledgement

I am very much indebted to my colleagues Drs. Dieter Schneider and Akio Itoh for the fruitful collaboration in the work undertaken at HMI. I would like to express my thanks for lively discussions with Drs. Teijo Åberg, Antoine Salin, Rido Mann, Manfred Krause, Thomas Carlson, Sheldon Datz and W. Mehlhorn, helping to improve the present article. I would like to thank Drs. David Pegg, Thomas Schneider and Theo Zouros for reading the manuscript and for enlightening comments. I appreciate much the communication of transition energy calculations by Drs. E.J. Hansen, W. Menzel and D. Griffin. The hospitality of the Atomic Physics Group at ORNL where part of the article was written is gratefully acknowledged. Special appreciations are devoted to Frau Regina Herzog and Herrn Charly Grey for very helpful communications. I would like to thank Frau Eva Ochmann and Mrs. Janice Helton for their infinite patience in typing the manuscript.

Appendix A1. Summary of atomic units

1. Fundamental quantities

Length (Bohr radius):	$a_0 = 5.291 \times 10^{-9}$ cm
Action (Planck's constant):	$\hbar = 6.521 \times 10^{-16}$ eV s
Charge (electron):	$e = 1.602 \times 10^{-19}$ C

2. Other quantities

Energy (Hartree):	$H = 27.211$ eV
Time:	$\tau = 2.418 \times 10^{-17}$ s
Velocity:	$v_0 = 2.187 \times 10^8$ cm/s

In atomic units, the velocity of light is given by the inverse of Sommerfeld's fine structure constant, i.e. $c = 137$ a.u.

Appendix A2. Expansion coefficients

Coefficients [in a.u.] for the Z expansions of the energy levels in the singly core-excited Li-like and the doubly core-excited He-like isoelectronic sequence. From Rødbro et al. [253]

State	Expansion coefficients			
	Power of Z			
		Expt. ^{a)}	Theory ^{b)}	
$(1s2s^2)^2S$	Z^2	E_0	-0.7521	-0.75000
	Z	E_1	0.5469	0.53146
	Z^0	E_2	-0.2780	-0.24399
$1s(2s2p^3P^o)^2P^o$	Z^2	E_0	-0.7526	-0.75000
	Z	E_1	0.6216	0.60412
	Z^0	E_2	-0.4045	-0.38166
$1s(2s2p^1P^o)^2P^o$	Z^2	E_0	-0.7528	-0.75000
	Z	E_1	0.6495	0.62544
	Z^0	E_2	-0.4312	-0.37963
$(1s2p^2)^2D$	Z^2	E_0	-0.7503	-0.75000
	Z	E_1	0.6552	0.65368
	Z^0	E_2	-0.4429	-0.42968
$(1s2s2p)^4P^o$	Z^2	E_0	-0.7531	-0.75000
	Z	E_1	0.5733	0.54647
	Z^0	E_2	-0.3112	-0.24166
$(2, 2\alpha)^1S$	Z^2	E_0	-0.2494	
	Z	E_1	0.1184	
	Z^0	E_2	-0.0174	
$(2, 2\alpha)^3P^o$	Z^2	E_0	-0.2501	-0.25000
	Z	E_1	0.1328	0.13281
	Z^0	E_2	-0.0249	-0.02944
$(1, 1\alpha)^1D$	Z^2	E_0	-0.2497	
	Z	E_1	0.1763	
	Z^0	E_2	-0.0541	
$(2, 2\alpha)^1P^o$	Z^2	E_0	-0.2501	0.25000
	Z	E_1	0.1882	0.19141
	Z^0	E_2	-0.0695	-0.09555

^a Rødbro et al. [253].

^b Three-electron states: Safronov and Kharitonova [247]. Two-electron states: Chan and Stewart [260].

References

- [1] P. Auger, Compt. Rend. 177 (1923) 169; 180 (1925) 65.
- [2] P. Auger, J. Phys. Radium 6 (1925) 205.
- [3] G. Wentzel, Z. Phys. 43 (1927) 524.

- [4] P.G. Burke, *Advances in Atomic and Molecular Physics*, Vol. 4, eds. D.R. Bates and I. Estermann (Academic Press, New York, 1968) p. 173.
- [5] E.H.S. Burhop and W.N. Asaad, *Advances in Atomic and Molecular Physics*, Vol. 8 (Academic Press, New York, 1972) p. 164.
- [6] D. Chattarji, *The Theory of Auger Transitions* (Academic Press, New York, 1976).
- [7] E.J. McGuire, *Atomic Inner-Shell Processes*, Vol. I, ed. B. Crasemann (Academic Press, New York, 1975) p. 293.
- [8] T. Åberg and G. Howat, *Handbuch der Physik*, Vol. 31, eds. S. Flügge and W. Mehlhorn (Springer Verlag, Berlin, 1982) p. 469.
- [9] G.N. Ogurtsov, *Rev. Mod. Phys.* 44 (1972) 1.
- [10] A. Niehaus, *Atomic Inner-Shell Physics*, ed. B. Crasemann (Plenum Press, New York, 1985) p. 377.
- [11] M.E. Rudd and J. Macek, *Case Studies in Atomic Physics*, Vol. 3, eds. E.W. McDaniel and M.R.C. McDowell (North-Holland, Amsterdam, 1973) p. 47.
- [12] K.D. Sevier, *Low Energy Electron Spectrometry* (J. Wiley Interscience, New York, 1972).
- [13] W. Mehlhorn, *Electron Spectrometry of Auger and Autoionizing States: Experiment and Theory*, Lecture Notes, University of Aarhus (1978) unpublished.
- [14] W. Mehlhorn, *Atomic Inner-Shell Physics*, ed. B. Crasemann (Plenum Press, New York, 1985) p. 119.
- [15] D.L. Matthews, *Methods of Experimental Physics*, Vol. 17, ed. P. Richard (Academic Press, New York, 1980) p. 433.
- [16] N. Stolterfoht, *Fourth Conf. on the Scientific and Industrial Applications of Small Accelerators*, IEEE Trans. Nucl. Sci. 76CH1175-8 NTS (1976) p. 311.
- [17] N. Stolterfoht, *Topics in Current Physics*, Vol. 5: Structure and Collisions of Ions and Atoms, ed. I.A. Sellin (Springer Verlag, Berlin, 1978) p. 155.
- [18] N. Stolterfoht, *Fundamental Processes in Energetic Atomic Collisions*, eds. H.O. Lutz, J.S. Briggs and H. Kleinpoppen (Plenum Press, New York, 1983) p. 295.
- [19] D. Berényi, *Advances in Electronics and Electron Physics*, Vol. 56 (Academic Press, New York, 1981) p. 411.
- [20] R. Mann, F. Beyer and F. Folkmann, *XII Intern. Conf. on the Physics of Electronic and Atomic Collisions*, Invited Papers, ed. S. Datz (North-Holland, Amsterdam, 1981) p. 683.
- [21] J.D. Garcia, R.J. Fortner and T.M. Kavanagh, *Rev. Mod. Phys.* 45 (1973) 111.
- [22] A.C. Kessel and B. Fastrup, *Case Studies in Atomic Physics*, Vol. 3, eds. E.W. McDaniel and M.C. McDowell (North-Holland, Amsterdam, 1973) p. 137.
- [23] W.E. Meyerhof and K. Taulberg, *Ann. Rev. Nucl. Sci.* 27 (1977) 279.
- [24] H.R. Robinson and A.M. Cassie, *Proc. Roy. Soc. Ser. A* 113 (1926) 282.
- [25] C. Groyles, D. Thomas and S.K. Haynes, *Phys. Rev.* 89 (1953) 715.
- [26] J.C. Niall, C.L. Baird and S.K. Haynes, *Phys. Rev.* 118 (1960) 1278.
- [27] H. Beutler, *Z. Physik* 63 (1935) 177.
- [28] R.P. Madden and K. Codling, *J. Astrophys.* 141 (1965) 364.
- [29] K. Codling, R.P. Madden and D.L. Ederer, *Phys. Rev.* 155 (1967) 26.
- [30] E.N. Lassetre, *Suppl. Radiation Research* 1 (1959) 530.
- [31] R.P. Madden and K. Codling, *Phys. Rev. Lett.* 10 (1963) 516.
- [32] U. Fano, in: *Atomic Physics* (Plenum Press, New York, 1969) p. 209.
- [33] U. Fano and J.W. Cooper, *Phys. Rev.* 137 (1965) A1364.
- [34] W. Mehlhorn, *Phys. Lett.* 21 (1966) 155.
- [35] W. Mehlhorn, *Z. Physik* 160 (1960) 247.
- [36] H.W. Berry, *Phys. Rev.* 121 (1961) 1714.
- [37] M.E. Rudd, *Phys. Rev. Lett.* 13 (1964) 503; 15 (1965) 580.
- [38] T.A. Carlson and M.O. Krause, *Phys. Rev. Lett.* 14 (1965) 390.
- [39] K. Siegbahn, C. Nordling, G. Johansson, J. Hedman, P.F. Heden, K. Hamrin, U. Gelius, T. Bergmark, L.O. Werme, R. Manne and Y. Baer, *ESCA Applied to Free Molecules* (North-Holland, Amsterdam, 1969).
- [40] M.O. Krause, *Atomic Inner Shell Processes*, Vol. II, ed. B. Crasemann (Academic Press, New York, 1975) p. 33.
- [41] T.A. Carlson, *Photo Electron and Auger Spectroscopy* (Plenum Publishing Corporation, New York, 1975).
- [42] P.J. Hicks and J. Comer, *J. Phys. B* 8 (1975) 1866.
- [43] B.R. Barker and H.W. Berry, *Phys. Rev.* 151 (1966) 14.
- [44] M.E. Rudd, T. Jorgenson Jr. and D.J. Volz, *Phys. Rev. Lett.* 16 (1966) 929 and *Phys. Rev.* 151 (1966) 28.
- [45] Yu.S. Gordeev and G.N. Ogurtsov, *Zh. Eksp. Teor. Fiz.* 60 (1971) 2051 [*Sov. Phys.-JETP* 33 (1971) 1105].
- [46] R.K. Cacaek, Q.C. Kessel and M.E. Rudd, *Phys. Rev. A* 2 (1970) 1327.
- [47] D.L. Matthews, B.M. Johnson, J.J. Mackey and C.F. Moore, *Phys. Rev. Lett.* 31 (1973) 1331.
- [48] D. Burch, P. Richard and R.L. Blake, *Phys. Rev. Lett.* 26 (1971) 26.
- [49] N. Stolterfoht, D. Schneider, R. Mann and F. Folkmann, *J. Phys. B* 10 (1977) L281.
- [50] D. Schneider, M. Prost, R. DuBois and N. Stolterfoht, *Phys. Rev. A* 25 (1982) 3102.
- [51] R. Mann and F. Folkmann, *J. Physique* 40 (1979) C1-236.
- [52] C. Woods, R.L. Kauffman, K. Jamison, N. Stolterfoht and P. Richard, *Phys. Rev. A* 12 (1975) 1393.
- [53] I. Kádár, S. Ricz, V.A. Shchegolev, B. Sulik, D. Varga, J. Végh, D. Berényi and G. Hock, *J. Phys. B* 18 (1985) 275.
- [54] T. Matsuo, J. Urakawa, A. Yagishita, Y. Awaya, T. Kambara, M. Kase and H. Kumagai, *J. Phys. B* 16 (1983) L239.

- [55] I.A. Scellin, Topics in Current Physics, Vol. I: Beam Foil Spectroscopy, ed. S. Bashkin (Springer Verlag, Heidelberg, 1976) p. 265.
- [56] D.J. Pegg, Methods of Experimental Physics, Vol. 17, ed. P. Richard (Academic Press, New York, 1980) p. 529.
- [57] M. Rødbro, R. Bruch and P. Bisgaard, J. Phys. B 10 (1977) L275.
- [58] D. Schneider, W. Hodge, B.M. Johnson, L.E. Smith and C.F. Moore, Phys. Lett. A 54 (1975) 174.
- [59] J. Newcomb, T.R. Dillingham, J. Hall, S.L. Varghese, P.L. Pepmiller and P. Richard, Phys. Rev. A 29 (1984) 82.
- [60] M.W. Lucas and K.G. Harrison, J. Phys. B 5 (1972) L20.
- [61] A. Itoh, T. Schneider, G. Schiwietz, Z. Roller, H. Platten, G. Nolte, D. Schneider and N. Stolterfoht, J. Phys. B 16 (1983) 3965.
- [62] H.A. Bethe and R. Jackiw, Intermediate Quantum Mechanics (W.A. Benjamin Inc., New York, 1968) p. 135.
- [63] N. Stolterfoht, H. Gabler and U. Leithäuser, Phys. Lett. A 45 (1973) 351.
- [64] D. Coster and R.L. Kronig, Physica 2 (1935) 13.
- [65] T.A. Carlson and M.O. Krause, Phys. Rev. Lett. 17 (1965) 1079.
- [66] M.O. Krause, T.A. Carlson and W.E. Moddeman, J. Phys. (Paris) 32 (1971) C4-139.
- [67] V.V. Afrosimov, Yu.S. Gordeev, A.N. Zinoviev, D.H. Rasulov and A.P. Shergin, IX Intern. Confer. on the Physics of Electronic and Atomic Collisions, Abstracts, eds. J.S. Risley and R. Geballe (University Press, Seattle, 1975) p. 1068.
- [68] M.O. Krause, J. Phys. Chem. Ref. Data 8 (1979) 307.
- [69] E.U. Condon and G.H. Shortley, The Theory of Atomic Spectra (University Press, Cambridge, 1964).
- [70] T.C. Slater, Quantum Theory of Atomic Structure, Vol. I and Vol. II (McGraw Hill, New York, 1960).
- [71] D.R. Hartree, The Calculations of Atomic Structures (John Wiley & Sons Inc., New York, 1957).
- [72] I.P. Grant, Adv. Phys. 19 (1970) 747.
- [73] D.R. Hartree, Proc. Cambridge Phil. Soc. 24 (1927) 89.
- [74] V. Fock, Z. Physik 61 (1930) 126; 62 (1930) 795.
- [75] A. Messiah, Quantum Mechanics, Vol. I and Vol. II (North-Holland, Amsterdam, 1962);
G. Racah, Phys. Rev. 63 (1943) 367.
- [76] P.O. Löwdin, Rev. Mod. Phys. 34 (1962) 520.
- [77] O.K. Rice, J. Chem. Phys. 1 (1933) 375.
- [78] T. Åberg, Physica Scripta 21 (1980) 495.
- [79] S. Bashkin and J.O. Stoner Jr., Atomic Energy Levels and Grotrian Tables (North-Holland, Amsterdam, 1975);
C.E. Moore, Atomic Energy Levels, NBS Circular 467 (U.S. GPO, Washington D.C., 1949).
- [80] M.E. Rudd, Proc. Second Conf. on the Use of Small Accelerators for Teaching and Research, ed. J.L. Duggan (Oak Ridge, 1970) p. 305.
- [81] J.A. Bearden and A.F. Burr, Rev. Mod. Phys. 31 (1967) 49.
- [82] D.A. Shirley, R.L. Martin, S.P. Kowalczyk, F.R. McFeely and L. Ley, Phys. Rev. B 15 (1977) 544.
- [83] T.A. Koopmans, Physica 1 (1933) 104.
- [84] C. Froese-Fischer, Atomic Data 4 (1972) 301.
- [85] I. Bergström and R.D. Hill, Ark. Phys. 8 (1954) 27.
- [86] W.A. Coghlan and R.E. Clausing, Atomic Data 5 (1973) 317.
- [87] E.J. McGuire, Phys. Rev. A9 (1974) 1840.
- [88] W.N. Asaad and E.H.S. Burhop, Proc. Phys. Soc. Lond. 71 (1958) 369.
- [89] W.N. Asaad, Nucl. Phys. 44 (1963) 415.
- [90] W.N. Asaad, Nucl. Phys. 66 (1965) 494.
- [91] W. Mehlhorn and W.N. Asaad, Z. Phys. 191 (1966) 231.
- [92] K. Siegbahn et al., ESCA-Atomic, Molecular, and Solid-State Structure by Means of Electron Spectroscopy, Nova Acta Reg. Soc. Sci. Uppsallienis, Ser. IV (1967) p. 20.
- [93] D.A. Shirley, Phys. Rev. A 7 (1973) 1520.
- [94] L. Hedin and A. Johansson, J. Phys. B 2 (1969) 1336.
- [95] F.P. Larkins, J. Phys. B 9 (1976) 47.
- [96] F.P. Larkins, At. Data Nucl. Data Tables 20 (1977) 311.
- [97] Ch. Froese-Fischer, Comp. Phys. Comm. 1 (1969) 151; 4 (1972) 107; 14 (1978) 145.
- [98] J.P. Desclaux, Adv. Phys. 27 (1970) 351; Comp. Phys. Comm. 9 (1975) 31.
- [99] I.P. Grant, B.J. McKenzie, P.H. Norrington, D.F. Mayers and N.C. Pyper, Comp. Phys. Comm. 21 (1980) 207.
- [100] R.D. Cowan, The Theory of Atomic Structure and Spectra (University of California Press, Berkeley, 1981).
- [101] The computer programs [97-99] can be obtained from the CPC Library in Belfast.
- [102] H.P. Kelly, Phys. Rev. A 11 (1975) 556.
- [103] C. Briançon and J.P. Desclaux, Phys. Rev. A 13 (1976) 2157.
- [104] W. Mehlhorn, D. Stahlherm and H. Verbeck, Z. Naturforsch. A 23 (1968) 287.
- [105] P.J. Mohr, Phys. Rev. Lett. 34 (1975) 1050.
- [106] E.H.W. Wichmann and N.M. Kroll, Phys. Rev. 101 (1956) 843.
- [107] M.H. Chen, B. Crasemann and H. Mark, Phys. Rev. 24 (1981) 1158.
- [108] P. Feldman and R. Novick, Phys. Rev. 160 (1967) 143.
- [109] E.J. McGuire, Phys. Rev. A 10 (1974) 13 and 32.

- [110] D.L. Walters and C.P. Bhalla, *Phys. Rev. A* 3 (1971) 1919.
- [111] B.W. Shore and D.H. Menzel, *Principles of Atomic Spectra* (John Wiley, New York, 1968) p. 352.
- [112] E.J. Callan, *Rev. Mod. Phys.* 35 (1963) 524.
- [113] B. Crasemann, M.H. Chen and V.O. Kostroun, *Phys. Rev. A* 4 (1971) 2161.
- [114] V.O. Kostroun, M.H. Chen and B. Crasemann, *Phys. Rev. A* 3 (1971) 533.
- [115] P.V. Rao, M.H. Chen and B. Crasemann, *Phys. Rev. A* 5 (1972) 997.
- [116] R.A. Rubenstein and J.A. Snyder, *Phys. Rev.* 97 (1955) 1653;
R.A. Rubenstein, Ph.D. Thesis (University of Illinois, 1955) unpublished.
- [117] D.L. Walters and C.P. Bhalla, *Phys. Rev. A* 4 (1971) 2164.
- [118] D.L. Walters and C.P. Bhalla, *Atomic Data* 3 (1971) 301.
- [119] E.J. McGuire, *Phys. Rev.* 185 (1969) 1.
- [120] E.J. McGuire, *Phys. Rev. A* 2 (1970) 273.
- [121] E.J. McGuire, *Phys. Rev. A* 3 (1971) 587, 1801.
- [122] E.J. McGuire, *Phys. Rev. A* 5 (1972) 1043 and 1052.
- [123] M.H. Chen and B. Crasemann, *Phys. Rev. A* 8 (1973) 7.
- [124] C.P. Bhalla and D.R. Ramsdale, *Z. Phys.* 239 (1970) 95.
- [125] U. Gelius, *J. Electr. Spectrosc.* 5 (1974) 1985.
- [126] W.N. Asaad and W. Mehlhorn, *Z. Phys.* 217 (1968) 304.
- [127] S.N. El Ibari, W.N. Asaad and E.J. McGuire, *Phys. Rev. A* 5 (1972) 1048.
- [128] D. Ridder, J. Dieringer and N. Stolterfoht, *J. Phys. B* 9 (1976) L307.
- [129] O. Keski-Rahkonen and M.O. Krause, *At. Data Nucl. Data Tables* 14 (1974) 139.
- [130] W.N. Asaad and D. Petrini, *Proc. Roy. Soc. Lond. A* 350 (1976) 381.
- [131] M.H. Chen, E. Laimann and B. Crasemann, *Phys. Rev. A* 19 (1979) 2253.
- [132] M.H. Chen, B. Crasemann and H. Mark, *Phys. Rev. A* 21 (1980) 436, 442 and 449.
- [133] M.H. Chen, B. Crasemann and H. Mark, *Phys. Rev. A* 24 (1981) 177.
- [134] M.H. Chen and B. Crasemann, *Phys. Rev. A* 28 (1983) 2829.
- [135] G. Howat, T. Åberg, O. Goscinski, S.C. Soong, C.P. Bhalla and M. Ahmed, *Phys. Lett. A* 60 (1977) 404.
- [136] G. Howat, T. Åberg and O. Goscinski, *J. Phys. B* 11 (1978) 1575.
- [137] G. Howat, *J. Phys. B* 11 (1978) 1589.
- [138] Kh.R. Karim and B. Crasemann, *Phys. Rev.* 31 (1985) 709.
- [139] C.A. Nicolaidis and T. Mercouris, *Phys. Rev. A* 32 (1985) 3247.
- [140] E.J. McGuire, *Phys. Rev. A* 11 (1975) 10, 17, 1880 and 1889.
- [141] E.J. McGuire, *Phys. Rev. A* 12 (1975) 330.
- [142] E.J. McGuire, *Phys. Rev. A* 17 (1978) 182.
- [143] M.H. Chen and B. Crasemann, *Phys. Rev. A* 10 (1974) 2232.
- [144] M.H. Chen and B. Crasemann, *Phys. Rev. A* 12 (1975) 959.
- [145] M.H. Chen and B. Crasemann, *Phys. Rev. A* 16 (1977) 1495.
- [146] M.H. Chen, *Phys. Rev. A* 15 (1977) 2318.
- [147] M.H. Chen, B. Crasemann and H. Mark, *Phys. Rev. A* 24 (1981) 1852.
- [148] M.H. Chen, B. Crasemann and H. Mark, *Phys. Rev. A* 26 (1982) 1441.
- [149] M.H. Chen, B. Crasemann and H. Mark, *Phys. Rev. A* 27 (1983) 544.
- [150] Kh.R. Karim, M.H. Chen and B. Crasemann, *Phys. Rev. A* 28 (1983) 3355.
- [151] C.P. Bhalla, *Phys. Rev. A* 8 (1973) 2877.
- [152] C.P. Bhalla, *J. Phys. B* 8 (1975) 2787 and 2792.
- [153] C.P. Bhalla, *Phys. Rev. A* 12 (1975) 122.
- [154] P. Marmier and E. Sheldon, *Physics of Nuclei and Particles* (Academic Press, New York, 1969).
- [155] J.R. Risley, A.K. Edwards and R. Geballe, *Phys. Rev. A* 9 (1974) 1115.
- [156] N. Stolterfoht, D. Schneider, D. Burch, B. Aagaard, E. Bøving and B. Fastrup, *Phys. Rev. A* 12 (1975) 1313.
- [157] A. Gleizes, P. Benoit-Cattin, A. Bordenave-Montesquieu and H. Merchez, *J. Phys. B* 9 (1976) 473.
- [158] P. Dahl, M. Rødbro, B. Fastrup and M.E. Rudd, *J. Phys. B* 9 (1976) 1567.
- [159] N. Stolterfoht, D. Schneider, D. Burch, H. Wiemann and J.S. Risley, *Phys. Rev. Lett.* 33 (1974) 59.
- [160] F. Drepper and J.S. Briggs, *J. Phys. B* 9 (1976) 2063.
- [161] R. Morgenstern, A. Niehaus and G. Zimmermann, *J. Phys. B* 13 (1980) 4811.
- [162] D.J. Volz and M.E. Rudd, *Phys. Rev. A* 2 (1970) 1395.
- [163] D.L. Matthews, B.M. Johnson, J.J. Mackey, L.E. Smith, W. Hodge and G.F. Moore, *Phys. Rev. A* 10 (1974) 1177.
- [164] D. Burch, N. Stolterfoht, D. Schneider, H. Wiemann and J.S. Risley, *Nuclear Physics Annual Report 1974* (University of Washington, Seattle, 1975) unpublished.
- [165] T.A. Carlson, C.W. Nestor Jr. and T.C. Tucker, *Phys. Rev.* 169 (1968) 27.
- [166] M.O. Krause, F.A. Stevie, L.J. Lewis, T.A. Carlson and W.E. Moddeman, *Phys. Lett. A* 31 (1970) 81.

- [167] D. Schneider, K. Roberts, W. Hodge and C.F. Moore, *Phys. Rev. Lett.* 36 (1976) 1065.
- [168] A.K. Edwards and M.E. Rudd, *Phys. Rev.* 170 (1968) 140.
- [169] D. Schneider, D.F. Burch and N. Stolterfoht, *Proc. VIIIth Intern. on the Physics of Electronic and Atomic Collisions, Abstracts of Papers*, eds. R.C. Cobic and M.K. Kurepa (Institute of Physics, Beograd, 1973) p. 729.
- [170] N. Stolterfoht, *Phys. Lett. A* 41 (1972) 400.
- [171] D.L. Matthews, B.J. Johnson and C.F. Moore, *At. Data Nucl. Data Tables* 15 (1975) 40.
- [172] C.P. Bhalla, N.O. Folland and M.A. Hein, *Phys. Rev. A* 8 (1973) 649.
- [173] R.L. Kauffman, C.W. Woods, K.A. Jamison and P. Richard, *Phys. Rev. A* 11 (1975) 873.
- [174] D. Schneider, C.F. Moore and B.M. Johnson, *J. Phys. B* 9 (1976) L153.
- [175] D.F. Burch, L. Willets and W.E. Meyerhof, *Phys. Rev. A* 9 (1974) 1007.
- [176] P. Ziem, R. Bruch and N. Stolterfoht, *J. Phys. B* 8 (1976) L480.
- [177] D.L. Ederer, T. Lucatoro and R.P. Madden, *Phys. Rev. Lett.* 25 (1970) 1537.
- [178] H.G. Berry, J. Desesquelles and M. Dufay, *Nucl. Instrum. Meth.* 110 (1973) 42.
- [179] C.F. Moore, J.J. Mackey, L.E. Smith, J. Bolger, B.M. Johnson and D.L. Matthews, *J. Phys. B* 7 (1974) L302.
- [180] L. Toburen, N. Stolterfoht, P. Ziem and D. Schneider, *Phys. Rev. A* 24 (1981) 1741.
- [181] N. Stolterfoht, D. Schneider and P. Ziem, *Phys. Rev. A* 10 (1974) 81.
- [182] D. Ridder, J. Dieringer and N. Stolterfoht, *IXth Intern. Conf. on the Physics of Electronic and Atomic Collisions, Abstracts of Papers*, eds. J.S. Risley and R. Geballe (University of Washington, Seattle, 1975) p. 419.
- [183] W. Mehlhorn and D. Stahlherm, *Z. Phys.* 217 (1968) 294.
- [184] L.O. Werme, T. Bergmark and K. Siegbahn, *Phys. Scr.* 6 (1972) 141.
- [185] L.O. Werme, T. Bergmark and K. Siegbahn, *Phys. Scr.* 8 (1973) 149.
- [186] W. Mehlhorn, *Z. Phys.* 208 (1968) 1.
- [187] J. Nordgren, H. Ågren, C. Nordling and K. Siegbahn, *Phys. Scr.* 19 (1979) 5.
- [188] N. Stolterfoht, F.J. de Heer and J. van Eck, *Phys. Rev. Lett.* 30 (1973) 1159.
- [189] R.L. Watson and L.H. Toburen, *Phys. Rev. A* 7 (1973) 1853.
- [190] H. Christofzig, thesis (Münster) 1970, unpublished, see also in ref. [188].
- [191] N. Stolterfoht, D. Schneider and H. Gabler, *Phys. Lett. A* 47 (1974) 271.
- [192] B.M. Johnson, D.L. Matthews, L.E. Smith and C.F. Moore, *J. Phys. B* 6 (1973) L444.
- [193] D. Schneider, B.M. Johnson, B. Hodge and C.F. Moore, *Phys. Lett. A* 59 (1976) 25.
- [194] F. Folkmann, K.M. Cramon, R. Mann and H.F. Beyer, *Phys. Scr. T* 3 (1983) 166.
- [195] T. Matsuo, H. Shibita, J. Urakawa, A. Yagishita, Y. Awaya, T. Kambara, M. Kase, H. Kumagai and J. Tawahashi, *RIKEN Accel. Rep.* 17 (1983) 65.
- [196] P. Ziem, G. Wüstefeld and N. Stolterfoht, *Proc. 2nd Intern. Conf. on Inner-Shell Ionization Phenomena, Abstracts of Papers*, eds. W. Mehlhorn and R. Brenn (Freiburg, 1976) p. 38.
- [197] C.E. Theodosiou, E. Breukmann, B. Breukmann and W. Mehlhorn, *J. Phys. B* 12 (1979) L689.
- [198] D.F. Burch, *Proc. Intern. Conf. on Inner-Shell Ionization Phenomena*, eds. R.W. Fink et al., Conf.-720 404 (USAEC, Oak Ridge, 1973).
- [199] J.M. Hansteen and O.P. Mosebeck, *Phys. Rev. Lett.* 29 (1972) 1361.
- [200] T. Åberg and O. Goscinski, *X-Ray and Atomic Inner-Shell Phenomena*, ed. B. Crasemann, AIPCP No. 94 (American Institute of Physics, New York, 1982) p. 121.
- [201] T. Åberg, A. Blomberg, J. Tulkki and O. Goscinski, *Phys. Rev. Lett.* 52 (1984) 1207.
- [202] P. Richard, *Atomic Inner-Shell Processes*, Vol. 1, ed. B. Crasemann (Academic Press, New York, 1975) p. 74.
- [203] N. Stolterfoht, D. Schneider, P. Richard and R.L. Kauffman, *Phys. Rev. Lett.* 33 (1974) 1418.
- [204] D.L. Matthews, B.M. Johnson, L.E. Smith, J.J. Mackey and C.F. Moore, *Phys. Lett. A* 48 (1974) 93.
- [205] F. Folkmann, R. Mann and H.F. Beyer, *Phys. Scr. T* 3 (1983) 88.
- [206] C. Schmiedekamp, B.L. Doyle, T.J. Gray, R.K. Gardner, K.A. Jamison and P. Richard, *Phys. Rev. A* 18 (1978) 1892.
- [207] B. Sulik, G. Hock and D. Berényi, *J. Phys. B* 17 (1984) 3239.
- [208] D.H. Madison and E. Merzbacher, *Atomic Inner-Shell Processes*, Vol. I, ed. B. Crasemann (Academic Press, New York, 1975) p. 1.
- [209] J.H. McGuire, N. Stolterfoht and P.R. Simony, *Phys. Rev. A* 24 (1981) 97.
- [210] D.L. Matthews, R.J. Fortner, D. Schneider and C.F. Moore, *Phys. Rev. A* 14 (1976) 1561.
- [211] S. Schumann, K.O. Groeneveld, G. Nolte and B. Fricke, *Z. Phys. A* 289 (1979) 245.
- [212] R. Mann, F. Folkmann and H.F. Beyer, *J. Phys. B* 14 (1981) 1161.
- [213] V. Schmidt, *Proc. Intern. Conf. on Inner-Shell Ionization Phenomena*, eds. R.W. Fink et al., Conf. No. 720404 (USAEC, Washington D.C., 1973) p. 548.
- [214] C.P. Bhalla, D.L. Matthews and C.F. Moore, *Phys. Lett. A* 46 (1974) 336.
- [215] N. Stolterfoht, *Proc. 2nd Intern. Conf. on Inner-Shell Ionization Phenomena, Invited Papers*, eds. W. Mehlhorn and R. Brenn (Freiburg, 1976) p. 42.
- [216] N. Stolterfoht, D. Schneider, R. Mann, F. Folkmann and K.O. Groeneveld, *Hahn-Meitner-Institut Annual Report 1978*, HMI-294, ISSN 0440-0836 (Berlin, 1979) unpublished.
- [217] R. Mann, H.F. Beyer and F. Folkmann, *Phys. Rev. Lett.* 46 (1981) 646.

- [218] R. Mann, private communication (1985).
- [219] H. Ryufuku, K. Sasaki and T. Watanabe, Phys. Rev. A 21 (1980) 745.
- [220] H.F. Beyer, F. Folkmann and K.H. Schartner, J. Phys. (Paris) 40 (1979) C1-17.
- [221] R.K. Janev and L.P. Presnyakov, Phys. Reports 70 (1981) 1.
- [222] K.M. Cramon and F. Folkmann, The Physics of Electron Ejection in Ion-Atom and Ion-Solid Interaction, Lecture Notes in Physics 213, eds. K.O. Groeneveld, W. Meckbach and I.A. Sellin (Springer Verlag Heidelberg, 1984) p. 94.
- [223] T.A. Carlson and K.M. White, J. Chem. Phys. 44 (1966) 4510.
- [224] R. Mann, F. Folkmann and K.O. Groeneveld, Phys. Rev. Lett. 37 (1976) 1674.
- [225] R. Mann, F. Folkmann, R.S. Peterson, Gy. Szabo and K.O. Groeneveld, J. Phys. B 11 (1978) 3045.
- [226] N. Stolterfoht, Proc. Intern. on Inner-Shell Ionization Phenomena and Future Applications, eds. R.W. Fink et al., Conf-720 404 (USAEC, Oak Ridge, TN 1973) p. 1043.
- [227] H.G. Berry, Rep. Prog. Phys. 40 (1977) 155.
- [228] G.M. Thomson, W.W. Smith and A. Russek, Phys. Rev. A 7 (1973) 168.
- [229] S. Hagmann, C.L. Cocke, P. Richard, A. Skutlartz, S. Kelbch, H. Schmidt-Böckling and R. Schuch, Electronic and Atomic Collisions, eds. J. Eichler, I.V. Hertel and N. Stolterfoht (North-Holland, Amsterdam, 1984) p. 385.
- [230] M. Suter, C.R. Vane, S.B. Elston, I.A. Sellin, R.S. Thoe and G.D. Alton, XIth Intern. Conf. on the Physics of Electronic and Atomic Collisions, Abstracts of Papers, eds. K. Takayanagi and N. Oda (Kyoto, 1979) p. 762.
- [231] N. Stolterfoht, A. Itoh, D. Schneider, Th. Schneider, G. Schiwietz, H. Platten, G. Nolte, R. Glodde, U. Stettner, W. Zeitz and T.J. Zouros, Intern. Conf. on X-Ray and Inner-Shell Processes in Atoms Molecules and Solids, Invited Lectures, ed. A. Meisel (Leipzig, 1984) p. 193.
- [232] P. Bisgaard, P. Dahl, B. Fastrup and W. Mehlhorn, J. Phys. B 14 (1981) 2023.
- [233] S.B. Elston, Inner-Shell and X-Ray Physics of Atoms and Solids, eds. D.J. Fabian, H. Kleinpoppen and L.M. Watson (Plenum Press, New York, 1981) p. 132.
- [234] M. Suter, C.R. Vane, S.B. Elston, G.D. Alton, P.M. Griffin, R.S. Thoe, L. Williams and I.A. Sellin, Z. Phys. 289 (1979) 433.
- [235] L.H. Anderson, M. Frost, P. Hvelplund, H. Knudsen and S. Datz, Phys. Rev. Lett. 52 (1984) 518.
- [236] T.J. Kvale, G.D. Alton, R.N. Compton, D.J. Pegg and J.S. Thomson, Phys. Rev. Lett. 55 (1985) 484.
- [237] Th. Schneider, D. Schneider, G. Schiwietz, H. Platten, W. Zeitz, T.J. Zouros and N. Stolterfoht, to be published.
- [238] B.M. Johnson, D. Schneider, K.S. Roberts, J.E. Bolger and C.F. Moore, Phys. Lett. A 53 (1975) 245.
- [239] K.O. Groeneveld, R. Mann, G. Nolte, S. Schumann, R. Spohr and B. Fricke, Z. Phys. A 274 (1975) 191.
- [240] R. Bruch, G. Paul, J. Andrä and L. Lipsky, Phys. Rev. A 12 (1975) 1808.
- [241] R. Bruch, D. Schneider, W.H.E. Schwarz, M. Meinhart, B.M. Johnson and K. Taulbjerg, Phys. Rev. A 19 (1979) 587.
- [242] B. Rossner and W. Brandt, Phys. Lett. A61 (1977) 97.
- [243] D. Schneider, R. Bruch, W.H.E. Schwarz, T.C. Chang and C.F. Moore, Phys. Rev. A 15 (1977) 926.
- [244] D. Schneider, D. Ridder, R. Bruch, W.H.E. Schwarz and B.M. Johnson, Jpn. J. Appl. Phys. 17-2 (1978) 395.
- [245] D. Schneider, R. Bruch, W. Butcher and W.H.E. Schwarz, Phys. Rev. A 24 (1981) 1223.
- [246] W.H.E. Schwarz and T.C. Chang, Int. J. Quantum Chem. S 10 (1976) 91.
- [247] U.I. Safronova and V.N. Kharitonova, Opt. Spectrosc. 27 (1969) 300.
- [248] U. Feldman and L. Cohen, Astrophys. J. 158 (1969) L169.
- [249] E. Høloien and S. Geltman, Phys. Rev. 153 (1967) 81.
- [250] S. Goldsmith, J. Phys. B 7 (1974) 2315.
- [251] L. Lipski, R. Anania and M.J. Conneely, At. Data Nucl. Data Tables 20 (1977) 127.
- [252] M. Rødbro, R. Bruch, P. Bisgaard, P. Dahl and B. Fastrup, J. Phys. B 10 (1977) L483.
- [253] M. Rødbro, R. Bruch and P. Bisgaard, J. Phys. B 12 (1979) 2413.
- [254] E.T. Kennedy and P.K. Carroll, Phys. Lett. A 64 (1977) 37.
- [255] K.T. Chung and R. Bruch, Phys. Rev. 28 (1983) 1418.
- [256] R. Bruch, K.T. Chung, W.L. Luken and J.C. Culberson, Phys. Rev. 31 (1985) 310.
- [257] K.T. Chung, Phys. Rev. A 20 (1979) 1743.
- [258] W.L. Luken and J.M. Leonhard, Phys. Rev. A 28 (1983) 532.
- [259] A. Pople and R.K. Nesbet, J. Chem. Phys. 22 (1954) 571.
- [260] Y.M.C. Chan and A.L. Stuart, Proc. Phys. Soc. 90 (1967) 619.
- [261] W.L. Wiese and A.W. Weiss, Phys. Rev. 175 (1968) 50.
- [262] G.W.F. Drake and A. Dalgarno, Phys. Rev. A 1 (1970) 1325.
- [263] H. Doyle, M. Oppenheimer and G.W.F. Drake, Phys. Rev. A 5 (1972) 26.
- [264] T.R. Dillingham, J. Newcomb, J. Hall, P.L. Pepmiller and P. Richard, Phys. Rev. A 29 (1984) 3029.
- [265] J.A. Tanis, E.M. Bernstein, W.G. Graham, M.P. Stöckli, M. Clark, R.H. McFarland, T.J. Morgan, K.H. Berkner, A.S. Schlachter and J.W. Stearns, Phys. Rev. Lett. 53 (1984) 2551.
- [266] A. Itoh, T.J.M. Zouros, D. Schneider, U. Stettner, W. Zeitz and N. Stolterfoht, J. Phys. B 18 (1986) 4581.
- [267] M. Terasawa, T.J. Gray, S. Hagmann, J. Hall, J. Newcomb, P. Pepmiller and P. Richard, Phys. Rev. A 27 (1983) 2868.
- [268] A. Itoh, D. Schneider, T. Schneider, T.J.M. Zouros, G. Nolte, G. Schiwietz, W. Zeitz and N. Stolterfoht, Phys. Rev. 31 (1985) 684.
- [269] N. Stolterfoht using the computer code by Grant [99].

- [270] B. Donnally, W.W. Smith, D.J. Pegg, M. Brown and I.A. Sellin, Phys. Rev. A 4 (1971) 122.
- [271] I.A. Sellin, D.J. Pegg, M. Brown, W.W. Smith and B. Donnally, Phys. Rev. Lett. 27 (1971) 1108.
- [272] D.J. Pegg, I.A. Sellin, R. Peterson, J.R. Mowat, W.W. Smith, M.D. Brown and J.R. MacDonald, Phys. Rev. A 8 (1973) 1350.
- [273] I.A. Sellin, D.J. Pegg, P.M. Griffin and W.W. Smith, Phys. Rev. Lett. 28 (1972) 1229.
- [274] D.J. Pegg, I.A. Sellin, P.M. Griffin and W.W. Smith, Phys. Rev. Lett. 28 (1972) 1615.
- [275] D.J. Pegg, P.M. Griffin, I.A. Sellin and W.W. Smith, Nucl. Instr. Meth. 110 (1973) 489.
- [276] D.J. Pegg, H.H. Haselton, P.M. Griffin, R. Laubert, J. R. Mowat, R. Peterson and I.A. Sellin, Phys. Rev. A 9 (1974) 1112.
- [277] H.H. Haselton, R.S. Thoe, J.R. Mowat, P.M. Griffin, D.J. Pegg and I.A. Sellin, Phys. Rev. A 11 (1975) 468.
- [278] I.S. Dmitriev, Ya.A. Teplova and V.S. Nikolaev, Zh. Eksperim. Teor. Fiz. 61 (1971) 1359 [Sov. Phys.-JETP 34 (1972) 723].
- [279] P. Feldman and R. Novick, Phys. Rev. Lett. 11 (1963) 278.
- [280] P. Richard, R.L. Kauffman, F.F. Hopkins, C.W. Woods and K.A. Jamison, Phys. Rev. Lett. 30 (1973) 888.
- [281] P. Richard, R.L. Kauffman, F.F. Hopkins, C.W. Wood and K.A. Jamison, Phys. Rev. A 8 (1973) 2187.
- [282] C.L. Cocke, B. Carnutte and R. Randall, Phys. Rev. A 9 (1974) 1823.
- [283] H.D. Dohmann and R. Mann, Z. Phys. A 291 (1979) 15.
- [284] R. Bruch, G. Paul and J. Andrä, J. Phys. B 8 (1975) L253.
- [285] R. Bruch, M. Rødbro, P. Bisgaard and P. Dahl, Phys. Rev. Lett. 39 (1977) 801.
- [286] S.T. Manson, Phys. Lett. 23 (1966) 315; Phys. Rev. A 3 (1971) 147.
- [287] V.V. Balashov, V.S. Senashenko and B. Tekou, Phys. Lett. A 25 (1967) 487.
- [288] K.T. Cheng, C.P. Lin and W.R. Johnson, Phys. Lett. A 48 (1974) 437.
- [289] C.P. Bhalla and A.H. Gabriel, Beam Foil Spectroscopy, Vol. 1, eds. I.A. Sellin and D.J. Pegg (Plenum, New York, 1976) p. 121.
- [290] J.R. McDonald, L. Winters, M.D. Brown, T. Chiao and L.D. Ellsworth, Phys. Rev. Lett. 29 (1972) 1291.
- [291] N. Stolterfoht, D. Schneider, D. Burch, H. Wieman and J.S. Risley, Phys. Rev. Lett. 33 (1974) 59.
- [292] W.W. Smith, B. Donnally, D.J. Pegg, M. Brown and I.A. Sellin, Phys. Rev. A 7 (1973) 487.
- [293] The metastable beam fraction of less than 10% given by Itoh et al. [268] is incorrect. The authors erroneously divided the observed fraction of 51% by the ratio of statistical weights for the ^4P and ^2S states.
- [294] I.L. Beigmann and L.A. Bureyeva, Ninth Intern. Conf. on Atomic Physics, Abstracts, eds. R.S. van Dyk and E.N. Fortson (Washington University Press, Seattle, 1984) p. A18.
- [295] D.J. Pegg, H.H. Haselton, R.S. Thoe, P.M. Griffin, M.D. Brown and I.A. Sellin, Phys. Rev. A 12 (1975) 1330.
- [296] P. Bisgaard, J.O. Olson and N. Anderson, J. Phys. B 13 (1980) 1403.
- [297] P. Dahl, M. Rødbro, G. Hermann, B. Fastrup and M.E. Rudd, J. Phys. B 9 (1976) 1581.
- [298] B. Fastrup, G. Hermann and K.J. Smith, Phys. Rev. A 3 (1971) 1591.
- [299] D. Ridder and D. Schneider, Phys. Rev. A 25 (1982) 921.
- [300] N. Stolterfoht, Th. Schneider, D. Schneider and A. Itoh, XIVth Intern. Conf. on the Physics of Electronic and Atomic Collisions, Abstracts, eds. M.J. Coggiola, D.L. Huestis and R.P. Saxon (University Press, Stanford, 1985) p. 467.
- [301] W. Menzel and W. Mehlhorn, private communication. The calculations were performed using the DF code by Grant [99].
- [302] E.J. Hanson, private communication. The calculations were performed using the computer code by Cowan [100].
- [303] M. Sekiya, T. Noro, I. Sasaki, T. Watanabe and K. Ohno, RIKEN Accel. Progr. Rep. 18 (1984) 67.
- [304] M. Breinig, S.B. Elston, S. Hult, L. Liljeby, C.R. Vane, S.D. Berry, G.A. Glass, M.M. Schauer, I.A. Sellin, G.D. Alton, S. Datz, S. Overbring, R. Laubert and J.M. Suter, Phys. Rev. A 25 (1982) 3015.
- [305] L.H. Anderson, M. Frost, P. Hvelplund and H. Knudsen, J. Phys. B 17 (1984) 4701.
- [306] A. Itoh and N. Stolterfoht, Nucl. Instr. Meth. B10/11 (1985) 97.
- [307] Th. Schneider, D. Schneider, W. Zeitz, G. Schiwietz, H. Platten, U. Stettner and N. Stolterfoht, 6. Arbeitstagung für energiereiche atomare Stöße (Obersdorf, 1985) unpublished.
- [308] N. Stolterfoht, P.D. Miller, H.F. Krause, Y. Yamazaki, P.F. Dittner, P.L. Pepmiller, I.A. Sellin and S. Datz, Second U.S.-Mexico Symp. on Atomic and Molecular Physics: Two Electron Phenomena (Cocoyoc, Mexico, 1986).
- [309] D.C. Griffin, M.S. Pindzola and C. Bottcher, Phys. Rev. A 31 (1985) 568;
D.C. Griffin, private communication.
- [310] N. Stolterfoht, D. Brandt and M. Prost, Phys. Rev. Lett. 43 (1979) 1654.
- [311] Y. Yamazaki, P.D. Miller, H.F. Krause, P.L. Pepmiller, S. Datz, I.A. Sellin and N. Stolterfoht, Phys. Rev. Lett. 57 (1986) 992.